TÉCNICO LISBOA

Optical nanoantennas for photovoltaic applications

Francisco Bernardo Duarte

Thesis to obtain the Master of Science Degree in

Electrical and Computer Engineering

Supervisors:

Professor António Carlos De Campos Simões Baptista
Professor João Paulo Neto Torres

Examination Committee

Chairperson: Professor Francisco André Corrêa Alegria

Supervisor: António Carlos De Campos Simões Baptista

Members of the Committee: Professor Maria João Marques Martins

November 2019

Declaração

Declaro que o presente documento é um trabalho original da minha autoria e que cumpre todos os requisitos do Código de Conduta e Boas Práticas da Universidade de Lisboa.

I declare that this document is an original work of my own authorship and that it fulfils all the requirements of the Code of Conduct and Good Practices of the Universidade de Lisboa.

Agradecimentos

Nesta secção gostaria de agradecer a todos aqueles que ao longo do meu Mestrado em Engenharia Eletrotécnica e de Computadores me ajudaram, direta ou indiretamente, a cumprir os meus objetivos e a realizar mais uma etapa da minha formação académica.

Em primeiro lugar, gostaria de agradecer profundamente à minha Família, em especial aos meus Pais, por todo o apoio e carinho e pela educação e ensinamentos de vida que me proporcionaram. Sempre acreditaram em mim e estiveram ao meu lado, nos bons e nos maus momentos. Espero que esta fase da minha vida, que agora termino, possa de alguma forma retribuir e compensar todo o apoio que me oferecem e que espero continuar sempre a receber pela vida fora.

Em segundo, ao Instituto Superior Técnico, nomeadamente professores, funcionários, que contribuíram para o meu crescimento pessoal e profissional.

A todos os meus amigos e colegas de curso, que sempre me acompanharam ao longo deste percurso académico e que certamente me continuarão a acompanhar no futuro. Obrigado pela vossa amizade e por todos os momentos vividos ao longo destes anos.

Aos meus orientadores, Professor Doutor António Baptista e Professor Doutor João Paulo Neto Torres, docentes com um excelente currículo científico e académico, pelo apoio, disponibilidade para esclarecimento de dúvidas ou conselhos e por me terem dado todas as condições para que eu pudesse realizar esta dissertação. Certamente não esquecerei.

A todos deixo aqui o meu sincero agradecimento.

Resumo

A ideia de converter luz em energia elétrica com auxílio de antenas ópticas foi proposta há cerca de quatro décadas, mas ainda não foi alcançada com sucesso.

No entanto, na última década, o desenvolvimento e o progresso da nanotecnologia permitem uma melhor compreensão da interação da luz com a matéria em escala nanométrica. A sua capacidade única de criar novas estruturas em escala atómica já produziu novos materiais e dispositivos com grandes aplicações num grande número de áreas.

Nesse contexto, a nanotecnologia permite o desenvolvimento de modelos, como antenas ópticas nanométricas com dimensões menores que o comprimento de onda da radiação eletromagnética incidente. Estas antenas ópticas combinadas com painéis solares fotovoltaicos estão a emergir como uma solução de energia renovável com bastante potencial, tendo como principais vantagens: o aumento do rendimento das células solares e a redução dos seus custos de fabricação e produção de energia. A característica única do uso de antenas ópticas para a produção de energia elétrica são as suas fendas. A passagem da luz através de fendas muito menores que o comprimento de onda da luz provou ser um fenómeno surpreendentemente interessante.

O principal objetivo desta dissertação de mestrado é a análise de uma nanoantena com fendas, que deve ser integrada em cima de uma célula solar fotovoltaica. Para isso, é feita uma análise de desempenho, usando o software COMSOL Multiphysics®, com diferentes materiais e tipos de nanoantenas. Uma vez obtidos os resultados das simulações, é feita uma comparação dos resultados com modelos teóricos e a nanoantena mais adequada é escolhida para uso num painel solar fotovoltaico.

Palavras-chave: antena óptica; nanoantena; fendas; solar; energia; fotovoltaica.

Abstract

The idea of collecting solar electromagnetic radiation with optical antennas was proposed four decades ago but has not yet been achieved successfully.

However, in the last decade, the development and progress of nanotechnology allows a better understanding of light-matter interaction at a nanometric scale. Its unique capability to fabricate new structures at atomic scale has already produced novel materials and devices with great potential applications in a wide number of fields.

In this context, nanotechnology allows the development of models, such as nanometric optical antennas with dimensions smaller than the wavelength of the incident electromagnetic wave. These optical antennas combined with photovoltaic solar panels are now emerging as a potential renewable energy solution, by increasing the efficiency of solar cells, while reducing their manufacturing and electricity production costs. The unique feature of using these optical antennas for solar energy harvesting is their apertures. The passage of light through apertures much smaller than the wavelength of light has proved to be a surprisingly interesting phenomenon.

The main objective of this master thesis is to analyze an aperture array nanoantenna, which is intended to be integrated on top of a solar photovoltaic cell. For that, a performance analysis, using COMSOL Multiphysics® software, is made with different materials and designs of nanoantennas. Once the simulations results are obtained, a comparison of the results is made with theoretical models and the most suitable nanoantenna is then chosen for use on a solar photovoltaic panel.

Keywords: optical antenna; rectenna; nanoantenna; apertures; solar; energy; photovoltaic.

Index

List of figures

List of tables

Acronyms

AC	Alternating Current
CPV	Concentrator Photovoltaic
CIGS	Copper-Indium-Gallium selenide
DC	Direct Current
EM	Electromagnetic
EOT	Extraordinary Optical Transmission
FEM	Finite Element Method
IEA	International Energy Agency
IR	Infrared
LSP	Localized Surface Plasmon
MIM	Metal-Insulator-Metal
NREL	National Renewable Energy Laboratory
NSOM	Nearfield Scanning Optical Microscopy
RF	Radio-Frequency
SEM	Scanning Electron Microscope
STC	Standard Test Conditions
SPP	Surface Plasmon Polariton
SPR	Surface Plasmon Resonance
PV	Photovoltaic
TE	Transverse Electric
TM	Transverse Magnetic
UV	Ultraviolet

1. Introduction

Since the main topic of this dissertation is the application of nanoantennas for solar energy harvesting, it is fundamental to start with a brief overview of the different photovoltaic technologies. Before establishing the work's targets and original contributions, its scope and motivations are brought up. At the end of this chapter, the work's structure is provided.

1.1. General overview

Worldwide energy demands have increased significantly over the last 20 years. As of 2018, 64% of the world's power is still generated by combustion of fossil fuels [1]. Clean renewable alternative energy sources are required to meet the demands and by ensuring that climate targets are met.

Renewable energy sources give a strong contribution to power generation with a short impact on environmental pollution. The International Energy Agency (IEA) predict that renewables will have the fastest growth in the electricity sector in the next upcoming years, providing almost 30% of the world's power demand in 2023, up from 24% in 2018. During this period, renewables are forecast to meet more than 70% of global electricity generation growth, led by solar photovoltaic (PV) and followed by wind, hydropower, and bioenergy [2].

Solar PV energy can take advantage of the enormous potential of solar radiation. The sun represents the most abundant source of energy that is freely available. The direct conversion of solar energy into electricity on a large-scale has been made possible by the emergence of PV solar cells, which are relatively low cost [4].

The most common photovoltaic cells, consisting of PN junctions of mono-crystalline, polycrystalline or amorphous silicon, made a direct conversion of the power associated with solar radiation into DC electric power [4]. PV cells are robust structures that require very little maintenance and so they are an attractive technology that is rapidly expanding on the global energy market [4].

However, PV solar cells have quite a few limitations: only a small part of the incoming solar radiation can be converted to electricity by semiconductors, while the remaining radiation can be absorbed by the cell, but instead is converted into heat due to intrinsic material characteristics electrical properties [5].

The record lab cell efficiency for a silicon mono-crystalline cell is 26.7%, but traditional single-junction PV cells generally have an efficiency of 20%, in ideal conditions [6][15].

Furthermore, the performance of photovoltaic cells is largely dependent on weather factors: power generation from PV cells alters with changes in the amount of solar irradiation they receive during the day, their performance can be influenced by changes in temperature and also the accumulation of dust particles on its surface [6].

Currently, PV market is based on silicon solar cells that are thick cells of around 150–300 nm made of crystalline silicon. This technology, classified as the first-generation of photovoltaic cells, accounts for more than 86% of the global solar cell market. The crystalline silicon cells are divided into three main types: Monocrystalline, Polycrystalline and Ribbon puled silicon cells [4]. In 2017, the market share of crystalline technology is now about 62% of total production [7].

While silicon remains the material of choice for photovoltaics because of its abundance, non-toxicity, high and stable cell efficiencies, other elements have been used in the manufacture of single-junction PV cells that have a higher efficiency, like Gallium Arsenide (GaAs) or Indium Phosphide (InP) solar cells. Due to its high cost of fabrication, they have been mostly applied in solutions for satellites in space [4][8].

Figure 1.1 – Monocrystalline, Polycrystalline and Thin-Film solar cells [9]

The use of single-junction PV cells has not been further developed, given that on a multi-junction configuration of these materials it is possible to reach higher efficiency levels. The cell design includes multiple layers: two, three or even four junctions with different bandgaps. The highest solar cell conversion efficiencies are achieved with four-junction devices under concentrated sunlight illumination. They can reach efficiency values over 40% [10].

Multi-junction cells are emerging in concentrator photovoltaic (CPV) systems with a growing number of installations around the world in regions with a large amount of direct solar radiation[1]. CPV systems have the advantage of producing low-cost electricity in PV power plants. The solar radiation incident in Portugal, particularly in the south, has a significant direct component, which makes our country especially suitable for the installation of these converters [4].

[1] Direct solar radiation is used to describe solar radiation traveling ideally on a straight line from the sun down to the surface of the earth. Direct solar radiation varies with latitude, climate, season of the year and time of the day.

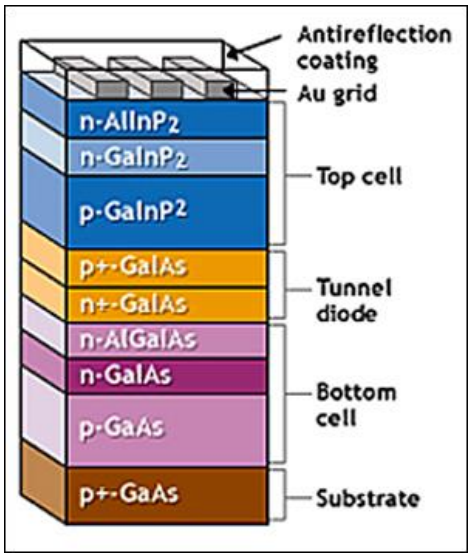

Figure 1.2 – Multi-junction solar cell [4]

The second generation of photovoltaic materials is based on the introduction of thin-film layers with high light absorption properties. Thin-film thickness varies from a few nanometers (nm) to tens of micrometers (µm), much thinner than the conventional first-generation crystalline silicon solar cell, that uses wafers of up to 200 µm thick. Thin-films are deposited on glass or plastic substrates with great flexibility that have experienced a strong growth in recent years due to their low fabrication cost. The National Renewable Energy Laboratory (NREL) classifies a number of thin-film as emerging PV technologies, mainly because most of them have not yet entered the market and are still in the research or development phase [10a].

The three-mainstream thin-film PV technologies currently in use today are: Cadmium Telluride (CdTe), Amorphous Silicon (a-Si) and Copper-Indium-Gallium selenide (CIGS) thin-films. CdTe solar cell efficiency has been rapidly increasing in recent years with an average production line module efficiency at around 15%. However, it has a major disadvantage due to the toxicity of its materials. Amorphous Silicon (a-Si) thin-films are made from a layer of silicon deposited as thin-film on a plastic backing. They are inexpensive to produce because the silicon atoms are disorganized and do not form perfect crystals. They have a low efficiency of up to 8%-11%. Whereas recently, CIGS technology is getting more popular than other thin-film technologies due to its higher efficiency, faster and cheaper manufacturing process [11].

It can be stated that thin-film cells are currently cheaper than crystalline silicon cells, but less efficient in energy conversion. Due to their characteristics, thin-film technology could emerge as a niche market holder, in building-integrated photovoltaics, where it can be used to replace conventional building materials in the roof, skylights or facades. Furthermore, the production process of thin-film solar panels consumes about 70% less energy than that of crystalline panels [4] [9].

Finally, a new concept of thin-films based in novel materials has appeared in the market. This class is known as the third generation of photovoltaics, which have the potential to overcome the current efficiency of the previous generations. This generation includes the Dye-sensitized nanocrystalline cells, perovskite cells or organic cells.

Dye-sensitized nanocrystalline cells are another alternative offered by nanotechnology to conventional silicon-based solar cells. O'Regan and Gratzel introduced in 1991 the first nanostructured solar cell, namely Gratzel cell, based on dye-sensitized titanium dioxide films [12]. Recently, this type of solar cells has been fabricated from nanoparticles of several semiconductors and different architectures such as nanotubes or photonic crystals, in order to increase their efficiency. The market of the Gratzel cells is still in research stage, where devices such as photoelectrochemical cells, polymer solar cells and nanocrystal solar cells are being tested [13].

Another concept of solar cells has been tested with perovskite materials. These materials are known for its superconductivity and magnetoresistance and are cheap to produce and simple to manufacture [14]. Solar cell efficiencies of devices using these materials have increased from 3.8% in 2009 to 23.3% in late 2018 in single-junction cells, making them the fastest-advancing solar technology to date [15]. It has a potential of achieving even higher efficiencies along together with very low production costs, which make them commercially attractive.

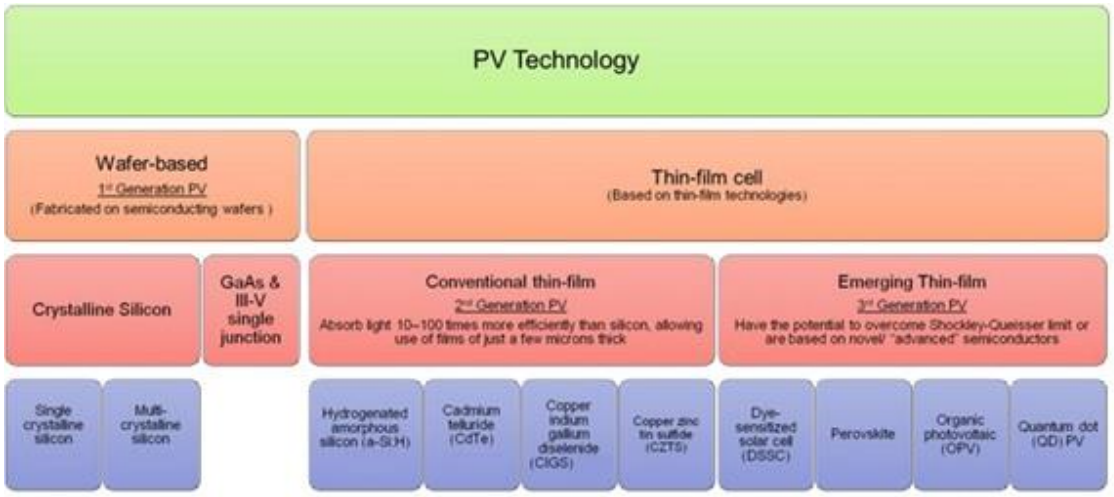

Figure 1.3 – Summary of the three photovoltaic generations
(adapted from: **[16]** R. Pernechelle, New Copper Redox Couples for Liquid Dye-Sensitized Solar Cells, KTH Royal Institute of Technology, 2017)

On the following page, there is an efficiency chart of compiled values by the *National* Renewable Energy Laboratory (NREL) of the highest confirmed conversion efficiencies for research cells, from 1976 to the present, for all three generations of photovoltaic technologies.

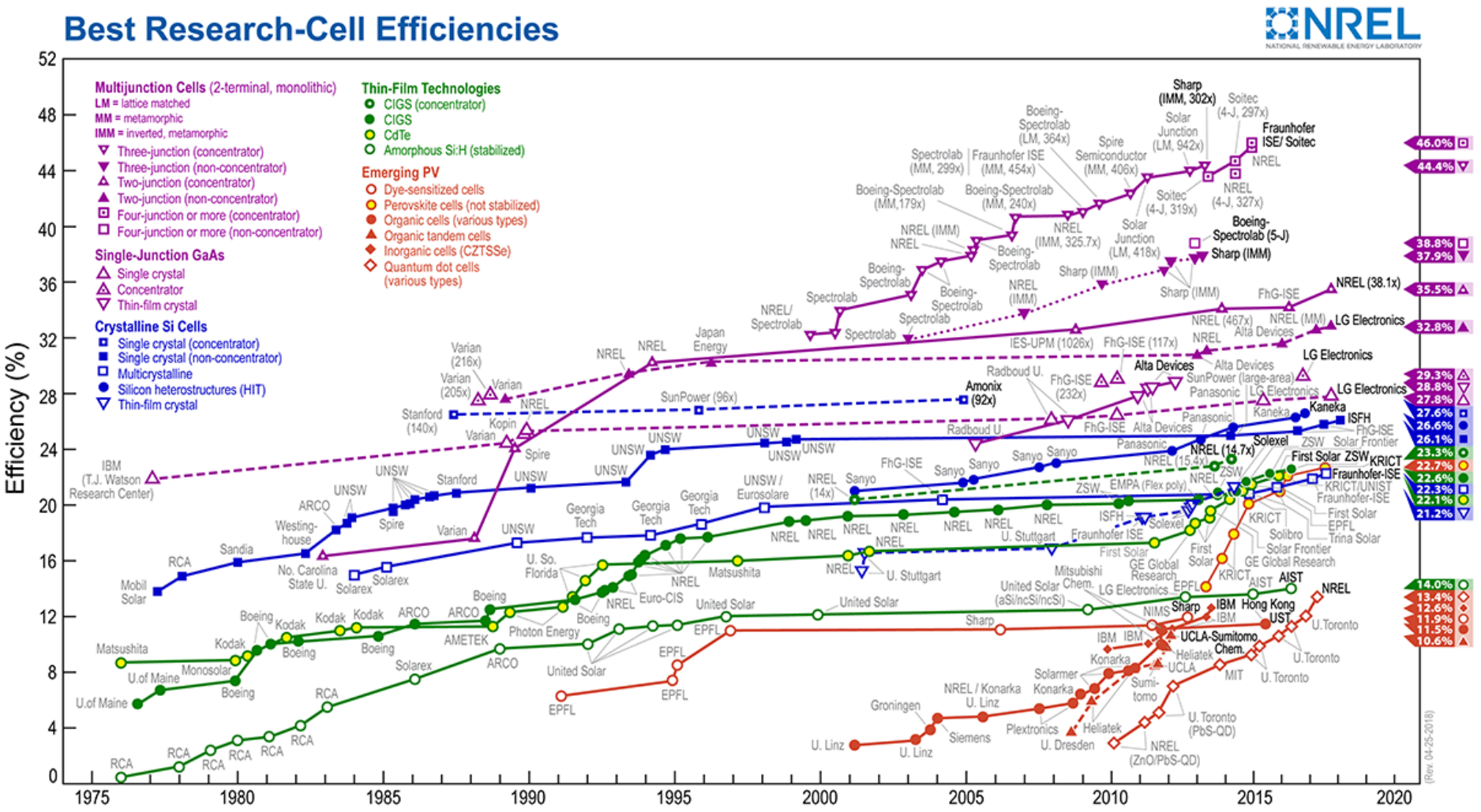

Figure 1.4 – Conversion efficiencies of best research solar cells worldwide for various PV technologies since 1976
(source **[15]**: National Renewable Energy Laboratory, United States Department of Energy)

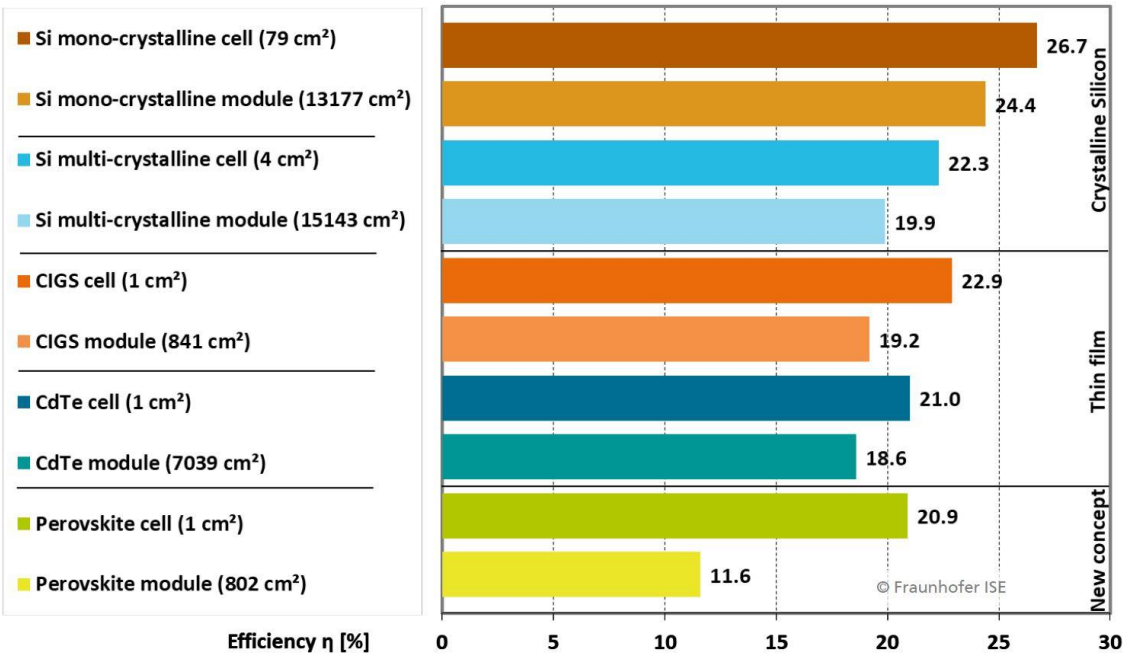

Figure 1.5 – Efficiency Comparison of Technologies: Best Lab Cells vs Best Lab Modules (source: Photovoltaic Report, Fraunhofer Institute for Solar Energy Systems, Germany)

And so, by looking at *Figure 1.4*, it is possible to verify that the highest conversion efficiency ever recorded for a PV cell was at 46%, in 2014, with a four-junction solar cell that was developed by Soitec and CEA-Leti, France, together with the Fraunhofer Institute for Solar Energy Systems, Germany, i.e. with CPV systems, module efficiencies of up to 46% have been reached [7][15][17].

According to data from *Figure 1.5*, the record lab cell and lab module efficiencies are, respectively, 26.7% and 24.4% for mono-crystalline. For multi-crystalline Si wafer-based technology, the record lab cell and lab module efficiencies are 22.3% and 19.9%, respectively. The highest lab cell efficiency in thin-films is 22.9% for CIGS and 21.0% for CdTe solar cells [7][15].

We can also conclude from *Figure 1.5* that there has been a significant increase in the efficiencies of several PV technologies in the last decade. As motivating as it may seem, it is still far from the efficiencies that can be obtained with other renewable energy sources. Additionally, the current PV systems are strongly dependent on daylight, which makes them sensitive to weather conditions like irradiance, temperature, humidity, dust deposition or shading. This affects their performance and so the efficiencies obtained in laboratory are always higher than those found outdoors.

Lately, costs have been experiencing a steep decline in PV systems. Yet, the optimization of efficiencies is still far from being achieved. Thus, this is the priority of the PV industry in order to take advantage of the enormous potential of this source of electricity production.

This is where nanotechnology can enter with the aim of helping PV devices by increasing the efficiency of solar cells, while reducing their manufacturing and electricity production costs [18].

The future is bright for nanotechnology! Its unique capability to fabricate new structures at atomic scale - 1 billionth to several tens of billionths of a meter - has already produced novel materials and devices with great potential applications in a wide number of fields [19].

This dissertation explores a new approach of nanotechnology in PV technology, that is the use of nanoantennas on solar photovoltaic panels.

1.2. Motivations and Objectives

In the last decade, alternatives to the classic solar panels have been discussed that would allow a greater use of the solar spectrum in order to produce electrical energy. In this case, the use of nanoantennas is proposed.

The objective of this thesis is to perform a performance analysis using COMSOL Multiphysics® software with nanoantennas with different types of metal, like aluminium or gold. After several simulations are made, the results obtained numerically with the program will be compared with those resulting from the theoretical models.

Finally, based on the results obtained, the most suitable nanoantenna will be chosen for use on a solar PV panel.

1.3. Outline of the Thesis

In order to achieve the objectives proposed, this work is organized in the following order:

Chapter 1 – Introduction: here it is presented the framework of the topic to be addressed, the objectives of the thesis and the structure of the document.

Chapter 2 – Application of nanoantennas for solar energy harvesting: provides some fundamental knowledge about optical nanoantennas for solar energy harvesting. It is thoroughly reviewed its history, materials used and design specifications, as well as its performance in terms of energy conversion efficiency.

Chapter 3 – Structure: introduces the structure that will be analysed and its expected behaviour, as well as the analytical model.

Chapter 4 – Simulation results: presents a brief explanation of the software used, COMSOL Multiphysics®, and also the results obtained by the developed software for the different topologies.

Chapter 5 – Conclusion and future work: presents the conclusions of this work and discusses possible future work to be done in this field.

2. Application of nanoantennas for solar energy harvesting

In this chapter, firstly the concept of light is introduced. Then, the nano-rectenna system is briefly explained, the history of nanoantennas is reviewed and the technical context of nanoantennas is presented as well as its performance in terms of energy conversion efficiency.

To finish, information related to fabrication methods, materials and a few design considerations are introduced, and an overview of current and potential applications is provided.

2.1. What is light?

No single answer to the question “What is light?” satisfies the many contexts in which light is experienced, explored and exploited. Light from the Sun warms the Earth, drives global weather patterns, and initiates the life-sustaining process of photosynthesis. On the universe scale, light’s interactions with matter have helped shape the structure of the universe [20].

For centuries, light has been studied by several physicists from around the globe. In the XVII century, Isaac Newton believed light was a set of particles, while Huygens believed light was a wave. His theory was initially rejected in favor of Isaac Newton's corpuscular theory of light, where it also states that white light consists of a mixture of colors [21]. Newton’s corpuscular model survived until the early XIX century. During this time, Thomas Young and Augustin-Jean Fresnel considered light as a wave phenomenon, known as the Huygens–Fresnel principle: Young introduces the concept of interference in the theory of light waves, while Fresnel used Young and Huygens' theories to calculate the distribution of electromagnetic waves in diffraction patterns. This was one of the investigations that led to convincingly establish the wave theory of light over the then predominant corpuscular theory. Young and Fresnel demonstrated, in their double-slit experiment, the interference and diffraction of light.

Decades later, Maxwell predicted that light itself was an electromagnetic (EM) wave, which was the first general frame for electricity, magnetism and light. It was confirmed experimentally by Hertz’s detection of radio waves.

Following Maxwell's theory, Gustav Kirchhoff demonstrates that the results obtained by the Huygens-Fresnel principle can be obtained through the solutions of the scalar wave equation. The Kirchhoff approximation is often applied to study the diffraction of light by an aperture bigger than the light wavelength in an infinitely thin, perfectly conducting screen. It assumes that the field inside the aperture is the same as the excitation field in the absence of the aperture. Further approximations of Kirchhoff’s integral then lead to the classical Fresnel and Fraunhofer diffraction integrals [22].

In 1944, Bethe derived an analytical solution for the EM field near a small aperture smaller than the light wavelength. Bethe formulated the theory to describe the field distribution in the vicinity of apertures in a perfect conductive metal. In 1950, Bouwkamp corrects and generalizes Bethe's theory, namely in the boundary conditions. Bouwkamp found that the boundary conditions proposed by Bethe exhibit discontinuities and do not constitute an approximate solution to the diffraction problem in the near-field region.

The Bethe-Bouwkamp theory has been used by various authors on recent diffraction studies on apertures considerably smaller than the wavelength of the EM radiation. The number of these studies have increased lately, namely with the introduction of optical antennas smaller than the light wavelength that is the main topic of this dissertation.

In 1998, Ebbesen demonstrated that the transmission through a metal plane with subwavelength-sized holes can be drastically increased if a periodic arrangement of holes is used. This phenomenon is widely known as the Extraordinary Optical Transmission. It originates from the constructive interference of scattered fields at the irradiated surface of the metal plane. The periodic arrangement of holes increases the energy density on the metal's surface through the creation of standing surface waves. This discovery would be fundamental, since it not only allowed great technological developments during the last decade, but also allowed a better understanding of the diffraction by small slits in relation to the light wavelength **[22] [53]**.

For most of history, visible light was the only known part of the electromagnetic spectrum. Today we know that the EM spectrum, represented in *Figure 2.1*, is classified by wavelength or frequency**.**

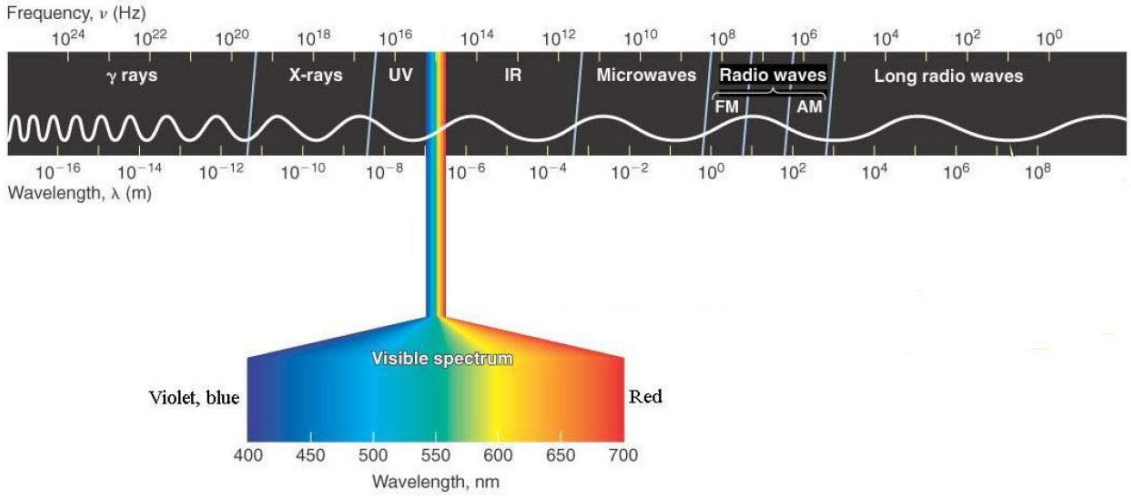

Figure 2.1 – Representation of the electromagnetic spectrum
(source: American Chemical Society, 2003)

The visible spectrum, that we perceive as light, is the electromagnetic radiation with wavelengths between 400 and 700 nm, which is visible to the human eye. This electromagnetic radiation is generated by electronic excitation within molecules or electrons in atoms.

With the arrival of quantum mechanics in the XX century, the controversy over the nature of light resurfaced, as the concept of wave–particle duality emerged. It states that every particle or quantum entity may be described as either a particle or a wave. De Broglie in a seminal paper explored the reconciliation of light-quanta, which was later used by Einstein to explain the photoelectric effect. He believed light is a particle (photon) and the flow of photons is a wave, thus demonstrating that light had a corpuscular behavior [23]. The main point of Einstein's light quantum theory is that light's energy is related to its oscillation frequency [24]:

$$E = h \cdot v \qquad (2.1)$$

where h is Planck's constant and v is the frequency of the light. For his explanation of the photoelectric effect Einstein received the Nobel Prize in Physics in 1921.

Photons, which are discrete parcels of energy that have dual nature as a particle and a wave, are the *quanta*[2] of EM radiation. The energy of a photon is directly proportional to the photon's frequency and inversely proportional to its wavelength. So, we can say that γ rays consist of very high-energy photons with higher frequencies and shorter wavelengths compared to radio waves.

Sunlight is attenuated as it travels through the Earth's atmosphere. This means that all UV radiation with a wavelength below 290nm is filtered out before it reaches the Earth's surface, as well as some regions above 800nm that are either reflected, absorbed or scattered by the Earth's atmosphere as seen on the solar light irradiance spectrum on *Figure 2.2* [25].

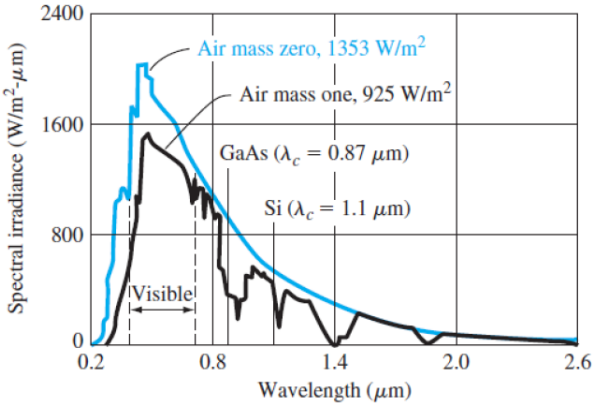

Figure 2.2 - Solar light irradiance spectrum [26]
(light blue: outside of the Earth atmosphere; black: inside the Earth's atmosphere)

[2] *Quanta*, plural of the word *quantum*, is a generic term used in physics to understand the smallest discrete quantity of some physical property that a system can possess.

2.2. Introduction to nanoantennas

Solar energy reaches the Earth, in the form of electromagnetic radiation, over a wide spectrum. Not all solar radiation reaches the Earth's surface: approximately 30% of this energy is reflected back to space from the atmosphere; another part is absorbed by atmospheric gases and re-radiated to the surface, while other parts are absorbed by the surface or organic life and re-radiated [27]. The electromagnetic spectrum that reaches the Earth's surface can be classified into three main bands: ultraviolet (UV) radiation, $\lambda < 400$ nm, of which the content is less than 10%; around 40% is visible light, 400 nm $< \lambda <$ 700 nm; and the remaining 50% consisting of infrared (IR) radiation.

PV technology has had a fast development in the last decade, namely with the increase of the solar panel efficiency. However, the intrinsic efficiency of a solar cells is still low, below ~20% for a monocrystalline cell of Si and below this value for the cheaper polycrystalline and amorphous cells. The use of mirror concentrators has a small impact in the intrinsic efficiency but allows the use of a smaller number of PV cells to output the same electric energy. However, mirror concentrators systems are expensive. Therefore, the PV industry will need cheaper and higher efficiency technologies to meet these requirements of the solar power market. This is where nanoantennas associated with solar cells could enter the market in the upcoming years.

With nanoantennas, the PV cells can convert in electricity a greater part of light that falls on the solar panel, eventually with a smaller number of PV cells than the basic system. One has to take into account that nanoantennas do not replace solar panels. They do not convert light into an electrical signal by themselves. Nanoantennas can function as light concentrators. When associated with solar panels, the overall eficiency is expected to be greater than the current solar panel conversion efficiency.

In the last decade, the advances in the nanoscale dimension enabled the development of new devices, such as nanoantennas or optical antennas, due to the emergence of a new branch of science known as nanooptics, which studies the transmission and reception of optical signals at the nanoscale. These devices have been the object of an intense research and development activity, with the goal to reach the captivating possibility of confining the electromagnetic radiation in spatial dimensions smaller than the wavelength of light [28]. Thus, nanoantennas are devices that have the ability to manipulate and control optical radiation at subwavelength scales.

Many of the properties and parameters of nanoantennas are similar to those of radio-frequency (RF) or microwave antennas. However, throughout this dissertation it will be seen that in the process of sizing the nanoantennas it will not be enough to reduce the size of the RF antennas to the optical domain, according the rules in the RF and microwave region, mainly because of the unique material properties of metals that influence the behavior of antennas at the

nanoscale: the existence at the interface between metals and dielectrics of surface plasmon-polariton electromagnetic waves, which gives rise to resonant effects not available at RF.

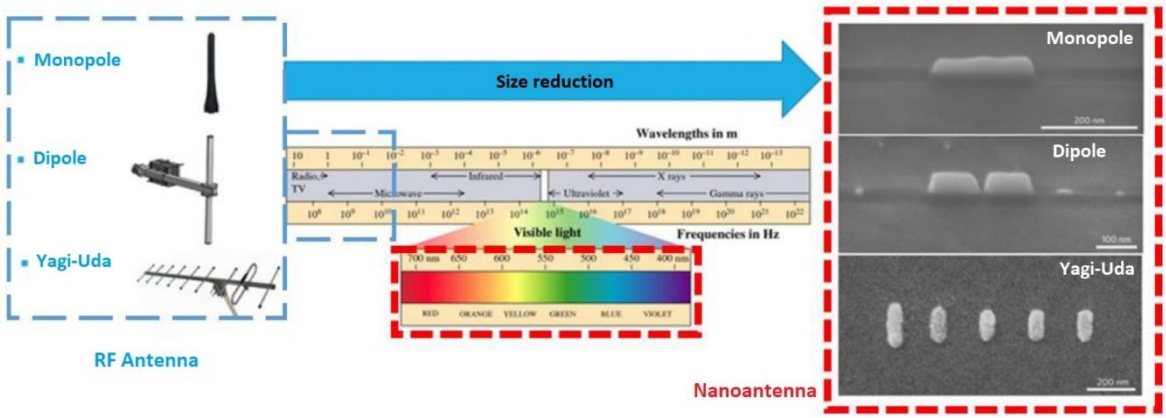

Figure 2.3 – Representation and comparison of RF antennas and nanoantennas (adapted from: **[29]** Gomes R., "Estudo de uma antena ótica para comunicação intersatélites", Instituto Superior Técnico, 2016)

The characteristics of RF antennas and the reason why they are used can be compared with nanoantennas as well. The main objective is to optimize the transfer of energy between an emitter and a receiver with the possibility of confining the energy of the electromagnetic field in a small region, that in the case of nanoantennas, it is a region of very small dimensions with very high precision [30] [31].

The use of optical antennas for solar energy harvesting has received a significant interest as they represent a viable alternative to the traditional energy harvesting technologies. Throughout this dissertation, we will be studying into more detail the application of optical nanoantennas with apertures. This type of nanoantenna takes advantage of the Extraordinary Optical Transmission phenomenon, in which a periodic array of subwavelength holes transmits more light than a large macroscopic hole with the same area as the sum of all the small holes.

Additionally, these devices allow the interaction of light or IR waves with nanoscale. With these capabilities, optical nanoantennas have also several other unique applications. According to Krasnok *et al.*, (2014) and Novotny *et al.* (2011), some other promising applications of nanoantennas for the near future include: medicine, in the therapy for malignant neoplasms; biological and chemical sensing (near-field microscopy and high-resolution biomedical sensors); nanoscale imaging and spectroscopy; optical imaging or light emission [31] [39].

Economical large-scale fabrication of nanoantenna devices would support applications such as building-integrated photovoltaics and supplementing the power grid [27].

2.3. Rectenna system for solar energy harvesting

The nanoantenna itself does not convert the collected AC current into DC current, and so it needs to be complemented with a rectifying element. The whole structure is commonly referred to as a rectenna [32].

A **rectenna** is a circuit containing an optical antenna, filter circuits and a rectifying diode or bridge rectifier for the conversion of electromagnetic energy propagating through space (solar energy) into DC electric power (through the photovoltaic effect).

Incident light on the optical antenna causes electrons in the device to oscillate in a collective movement at the same frequency as the incoming light. This is caused by the oscillating electric field of the incoming electromagnetic wave. The movement of electrons is an alternating current (AC) in the antenna circuit. To convert this into DC current, the AC must be rectified with a diode. The resulting DC current can then be used to power an external load [18].

A schematic representation of a nano-rectenna system is depicted in *Figure 2.4*:

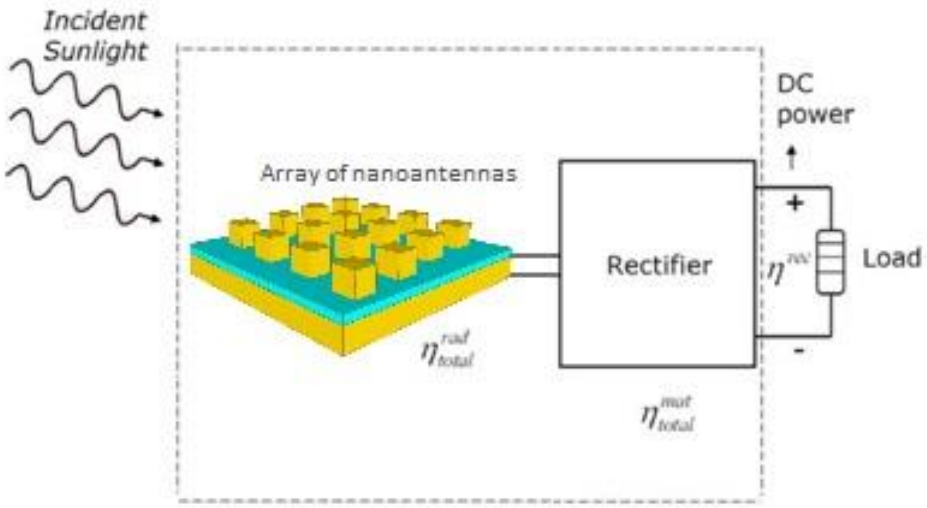

Figure 2.4 – Representation of the nano-rectenna system
(adapted from: **[33]** Sen Yan *et al.,* "Optimizing the bowtie nano-rectenna topology for solar energy harvesting applications"; 2017)

Still in the research phase, having a completely different form of operation than traditional solar cells, nanoantennas are devices that are capable to absorb various wavelengths of light, according to their size [4]. They are specially designed for the capture of IR radiation of wavelengths ranging from 700 to 1000 nm, approximately 50% of the total incoming solar radiation that reaches the Earth's surface. According to Kotter *et al.*, 2008, traditional solar cells have proven to be inefficient at these wavelengths [5] [32].

There is a high theoretical efficiency of nanoantennas alongside with its large-scale production and low-cost fabrication, which is an advantage in relation to the traditional silicon solar cells.

The energy reaching the Earth in both the visible and IR regions and the reradiated IR energy are under-utilized by current technology. Therefore, this new type of technology is a promising alternative to conventional solar energy conversion technologies with the prospect of revolutionizing the way solar energy is captured in a completely clean and renewable way, not only by capturing the energy of the Sun during the day but also the radiation of the Earth at night [4].

2.4. Brief history of solar nanoantennas

Rectennas were originally proposed in the 1960s for power transmission by radio waves for remote powering of aircraft for surveillance or communications platforms. Later, concepts were proposed to extend the rectennas into the infrared (IR) and optical region of the electromagnetic spectrum for use as energy collection devices (optical rectennas) [34] [35].

The idea of using nanoscale antennas to convert optical waves into electricity was introduced in 1972 by Robert L. Bailey [36]. In 1973, Bailey received a patent for their idea of an "electromagnetic wave energy converter". In his paper, he describes this device that consisted of pairs of pyramids as modified dipole antennas, with each pair electrically connected to a diode, low-pass filter and a load [37].

In the meantime, multiple patents for electromagnetic energy converter devices have been issued. In 1984, Alvin Marks was the first to patent a device that explicitly stated the use of sub-micron antennas for the direct conversion of solar energy to electricity. Marks' structure was essentially a conventional broadside array antenna with the output signal of multiple dipoles feeding a transmission line to transmit its combined power to a rectifier. This device brought structural improvements to Bailey's invention and showed a substantially higher performance [37] [38]. Following his first invention, Marks also patented other devices for the collection and conversion of electromagnetic energy.

Lin *et al.*, in 1996, reported the first experimental evidence for resonance light absorption and rectification in a fabricated nanostructure with a parallel dipole antenna array on a silicon substrate [39]. The device was reported to absorb electromagnetic radiation at a resonant frequency dependent on the light polarization and the angle of the incoming light.

Since then, there has been some investigations of nanoantenna structures by numerous research groups worldwide. ITN Energy Systems Inc. in the USA developed an optical rectenna that consisted of an optical antenna to efficiently absorb the incident solar radiation and high-frequency metal-insulator-metal (MIM) rectifier diodes that rectified the AC field across the antenna, providing DC power to an external load [37]. ITN's device achieved over 50% conversion efficiency operating in the microwave range at a 10 GHz frequency. However, a very low efficiency around 1% was observed at 10μm wavelengths (30 THz frequency) [37] [40].

Due to the lack of technical ability to manufacture structures at the nanoscale, it was not until 2005 that the concept of using nano-rectennas in solar energy harvesting has been intensively investigated [41]. A detailed numerical investigation was published in Kotter et al., in 2008, that at a single frequency in the solar spectrum up to 90% of the energy can be made available at the output of a silver dipole nanoantenna [5] [33]. In addition, Kotter et al. designed a spiral-square nanoantenna that exhibits high directivity[3] and good angular reception characteristics. Due to its wider angle of incidence exposure in comparison to conventional photovoltaic devices, this type of antenna allows to concentrate the electric field in one specific point in its structure, allowing an optimization of energy collection. This is a great benefit as it may reduce the need for additional solar tracking devices in nanoantenna electromagnetic collector structures [5] [42].

Lately, more topologies of nanoantenna structures have been studied by several research groups worldwide in order to produce efficient nanoantennas. Still, there was the problem that all these devices dealt with efficiencies that were a function of a single frequency and not an overall efficiency on a frequency range over which solar radiation is spread out, mainly in the visible and near IR bands. Such a parameter would be necessary to evaluate the performance of the whole rectenna system. Thus, Kotter *et al.*, in 2008, defined the notion of total harvesting efficiency, stating levels of about 60% - 70% for silver nano-dipoles [5] [33]. However, it is known that silver is more susceptible to oxidation. And so, in 2012, Vandenbosch and Ma suggested an aluminium based rectenna, reporting a slightly lower total efficiency of around 50%. With these results, they have demonstrated that energy conversion with this type of technology devices is possible [33] [43].

[3] The Directivity measures the power density of the antenna radiated in the direction of its strongest emission.

2.5. Technical context

2.5.1. Experimentally studied nanoantenna materials and designs

Firstly, the electromagnetic radiation is collected by the nanoantenna device. However, the output obtained from a single nanoantenna element is not enough to drive the rectifier and to provide DC power to an external load. The efficiency of a single optical antenna is generally low and its functionality is limited. And so, nanoantennas are arranged into arrays to increase their signal. The total field captured by the array is the addition of the fields captured by each nanoantenna [42].

A possible configuration for an array of individual nanoantennas consists of three main parts: a metal antenna layer (usually made of gold, silver or aluminium), a dielectric standoff layer (usually plastic polymers or glass) where the spacing creates an optical resonance cavity and a ground-plane that is used to reflect radiation back towards the nanoantenna [5] [32].

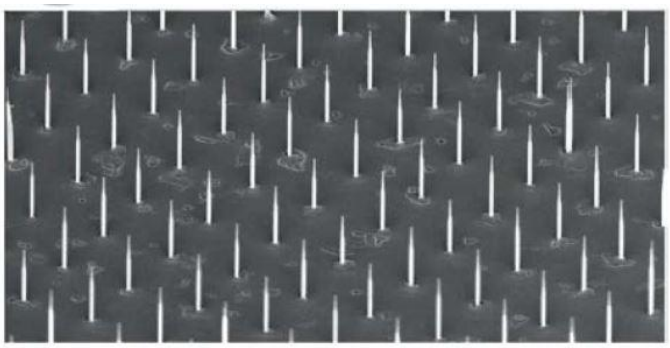

Figure 2.5 – Monopole nanoantenna arrays
(adapted from: **[44]** *Krasnok et al.,* "Optical Nanoantennas", 2013, p. 545)

2.5.1.1. Plasmonic nanoantennas

A large variety of nanoantenna geometries has been researched for multiple potential applications. Currently, nanoantennas structures are mainly made of plasmonic materials, i.e., specially designed metal (usually gold or silver) nanoparticles with unique optical properties. Plasmonic materials exhibit strong light absorption in the visible region of the spectrum [32].

According to the principle of reciprocity, any nanoantenna may operate both as a receiver and as a transmitter [44]. Thus, plasmonic nanoantennas emit, receive and, more generally, control light with nanoscale elements, whose size is much smaller than the wavelength of incident light [28].

The advances in the manufacturing techniques allowed the construction of different formats. The main types of plasmonic nanoantennas that have been proposed and investigated experimentally are represented in *Figure 2.6:*

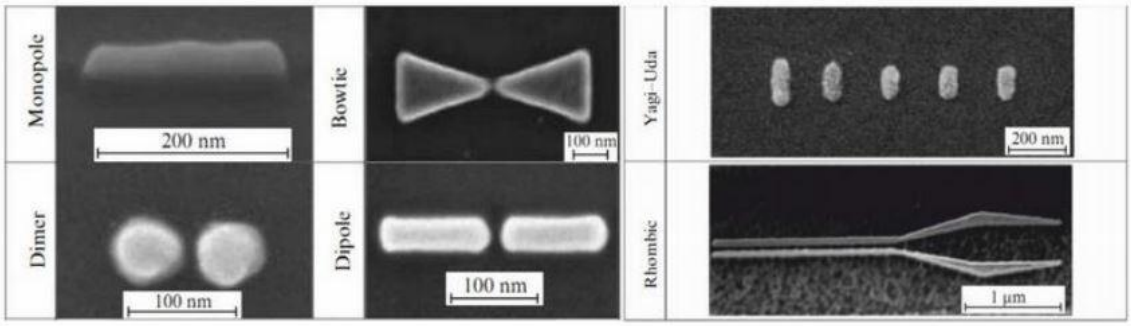

Figure 2.6 – Main types of plasmonic nanoantennas
(source: **[44]** *Krasnok et al.,* "Optical Nanoantennas", p. 545, 2013)

a) Plasmonic monopole nanoantennas

The most basic type of plasmonic nanoantenna, a monopole, is a single metallic nanoparticle that can enhance the electromagnetic field strength in its surrounding area upon excitation of plasmon resonances. Monopole nanoantennas have advantages over other geometries, because they are easier to engineer and are well isolated from interference due to the ground plane. Their characteristics are dependent on the shape, size, material, and dielectric environment of the nanoparticle [44].

Another great utility of the monopole optical antenna is when it is integrated in a Nearfield Scanning Optical Microscopy (NSOM), to be used as a near-field probe for measurements [45]. An effective nanoantenna can be used in spectroscopy: it needs to interact strongly with incident EM radiation in order to measure its intensity.

T. Kalkbrenner *et al.*, in 2005, reported the first realization of this idea, using a single gold nanoparticle as a subwavelength antenna. In their laboratory, they have made an experiment of NSOM by detecting the intensity of the light scattered from a gold nanoparticle with a 100nm diameter at a fixed wavelength [46]. Thus, the effect of EM field enhancement near the tip of a metal can be observed in this experiment. A schematic representation is shown in *Figure 2.7*:

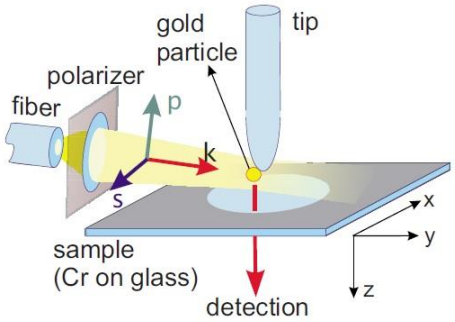

Figure 2.7 – Schematic of the experiment: a white light source illuminates a gold nanoparticle antenna from the side (source: **[46]** T. Kalkbrenner, *et al.*, "Optical microscopy via spectral modifications of a nanoantenna," Phys. Rev. Lett. 95, 2005)

b) Plasmonic dipole nanoantennas

Dipole configurations are widely used in radio frequency and microwave ranges. Therefore, it is not a surprise that analogues of such antennas also appeared in the optical range. This type of optical antennas is widely used in near-field optical probes, just like the monopole. The dipole optical antenna is constituted either by dimers or two monopoles separated by a small space (gap). Usually, there is a high field confinement in the gap between the two metallic nanoparticles [44].

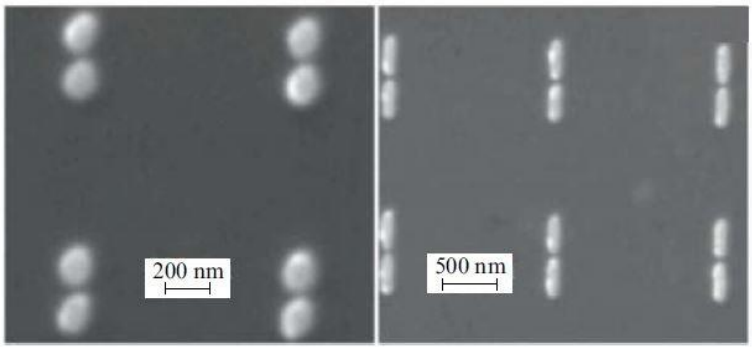

Figure 2.8 – SEM[4] images of dipole nanoantenna arrays in the form of dimers (left) and a combination of two monopoles (right) (source: **[44]** Krasnok *et al.,* "Optical Nanoantennas", 2013)

The authors of **[44]** state that the dipole nanoantenna design is often considered as the most suitable for data communication, as it could improve the method of coupling optical information transmission lines directly to nanooptic devices.

The design of plasmonic nanoantennas may rely on the same principles used in RF antennas. For example, the length of the dipole RF antenna is approximately half the wavelength of the incident radio waves. Whereas, the length of the dipole plasmonic nanoantenna is smaller than the wavelength, λ, of incident light in free space [28].

[4] SEM (scanning electron microscope) is a type of electron microscope that produces images of a sample by scanning the surface with a focused beam of electrons.

c) Plasmonic bowtie nanoantenna

Another typical structure is the bowtie nanoantenna, consisting of two triangular shape nanoparticles aligned along their axes and forming the feed gap with their tips. These optical antennas are a variant of the dipole nanoantennas. Such geometry ensures a wider bandwidth together with large field localizations in the feed gap compared to the straight dipole.

The bowtie topology is considered to be one of the most efficient nanoantenna geometries for solar energy harvesting. According to Sen Yan *et al.* (2017), in their study it is shown that the bowtie topology can increase the total radiation efficiency and rectenna efficiency compared to the straight dipole by a considerable 10% [33].

d) Plasmonic Yagi-Uda nanoantenna

Radio frequency Yagi-Uda type antennas are usually used to receive TV signals from remote stations, due to its high directivity. Their plasmonic counterparts, like RF Yagi-Uda antennas, consist of a reflector and one or several directors.

Yagi-Uda optical antennas can be useful in many applications: in wireless communications, in the fields of biology and medicine, in nanophotonic circuits, in quantum information technology, in data storage (as an optical chip), in photodetectors and in PV systems.

e) Plasmonic spiral-square nanoantenna

This design of nanoantenna allows the EM radiation to be harvested in one specific point in its structure, the gap (feed point) between two metallic arms. Thus, this topology has a wider angle of incidence exposure in comparison to other formats, which makes it an ideal geometry for solar energy harvesting.

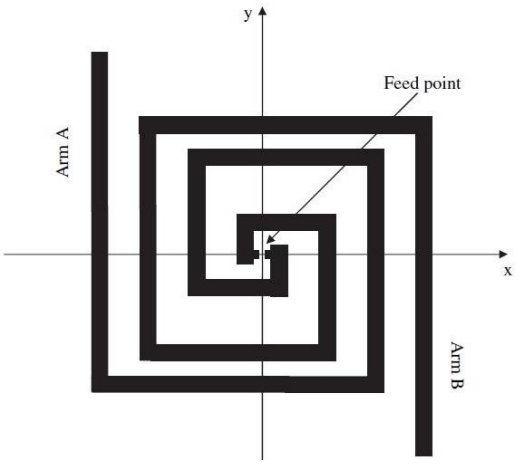

Figure 2.9 – Geometry of a square-spiral nanoantenna
(source: **[3]** Michele Gallo *et al.*, “Design of optical antenna for solar energy collection”, 2011)

They also demonstrate a high directivity that can be further improved by increasing the number of arms.

2.5.1.2. Dielectric nanoantennas

A new research direction of optical antennas has recently been suggested with the introduction of **dielectric nanoantennas**. Optical antennas constructed with dielectric materials have several advantages over their metallic counterparts due to unique features not found in plasmonic nanoantennas [32].

Dielectric nanoantennas are fabricated from optically transparent materials that have low dissipative losses at optical frequencies. Unlike gold or silver, dielectric nanoantennas are usually made from silicon nanoparticles which is widely used in nanoelectronics to fabricate transistors and diodes. Also, silicon has a high permittivity and exhibits very strong electric and magnetic resonances at the nanoscale and thus improves radiation efficiency and antenna directivity, expanding the range of applications for nanoantenna structures [32] [47]. Not only silicon is used in dielectric nanoantennas. Other high permittivity dielectric nanoparticles may include germanium (Ge), aluminium antimonide (AlSb), aluminium arsenide (AlAs), among others [47].

The authors of **[47]** in their study used silicon nanoparticles to demonstrate the performance of all-dielectric nanoantennas. They have analysed an all-dielectric analogue of the plasmonic Yagi-Uda nanoantenna consisting of an array of nanoelements: four directors and one reflector particle made of silicon. In this type of structure, the optimal performance is obtained when the director nanoparticles sustain a magnetic resonance and the reflector nanoparticle sustains an electric resonance [32]. A schematic representation of this antenna is shown in *Figure 2.10*:

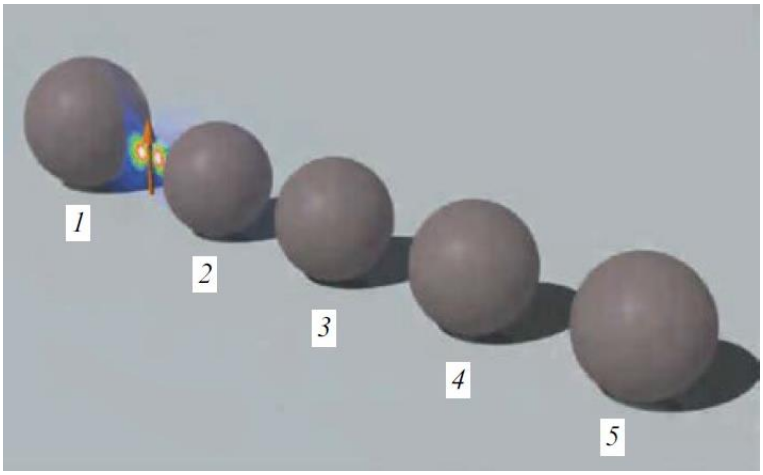

Figure 2.10 – 3D view of an all-dielectric optical Yagi-Uda nanoantenna, consisting of the reflector 1 of the radius Rr = 75 nm, and smaller director 2-5 of the radii Rd = 70 nm. (adapted from: **[44]** A.E. Krasnok et al., “Optical nanoantennas”, 2013)

The dipole source is placed equally from the reflector and the first director surfaces at the distance D. The separation between surfaces of the neighbouring directors is also equal to D.

The operational regime of a dielectric Yagi-Uda nanoantenna strongly depends on the distance between its elements**.** According to Krasnok *et al.* (2012), in their study it was verified that the radiation efficiency of the dielectric Yagi-Uda nanoantenna slowly decreased with decreasing distance between its elements, while the radiation efficiency of a plasmonic antenna of similar design and dimensions was greatly affected by the decrease in distance between particles. This is due to increased metal losses caused by proximity of adjacent metallic nanoparticles.

However, for larger separation distances, D, the radiation efficiencies of both types of nanoantennas were very identical. Although dissipation losses of silicon are much smaller than those of silver, the dielectric particle absorbs the EM energy by the whole spherical volume, while absorption only occurs at the surface of metallic particles. As a result, there is no substantial difference in the performance of these two types of nanoantennas for relatively large distances between its elements.

To sum up, based on the results of this study, a conclusion could be made that all-dielectric nanoantennas demonstrate major advantages over their metallic counterparts: much lower polarization losses at the optical frequencies and nanoparticles made of high-permittivity dielectrics may support both electric and magnetic resonant modes [47].

2.5.1.3. Aperture nanoantennas

There is another type of optical antennas that is interesting for the topic of this dissertation: **aperture optical antennas**. Light passing in a small aperture is the subject of intense scientific interest since the very first introduction of the concept of **diffraction** by Grimaldi in 1665 [48].

The first theory of diffraction due to a slit, that is much less than the light wavelength, in a thin metal layer was developed by Bethe. This theory predicted that the power transmitted by the slit would be decreasing as the slit diameter diminished relative to the wavelength of the EM radiation. This theory proved to be incorrect when Ebbesen, in 1998, observed the extraordinary optical transmission phenomenon (EOT). This discovery would be fundamental, since it not only allowed great technological developments during the last decade, but also allowed a better understanding of the diffraction by small slits in relation to the light wavelength [53].

According to **[48]**, there are three main types of aperture antennas: single subwavelength aperture, single aperture surrounded by shallow surface corrugations, and subwavelength aperture arrays.

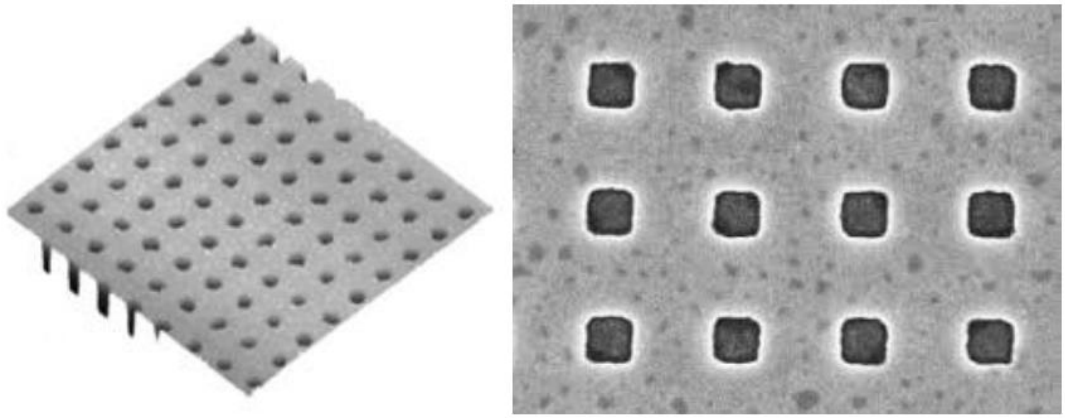

Figure 2.11 – Schematic view of 200 nm diameter aperture arrays with 1 um period
(adapted from: **[48]** J. Wenger, “Aperture optical antennas”, École Centrale de Marseille, p. 7)

The figure above shows a subwavelength array with periodic apertures. Arranging the apertures in an array with a periodic pattern is another way to provide for the momentum needed to match the far-field radiation with surface EM waves [48].

J. Wenger, the author of **[48],** states that two types of resonant phenomenon contribute to explain the transmission peaks observed in far-field and the intensity enhancement in the near-field: the first one relies on the resonant excitation of surface plasmon waves at the metal-dielectric interface, which is obtained at specific incident angles and wavelengths according to grating diffraction rule; while the second comes from localized plasmon modes on properly shaped apertures. Combination of these two resonant phenomena are of major interest to locally enhance light-matter interaction, and control the radiation spectrum, direction and polarization.

In the next subchapter of this dissertation, surface plasmon will be explained in detail.

2.5.2. Surface plasmon resonance

As seen in section 2.3, incident light on the optical antenna causes the excitation of free electrons in metallic particles. More precisely, EM waves induce time-varying electric fields in the nanoantenna that apply a force on the gas of electrons inside the device, causing them to move back and forth at the same frequency range as the incoming light. This phenomenon is known as **surface plasmon**. At specific optical frequencies the nanoantenna resonates at the same frequency as the incoming light which enables the absorption of the incoming radiation [32].

It should be taken into account that, at optical frequencies, metals do not act as perfect conductors: their conductivity changes dramatically and so are unable to respond to the time-varying electric field immediately. The wave propagation within the material is affected, which means that the penetration of EM radiation into metals can no longer be neglected. This EM response is dictated by surface plasmons that make a direct downscaling of traditional antenna designs impossible (see *section 2.1*). Thus, at optical frequencies an antenna no longer responds to external wavelength but to a shorter effective wavelength that depends on the material properties [31]. The authors of **[49]** proved this fact in their recent experiment at infrared frequencies.

EM radiation penetrates the metal of the nanoantenna and gives rise to oscillations of the free-electron gas. These electron oscillations can give rise to plasmon resonances, depending on the size, shape, and index of refraction of the particle as well as the optical constants of its surrounding [46]. When these oscillations are optimized, i.e., when the metal structure is sized to achieve the resonance condition, it is called **Surface Plasmon Resonance (SPR)**. It is also important to mention that there are two types of surface plasmons: when the EM waves strike a metallic film and are confined to the surface of this film is called **Surface Plasmon Polariton (SPP)**; when the coupling is made with a metal nanoparticle with a diameter much smaller than the incident wavelength is called **Localized Surface Plasmon (LSP)** [29].

Surface plasmons are highly confined energy fields made by the oscillation of electrons on the surface of nanoantennas. When a metallic nanoparticle is illuminated by light, surface plasmons will be coupled with the photons of incident light in the form of a propagating surface wave [30]. SPPs are infrared or visible-frequency EM waves trapped at or guided along metal-dielectric interfaces [50]. This coupling of plasmons, either SPPs or LSPs, and photons results in charge oscillation in the visible and infrared regimes depending on the metal used.

SPPs are shorter in wavelength than the incident light (photons). Hence, SPPs provide a significant reduction in effective wavelength and have tighter spatial confinement and higher local field intensity [50].

Recent development of nanofabrication techniques enabled construction of a variety of metal structures at the subwavelength scale and opened the research area called **plasmonics**, a subfield of nanophotonics studying the manipulation of light coupled to electrons at the nanoscale. The properties of optical antennas are still under the intensive study and so research efforts to relate plasmonics with subwavelength optical antenna are in a developing stage [30].

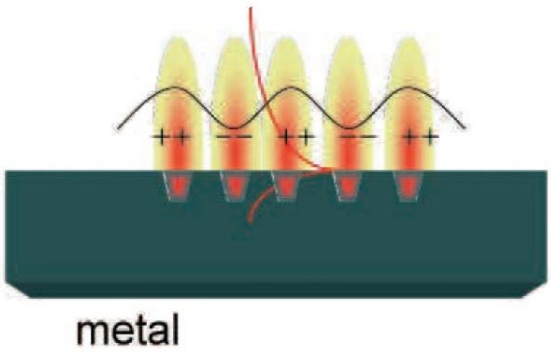

Figure 2.12 – Schematic view of a single antenna element represented by a metal rod. Incident light gives rise to a standing surface charge wave: SPP
(source: **[30]** Q-Han Park, “Optical antennas and plasmonics”, 2009)

2.5.3. Rectifier system

We have seen in section 2.3 the rectenna system where the nanoantenna is coupled to a rectifier and connected to an electric circuit for the purpose of energy conversion.

The AC current generated in the nanoantenna arrays is collected and rectified into DC current by the rectifier system. This system has different rectifiers whose outputs can be DC-coupled together, allowing arrays of nanoantennas to be networked to further increase output power [27].

As optical radiation requires high-speed rectification, high-frequency metal-insulator-metal (MIM) diodes – also known as tunnelling diodes - are commonly used for this purpose. Schottky diodes could also be a candidate for the rectifier, but they are limited to the far IR frequencies. Therefore, MIM diodes are better candidates to operate at these frequencies [51].

An MIM diode, represented in *Figure 2.13*, is made of two metal electrodes separated by a few nanometres by a thin dielectric oxide insulator. The charge carriers, i.e., electrons, are transported across the insulator, by electron tunnelling, on a femtosecond timescale.. This extremely fast charge transport across the tunnel barrier allows MIM diodes to operate at optical frequencies [42].

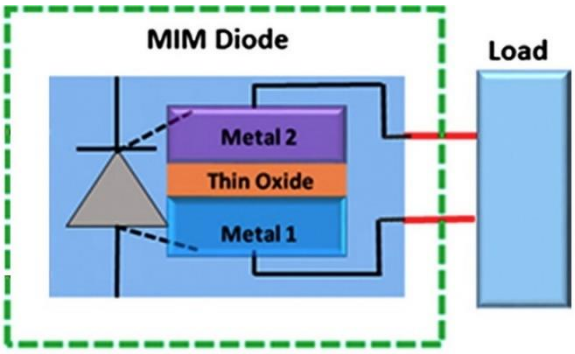

Figure 2.13 – Brief representation of the rectifier system
(adapted from: **[52]** A. Khan *et al.*, "Metal-insulator-metal diodes with sub-nanometre surface roughness for energy-harvesting applications"; 2017)

The probability of an electron tunnelling across the insulator depends exponentially on the distance while in the insulator. A change in the applied voltage in the diode will linearly change the tunnel distance and so the current is an exponential function of the voltage. Thus, the tunnel current depends exponentially on this distance, leading to nonlinear I–V characteristics [51].

The energy-band profile of the MIM diode is shown in *Figure 2.14*.

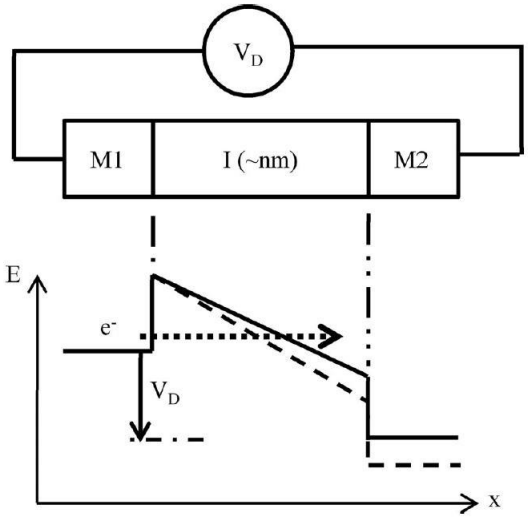

Figure 2.14 – Energy-band diagram of a single-insulator MIM diode.
(source: **[51]** Moddel & Grover, "Applicability of MIM Diodes to Solar Rectennas", IEEE Journal of Photovoltaics, Vol. 1, No. 1, 2011)

The device works when a large enough field causes tunnelling of electrons across the barrier layers. High-speed rectification is obtained when a difference in work functions between the metal junctions produces nonlinear effects. As the insulated layers become thinner, the probability increases such that the tunnelling effect can be maintained at optical frequencies. There are also other permutations of the MIM diode, such as the MIIM with two insulating layers [27].

According to Moddel & Grover (2011), the MIM diodes must have three key characteristics in order to have an efficient rectifier system: **high responsivity** that is a measure of the rectified DC voltage or current as a function of the input radiant power; **low resistance**, in order to have a good impedance matching between the antenna and the diode; **asymmetry in the I-V curve**, so the diode must have asymmetric characteristics for the rectenna be operated without applying an external DC bias[5]. This asymmetry can be easily obtained if different metals are used on the two sides of the insulator. This property is linked to the responsivity of the diode: the higher the asymmetry, the higher the diode's responsivity and so the barrier heights will increase. However, keeping the diode resistance low requires low barrier heights on both sides, which limits the asymmetry. Hence, an equilibrium must be made when designing the MIM diode [51].

Examples of material combinations used for diode rectifiers include Ni/NiO/Ni, Nb/Nb2O5/Pt, Nb/TiO2/Pt, Cu/TiO2/Pt, Nb/MgO/Pt and Nb/Al2O3/Nb [42].

[5] Bias refers to a fixed DC voltage or current applied to a terminal of an electronic component such as a diode in a circuit in order to establish proper operating conditions for that component.

2.5.4. Efficiency

The radiation efficiency of nano-antennas is a key parameter for solar energy harvesting. It is the first factor in the total efficiency product by which nanoantennas can convert incident light to useful energy. This efficiency depends directly on the type of metal used as conductor and the dimensions of the nanoantenna [42].

The main advantage of this type of technology in comparison to the conventional solar photovoltaic cells is its far bigger efficiency by which the transformation of electromagnetic energy into DC electric power is performed. Typical efficiencies for traditional silicon cells are in the order of 20%, whereas nanoantennas go from a stunning 70% for silver nano-dipoles [5] to a more realistic 50% for aluminium dipoles [41]. Most solar radiation is in the visible and in the IR wavelength region and so, nanoantennas need to be designed for this part of the spectrum, with the aim of being an alternative to conventional solar photovoltaic cells.

The total efficiency of a rectenna consists of two parts:

1) the efficiency by which the light is captured by the nanoantenna and brought to its terminals, also known as radiation efficiency, $\eta^{rad}{}_{total}$;
2) the efficiency by which the captured light is transformed into low frequency electrical power by the rectifier, $\eta^{mat}{}_{total}$.

According to *Kotter et al.*, the total radiation efficiency could be given by,

$$\eta^{rad}{}_{total} = \frac{\int_{\lambda_{start}}^{\lambda_{stop}} P_{inc}(\lambda) \cdot \eta^{rad}(\lambda)\, d\lambda}{\int_{\lambda_{start}}^{\lambda_{stop}} P_{inc}(\lambda)\, d\lambda} \qquad (2.2)$$

where λ is the wavelength of the incident light and the upper and lower integration limits λ_{start} and λ_{stop} should cover the optical bandwidth for the solar energy harvesting.

$P_{inc}(\lambda)$ is a function of the wavelength that follows Planck's law for black body radiation:

$$\mathrm{P}_{inc}(\lambda) = \frac{2\pi hc^2}{\lambda^5} \cdot \frac{1}{e^{\frac{hc}{\lambda kT}} - 1} \qquad (2.3)$$

T is the absolute temperature of the black body (in K) that in this case is the temperature of the surface of the sun; *h* is Planck's constant (6.626×10^{-34} Js); *c* is the speed of light in vacuum (3.0×10^{8}) and *k* is the Boltzmann constant (1.38×10^{-23} J/K).

$\eta^{rad}(\lambda)$ is the radiation efficiency of the antenna as a function of the wavelength that is given by:

$$\eta^{rad} = \frac{\mathrm{P}^{rad}}{\mathrm{P}^{inj}} = \frac{\mathrm{P}^{rad}}{\mathrm{P}^{rad} + \mathrm{P}^{loss}} \qquad (2.4)$$

where P^{rad}, P^{inj} and P^{loss} are the radiated power, the power injected at the terminals and the power dissipated in the metal of the nanoantenna, respectively.

In order to generate DC power in the load, a rectifier is connected to the input port to rectify the current flowing in the antenna's structure that oscillates around hundreds of THz. Like the total radiation efficiency, we may also define the total matching efficiency,

$$\eta^{mat}{}_{total} = \frac{\int_{\lambda_{start}}^{\lambda_{stop}} P_{inc}(\lambda) \cdot \eta^{rad}(\lambda) \cdot \eta^{mat}(\lambda)\, d\lambda}{\int_{\lambda_{start}}^{\lambda_{stop}} P_{inc}(\lambda) \cdot \eta^{rad}(\lambda)\, d\lambda} \qquad (2.5)$$

where is η^{mat} the matching efficiency of the nanoantenna rectifier system:

$$\eta^{mat} = \frac{4R_{rec} \cdot R_{ant}}{|Z_{rec} + Z_{ant}|^2} \qquad (2.6)$$

and Z_{rec} is the impedance of the rectifier and Z_{ant} is the input impedance of the nanoantenna. R_{rec} is the real part of the rectifier impedance and R_{ant} is the real part of the nanoantenna input impedance. All these quantities are marked in *Figure 2.15*, an equivalent circuit of the total rectenna system, where both the transmitting and receiving processes can be easily described.

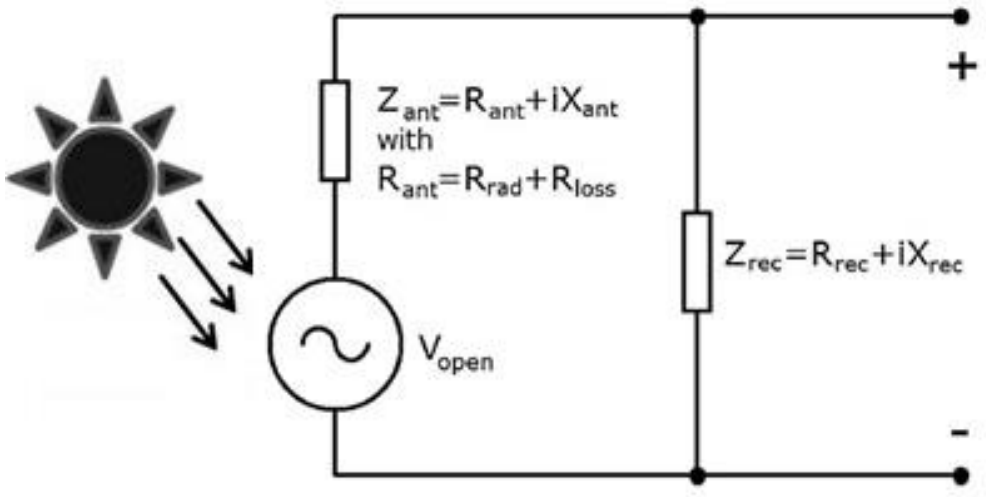

Figure 2.15– Equivalent circuit for the rectenna system
(adapted from: **[33]** Sen Yan *et al.,* "Optimizing the bowtie nano-rectenna topology for solar energy harvesting applications"; 2017)

V_{open} is the voltage generated by the receiving antenna at its open terminals, while V_{rec} is the voltage seen at the terminals when a current is flowing to the rectifier. This current generates power in the resistors R_{ant} and R_{loss}. The useful power is the power going to the impedance of the rectifier Z_{rec} and it is given by:

$$P_{rec} = \frac{R_{rec}}{2} \cdot \frac{V_{open}^2}{|Z_{ant} + Z_{rec}|^2} \qquad (2.7)$$

This power is maximal under optical matching conditions, i.e. $Z_{rec} = Z^*_{ant}$, and is then:

$$P_{rec} = \frac{V^2_{open}}{8R_{ant}} \qquad (2.8)$$

Finally, we define the total rectenna efficiency, $\eta^{rec}{}_{total}$ in Eq. *(2.8)* by combining the equations *(2.1)* with *(2.4)*. That is a definition of the global performance of the nanoantenna – rectifier system.

$$\eta^{rec} = \eta^{rad}{}_{total} \cdot \eta^{mat}{}_{total} \qquad (2.9)$$

3. Structure / Model

3.1. Solar cell

A solar cell, shown in *Figure 3.1*, is a PIN structure device with no voltage directly applied across the junction. The solar cell converts light into electrical power and delivers this power to a load. This process requires a material that can absorb the light photons. The interaction of an electron with a photon leads to the promotion of an electron from the valence band into the conduction band leaving behind a hole, i.e., the absorption of a photon by a semiconductor material results in a generation of an **electron-hole pair**. After an electron-hole pair is created, the electron and the hole move from the solar cell into an external circuit, producing a photocurrent *I*. The electron then dissipates its energy in the external circuit and returns to the solar cell [54].

The working principle of a solar cell is based on the **photovoltaic effect**, i.e., the generation of a potential difference at the junction of two different materials in response to EM radiation [55].

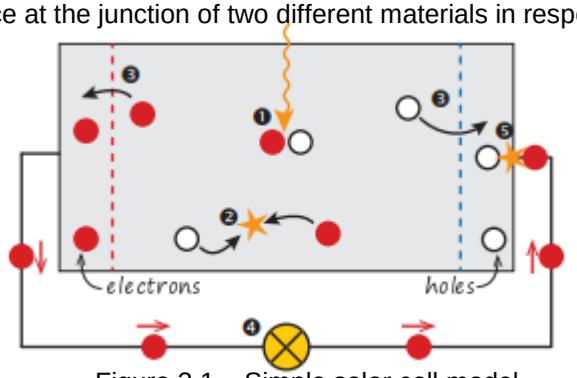

Figure 3.1 – Simple solar cell model
(source: **[55]** The Working Principle of a Solar Cell, TU Delft)

(1) Absorption of a photon leads to the generation of an electron-hole pair
(2) Recombination of electrons and holes
(3) Electrons and holes can be separated with semipermeable membranes
(4) The separated electrons can be used to drive an electric circuit
(5) After all electrons passed through the circuit, they will recombine with holes.

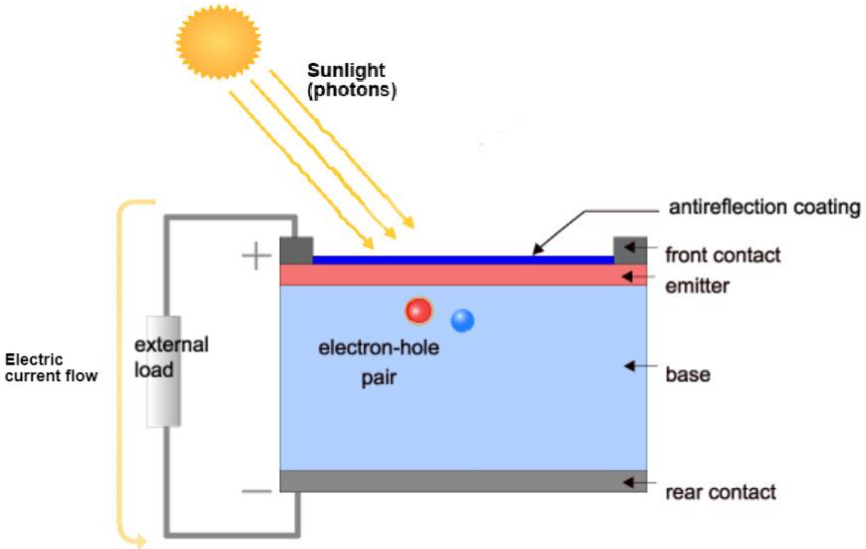

Figure 3.2 – Cross section of a solar cell connected to a load

The electrical current that is generated is DC, therefore, to connect the PV power station to the AC grid, an inverter is required in order to perform DC to AC conversion.

Solar cells are assembled in modules. The capacity of a PV module is a few hundreds of Watts (200 – 300 W). To obtain more power, PV modules are assembled in PV arrays. A PV park is composed of large numbers of PV arrays with an installed capacity that can reach tens of MW [57].

Figure 3.3 – *Ourika* PV park (46 MW capacity), Ourique, Portugal [58]

3.1.1. The PIN junction solar cell

Consider a PIN junction that is shown in *Figure 3.3*. The PIN structure consists of a p region and a n region separated by an intrinsic layer. The p region and the n region have different electrons concentration: the n-type has an excess of electrons while the p-type has an excess of holes, that are positive charges. The intrinsic layer width *W* is much larger than the space charge width of a normal PN junction.

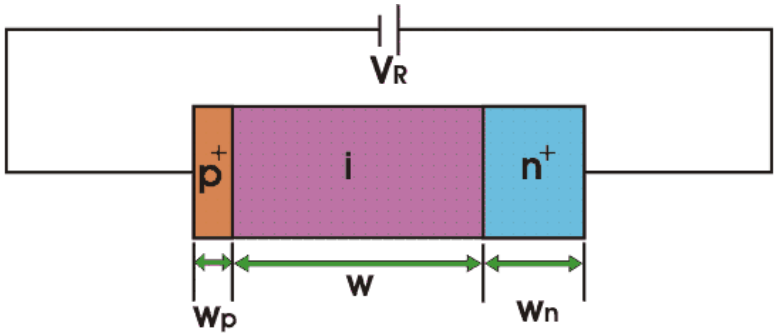

Figure 3.4 – Circuit of a PIN junction, where *W* is the intrinsic layer width

Absorption of light occurs in the intrinsic zone. A voltage V_R is applied so that there is an electric field in the intrinsic zone large enough so when the photons are absorbed, an electron-hole pair is created, i.e., a negative charge, electron, goes to the conduction band of the semiconductor and in the valence band a positive charge is going to move on the action of the electric field. Therefore, there is an electric field that immediately separates the positive from the negative charge (the negative goes to one of the terminals and the positive one goes to the other).

3.1.2. Photodetector vs. solar cell

Photodetectors are sensors of light, i.e., they detect the presence of photons. Like in a solar cell, a photo detector has a PIN junction that converts light photons into current.

Examples of photodetectors are photodiodes and phototransistors. A similar but different optical device is the LED, which is basically the inverse of a photodiode, instead of converting light to a voltage or current, it converts a voltage or current to light [56].

For photodetector applications, the speed of response is important, therefore these devices must have extremely fast response, exhibit high reliability and have a low cost.

In the photodetector, the photosensitivity is changed by speed. In practice, there is a current corresponding to an incident light intensity. If less electron-hole pairs are absorbed, a lower current will be present for the same luminous intensity (fewer electron-hole pairs were generated but at the same time a higher variation frequency can be applied to the signal that is applied to the input of the photodetector). The photodetector has a faster response because the device is shorter, so the response is faster to a higher frequency signal.

In a solar cell, on the other hand, there is no interest in applying a high frequency signal. In real conditions, the ambient light has a slow variation throughout the day. The main interest is that all the photons that enter the cell are converted into electric current. The length of the intrinsic zone for the solar cell must be bigger, in order to convert practically all photons into electron-hole pairs.

3.1.3. Electrical parameters of a solar cell

The output of the PV cell is often represented with the relation between the current and voltage. This is known as the **current-voltage curve** (I-V curve).

The I-V curve, which is represented in *Figure 3.4*, is a snapshot of all the potential combinations of current and voltage possible from a cell under standard test conditions (STC). A Datasheet of a PV module normally provides the module's specifications only at STC.

The parameters referenced by the upper index r are measured under STC [59].

- Cell temperature: $\theta^r = 25ºC \equiv T^r = 298.16\ K$
- Incident irradiance on the cell: $G^r = 1000\ W/m^2$
- Spectral distribution of solar radiation[6]: AM 1.5

[6] Spectral distribution of total solar radiation incident in a sunny day, on a surface perpendicular to the sun's rays and inclined 37º relatively to the horizontal, corresponding to an irradiance of 1000 W/m^2. AM stands for Air Mass.

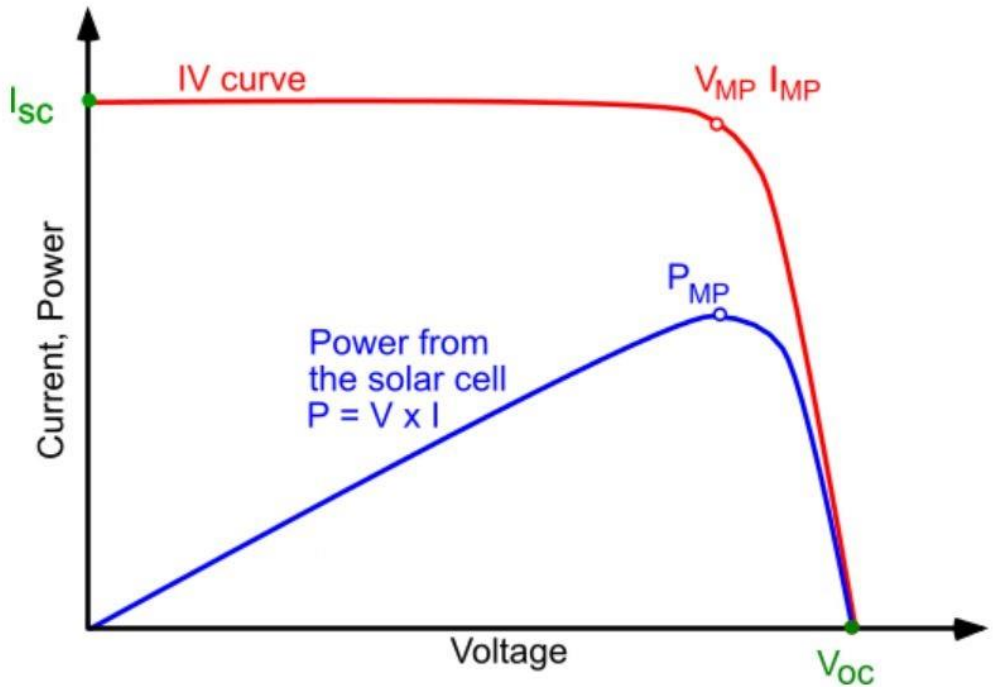

Figure 3.5 – I-V curve (red) and P-V curve (blue) of a solar cell: the power curve has a maximum denoted as P_{MP}, that occurs at a voltage of V_{MP} and a current of I_{MP} [60].

Several important parameters which are used to characterize solar cells are described below:

- **Short circuit current (I_{SC}):** the maximum current produced by the cell under STC conditions. It is the current when the load is short-circuited, i.e. the output voltage is zero. The output power at this point is essentially zero.

- **Open Circuit Voltage (V_{OC}):** the maximum voltage generated by the cell under STC conditions. It is the voltage when the load is open-circuited, i.e. the output current is zero. The output power at this point is again essentially zero.

- **Maximum Power (P_{MP}):** the maximum power that can be delivered from the cell under STC conditions. The point at I-V curve at which the maximum power is attainable is called Maximum Power Point (MPP).

$$P_{MP}^{r} = V_{MP}^{r} \cdot I_{MP}^{r} \qquad (3.1)$$

where V_{MP}^{r} and I_{MP}^{r} are the rated voltage and current, respectively, at STC conditions, that result in maximum power.

- **Fill Factor (FF)**[7]**:** a figure of merit that indicates the "squareness" of the I-V curve. It is the ratio of the actual maximum power P_{MP} to the unattainable but ideal power that would result from operating at I_{SC} and V_{OC}.

$$FF = \frac{P_{MP}^{r}}{V_{OC}^{r} \cdot I_{SC}^{r}} \qquad (3.2)$$

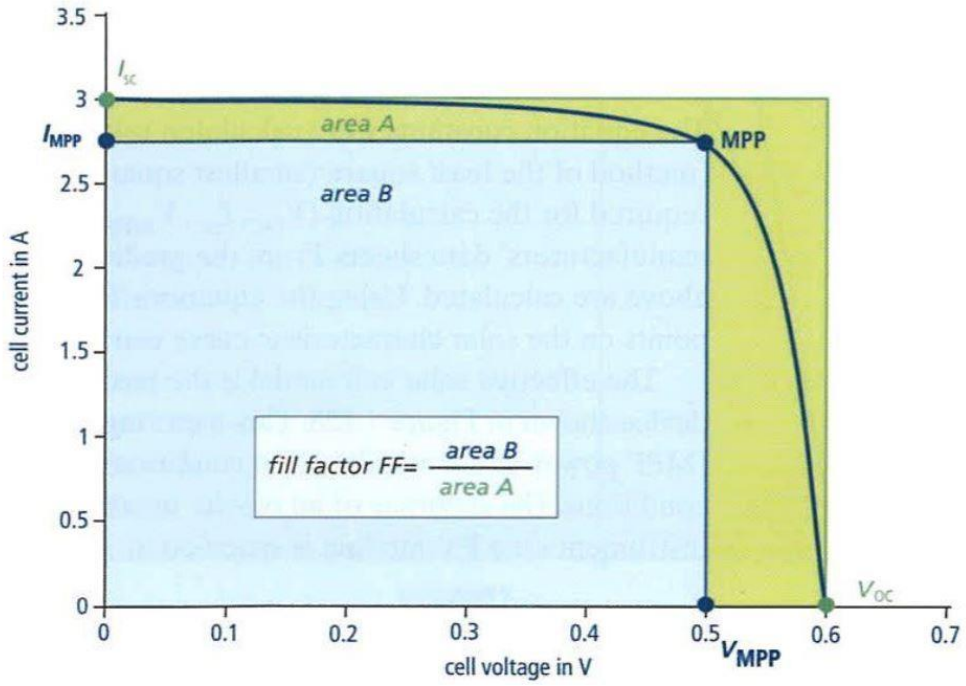

Figure 3.6 – Fill Factor: ratio of the largest rectangle that fits in the I-V curve (blue) over the largest possible rectangle (green)

For PV cells of the same material, the values of V_{OC}^{r} and I_{SC}^{r} are approximately constant, but the shape of the I-V curve may vary considerably.

- **Solar Cell Efficiency (*η*):** the ratio of energy output from the solar cell to input energy from the sun. It is the most common parameter to compare the performance of one solar cell to another.

$$\eta^{r} = \frac{P_{MP}^{r}}{A \cdot G^{r}} \qquad (3.3)$$

In *equation 3.3*, A is the cell area and G^{r} is the incident irradiance on the cell under STC. Naturally, for other operating conditions, the upper index r would not be used.

[7] Usually silicon cells have a Fill Factor between 0.7 and 0.85 (an ideal cell would have $FF = 1$).

- **Electrical power (P) for other operating conditions:**

$$P = V \cdot I = V \cdot \left\{ I_{CC} - \left[I_0 \cdot \left(e^{\frac{V}{m \cdot V_T}} - 1 \right) \right] \right\} \quad (3.4)$$

The maximum power in non-STC is obtained by:

$$\frac{dP}{dV} = 0 \Leftrightarrow I_{CC} + I_0 \cdot \left(1 - e^{\frac{V}{m \cdot V_T}} - \frac{V}{m \cdot V_T} \cdot e^{\frac{V}{m \cdot V_T}} \right) = 0 \Leftrightarrow$$

$$\Leftrightarrow e^{\frac{V}{m \cdot V_T}} = \frac{\frac{I_{CC}}{I_0} + 1}{\frac{V}{m \cdot V_T} + 1} \quad (3.5)$$

The solutions of *equation 3.5*, are the maximum power voltage and current, respectively, given by:

$$V_{MP} = m \cdot V_T \cdot \left(\frac{\frac{I_{CC}}{I_0} + 1}{\frac{V_{MP}}{m \cdot V_T} + 1} \right) \quad (3.6)$$

$$I_{MP} = I_{CC} - I_0 \cdot \left(e^{\frac{V_{MP}}{m \cdot V_T}} - 1 \right) \quad (3.7)$$

3.1.4. Analytic model of a solar cell

The representation of equipment through equivalent electrical circuits is a technique used in the field of electrical engineering. In order to better study the PV equipment, this methodology is also used with two simplified mathematical models that will be presented in this subchapter.

The basic solar cell structure is simply a PIN junction diode. From a circuit perspective, it is apparent that a solar cell can be modeled by an ideal current source, I_s. This current source represents the electric current generated by the light beam upon reaching the active surface of the solar cell. The PIN junction acts as a diode that is traversed by a unidirectional internal current, I_d, which depends on the voltage V at the cell terminals [61].

The current–voltage (I–V) characteristic of a typical silicon solar cell is plotted in *Figure 3.6*. At small applied voltages, the diode current is negligible and the current is just the short-circuit current, I_{SC}. When the sun illuminates the PV cell, its power source produces a photoelectric current, I_{ph}. The level of this current depends on the irradiance, G. The characteristic curve of a solar cell is represented in red in *Figure 3.7*.

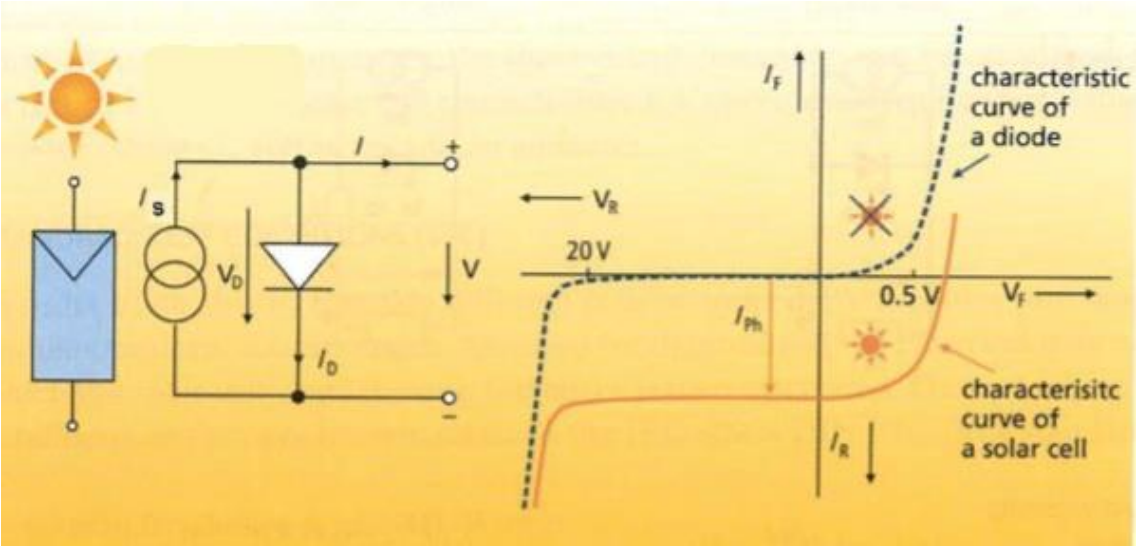

Figure 3.7 – Equivalent circuit and characteristic curve (I-V) of a solar cell [62]

The I-V characteristic has two curves in *Figure 3.6*: in black, the characteristic in dark, without light when no photons are entering the device; in red, the characteristic when the cell is under illumination.

A solar cell in the dark is a large flat diode. A simple dark I-V measurement produces the exponential curve, characteristic of a diode. Since solar cells convert light to electricity it might seem odd to measure the photovoltaic cells in the dark. However, dark I-V measurements are vital in examining the diode properties. Under illumination, small fluctuations in the light intensity add considerable amounts of noise to the system. Thus, dark I-V measurements give extra information about the PV cell for diagnostic purposes [63].

a) Single Diode and 3 parameters model

In this model, a silicon solar cell can be described through the equivalent electric circuit in *Figure 3.8*:

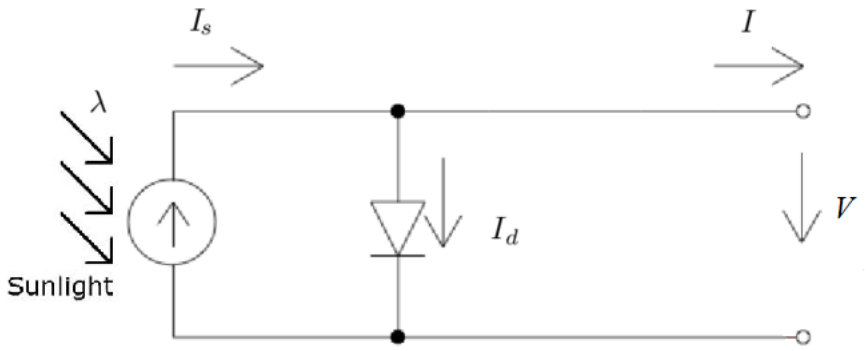

Figure 3.8 – Equivalent circuit of a PV cell (1 diode and 3 parameters model)

The three parameters in this model are I_s, I_0 and m.

The current source I_s represents the electric current generated by the beam of light radiation, consisting of photons, upon reaching the active surface of the cell. The level of this current depends on the irradiance.

The short-circuit current of the PV cell at STC is equal to the current source I_s.

$$I_{SC}^r = I_S^r \tag{3.8}$$

As it depends on the irradiance, outside of STC the short-circuit current is given by:

$$I_{SC} = \frac{G}{G^r} I_{SC}^r \tag{3.9}$$

The PIN junction functions as a diode that is traversed by an internal unidirectional current I_d, which depends on the voltage *V* at the terminals of the cell, that is

$$I_d = I_0 \cdot \left(e^{\frac{V}{m \cdot V_T}} - 1 \right), \tag{3.10}$$

where I_0 is the reverse saturation current of the diode, m is the diode factor and V_T is the thermal voltage for a given temperature T, given by:

$$V_T = \frac{k \cdot T}{q}. \tag{3.11}$$

k is the Boltzmann constant and q is the charge of electron.

And so, the total current *I* is

$$I = I_s - I_d = I_s - I_0 \cdot \left(e^{\frac{V}{m \cdot V_T}} - 1 \right). \tag{3.12}$$

This model was primarily developed for a single cell. Its generalization to the whole module implies that all cells are considered as rigorously identical.

b) Single Diode and 5 parameters model

The simplified model of 1 diode and 3 parameters is not a strict representation of the PV cell. It is necessary to take into account the voltage drop in the circuit up to the external contacts, which can be represented by a series resistance R_s, and also the leakage currents, which can be represented by a parallel resistance, R_p. The influence of these parameters on the I-V characteristic of the solar cell can be studied using the equivalent circuit presented on *Figure 3.9*:

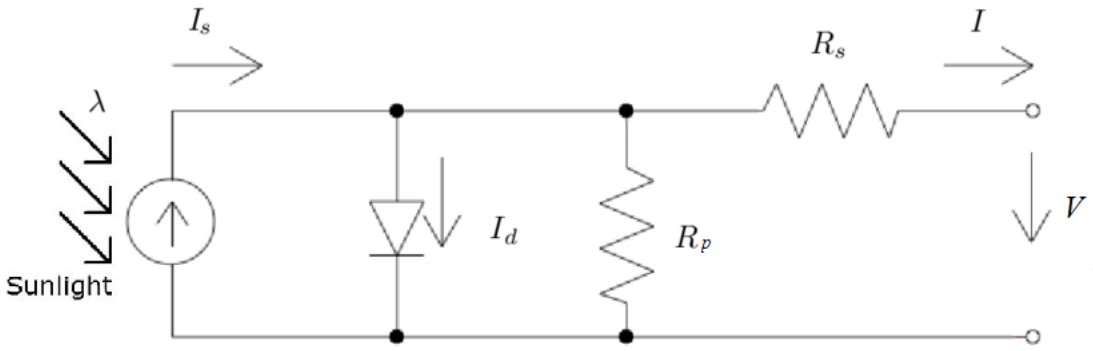

Figure 3.9 – Equivalent circuit of a PV cell (1 diode and 5 parameters model)

The model parameters are I_s, I_0, m, R_s e R_p and they are related with the current I:

$$I = I_s - I_d - I_p \Leftrightarrow$$

$$\Leftrightarrow I = I_s - I_0 \cdot \left(e^{\frac{V}{m \cdot V_T}} - 1\right) - \frac{V + R_s \cdot I}{R_p} \qquad (3.13)$$

These two models allow the calculation of the output power value, based on the incident irradiance, temperature and on data provided by the manufacturers in the datasheet of the equipment, thus avoiding the need for testing the solar cell.

4. Simulation

4.1. COMSOL Multiphysics® software

The main software used for this dissertation was COMSOL Multiphysics®. It is generally used for modelling and simulation of real world multiphysics systems.

The COMSOL Multiphysics® software enables the simulation of designs and devices based on electromagnetics, structural mechanics, acoustics, fluid flow, heat transfer, and chemical engineering behaviour. The software performs the simulation of any physics-based system that can be described with partial differential equations, using finite element analysis.

The users of this software are usually researchers and engineers working for leading technical enterprises, research labs, and universities.

In this dissertation, the main areas of interest with this software are:

- an analysis of a semiconductor device operation at the fundamental physics level;
- the simulation of electric, magnetic, and electromagnetic fields;
- to design antennas, waveguides, filters or circuits.

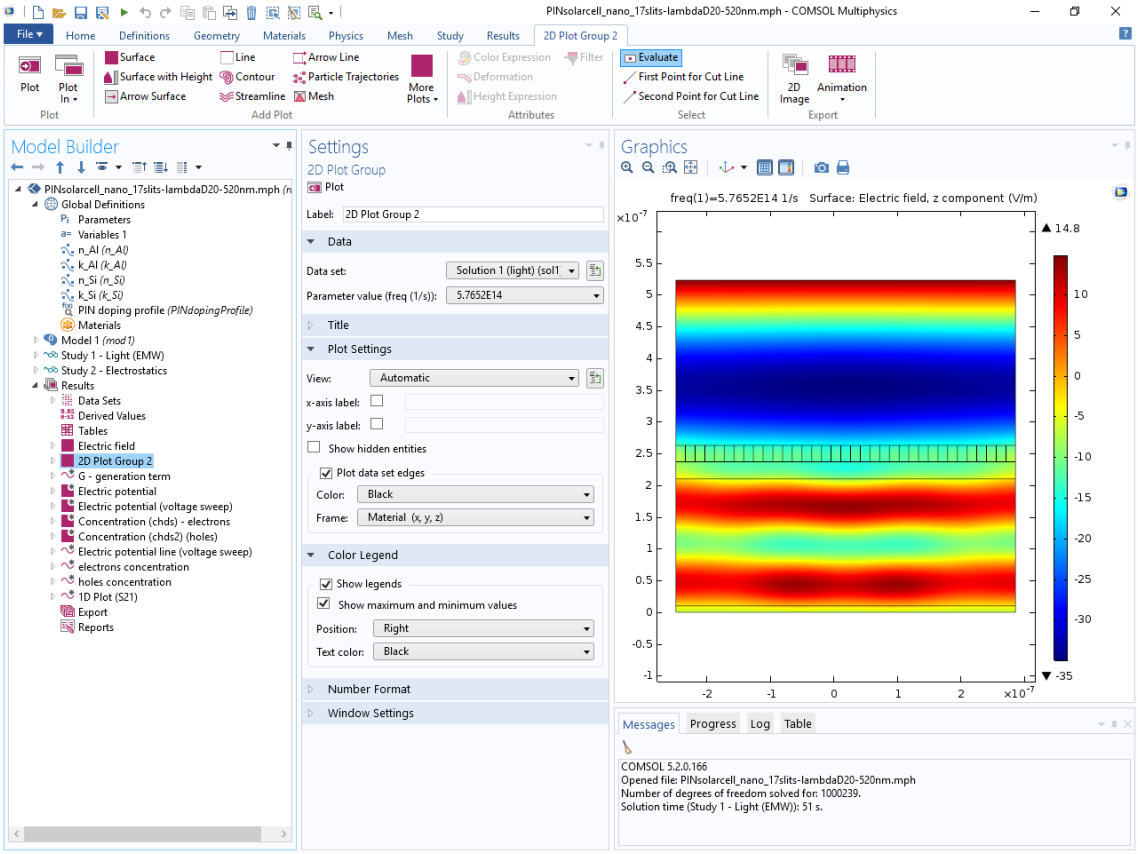

Figure 4.1 – A screenshot of COMSOL Multiphysics® GUI[8]

[8] GUI, graphical user interface, is a form of user interface that allows users to interact with electronic devices through graphical icons and visual indicators.

4.2. Modelling Optical Nanoantenna Arrays with COMSOL Multiphysics®

Firstly, we begin to module a PIN junction (solar cell) using COMSOL Multiphysics® with the following parameters in *Table 4.1*.

The purpose of the simulation is to study the propagation of light inside the semiconductor device.

Table 4.1 – Parameters of the PIN junction in COMSOL Multiphysics® software

Parameter	Value
Silicon electron mobility	0.15 [m^2/V*s]
Silicon hole mobility	0.045 [m^2/V*s]
Electron affinity	4.05 [V]
Silicon band gap @ 300 K	1.75 [V]
Intrinsic carrier concentration	1.5e10 [1/cm^3]
Relative permittivity	11.7
Electron carrier lifetime	1e-7 [s]
Hole carrier lifetime	1e-7 [s]
Substrate doping (p-doping)	1e17 [1/cm^3]
Peak concentration of implanted profile (n-doping)	1e17 [1/cm^3]
Lattice temperature	300 [K]
Elementary charge	1.6022e-19 [C]
Boltzmann constant	1.3806e-23 [J/K]
Thermal voltage	0.02585 [V]
Drain voltage	0 [V]
Junction width (2D)	1e-7 [m]
Junction depth (3D)	640 [nm]
Active Area = Junction width * Junction Depth	1e-9 [m^2]
p-doping layer	1e-8 [m]
n-doping layer	2.7e-8 [m]
Intrinsic region layer	2e-7 [m]
Total layer	2.37e-7 [m]
Total layer and Air	5e-7 [m]
Heaviside function	1e-8 [m]
Wavelength	5.3e-7 [m]
Layer Air Top	2.65e-7 [m]
Layer Air Bottom	2e-7 [m]
Plank constant	6.6261e-34 [J*s]
Current Density constant	1 [A/mol]
Spatial density converter factor	1 [1/mol]
Input Power Flow	1000 [w/m^2]
Standard light input power = Input Power Flow * Active area	1e-6 [W]
Number of voltage points	21
End voltage	0.42 [V]
Number Curves Display	5
Frequency	c/λ = 5.6565e14 [Hz]
Height Thin Layer	1e-9 [m]
Multiplication Factor	1
Incidence Angle	0 [rad]

The incident light, an EM wave with a wavelength of 530 nm in the visible band, hits a silicon PIN junction with dimensions: 150 nm, length of the p-junction; 2 µm, length of the intrinsic layer; 80 nm, length of the n-junction. The width was set to 0.5 µm, while the PIN junction depth was set to 640 nm. These values are representative for a 0.35 µm CMOS process.

In *Figure 4.2*, there is a schematic representation of the silicon PIN junction on COMSOL Multiphysics®:

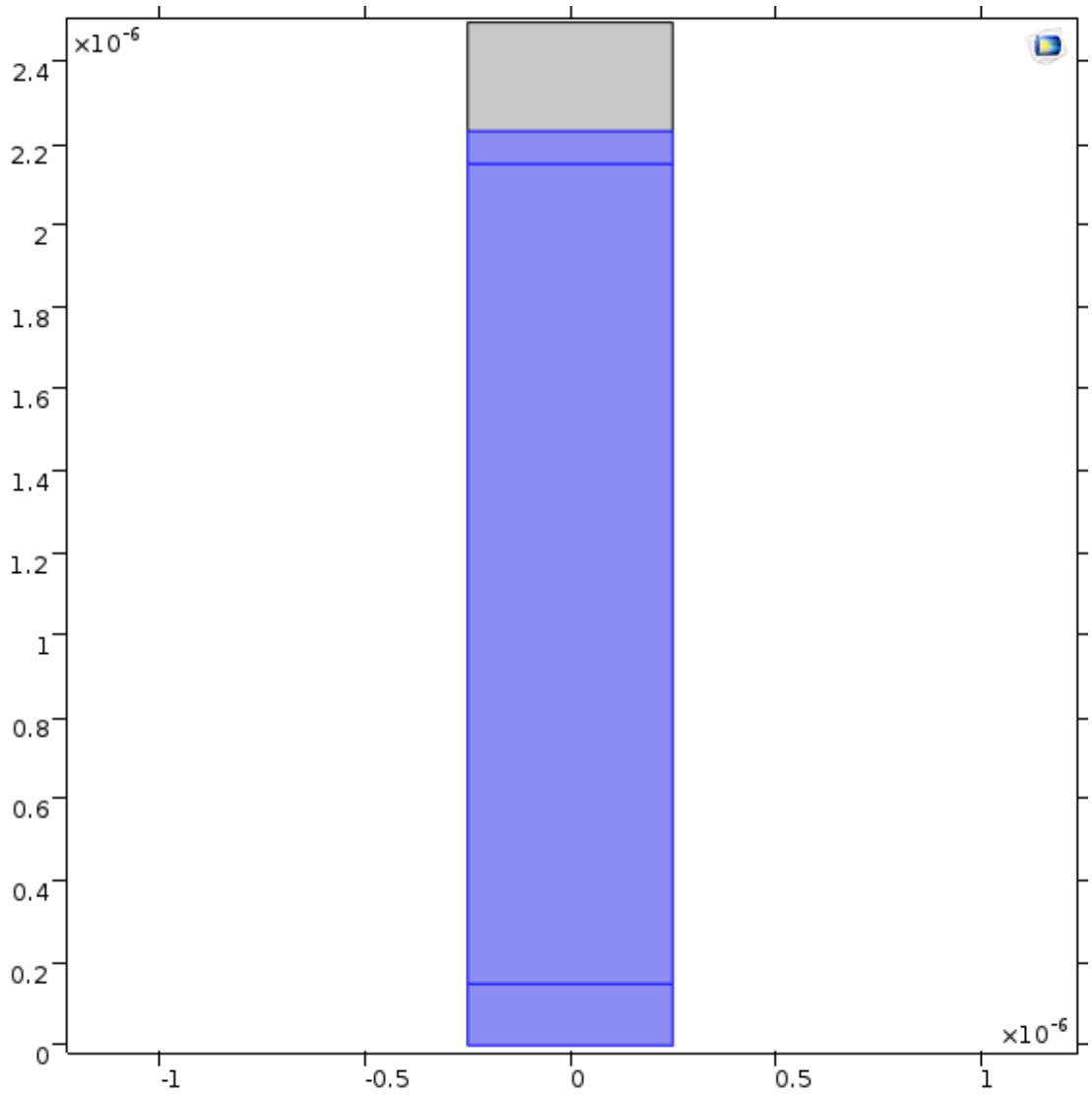

Figure 4.2 – Schematic representation of a PIN junction on COMSOL Multiphysics®

From the figure above, it can be said that the geometry consists of two parts. The first part is air (in *grey*), whose edge on top is used as the source for the EM wave that arrives to the solar cell. The second part, in *blue*, is the PIN junction (from top to bottom, n-junction, intrinsic zone and the p-junction).

The results are obtained through the simulations performed on COMSOL Multiphysics®, that uses the finite element method (FEM)[9]. This method is used to calculate the electric field, so that the program needs to define a mesh to solve the system of equations.

A customized mesh with triangular elements and a maximum element size of 10 nm was defined and it is represented in *Figure 4.3*. The basic condition is that the mesh size should be lower than wavelength, in order not to have numerical errors in the calculation of the solution.

The FEM gives an approximate solution to the mathematical model equations and so it is important to consider an error estimate.

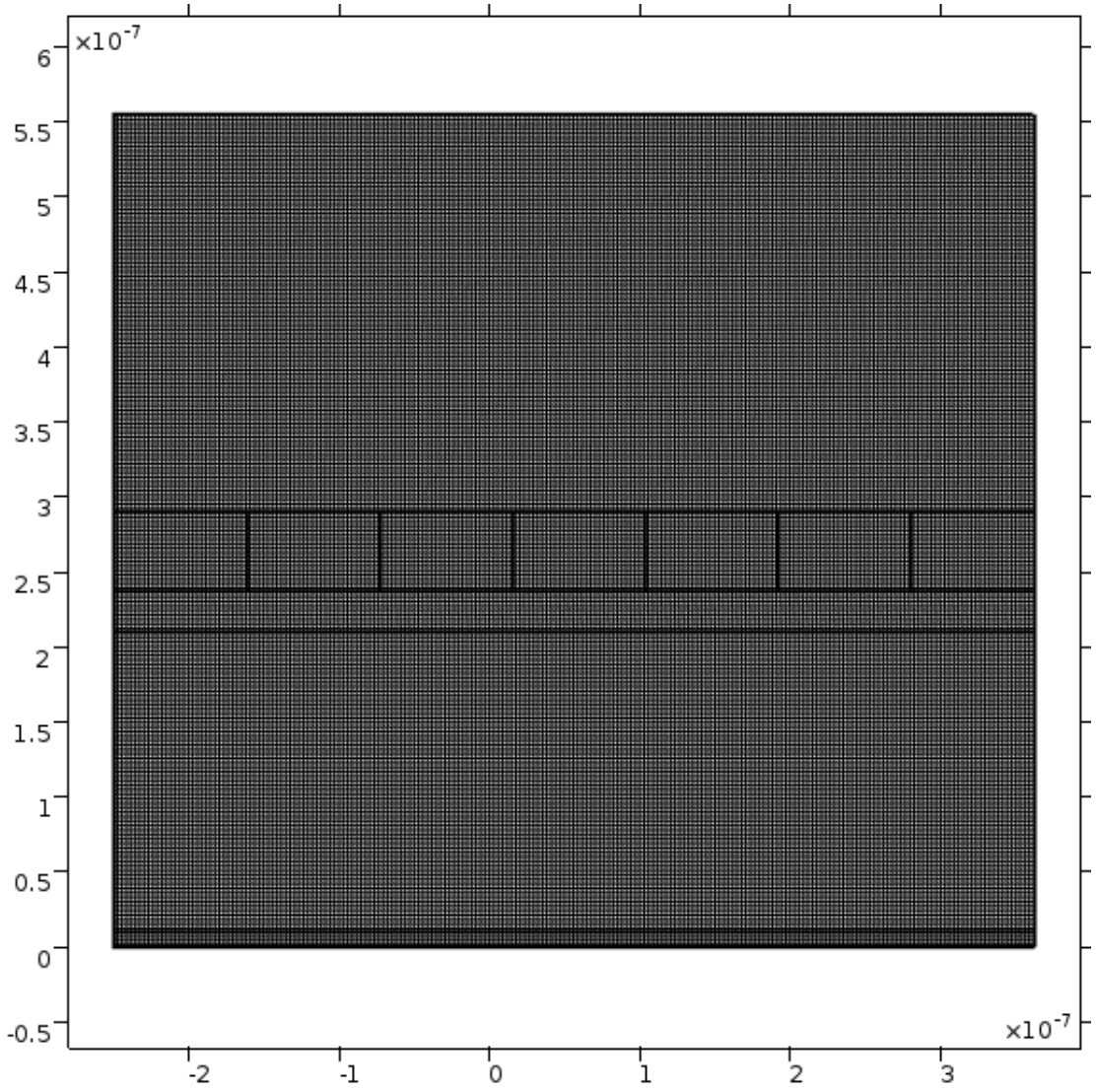

Figure 4.3 – Schematic representation of a mesh on a PIN junction on COMSOL Multiphysics®

[9] FEM is a numerical method for solving problems of engineering and mathematical physics. To solve the problem, it subdivides a large system into smaller, simpler parts called finite elements.

Meshes are defined by the following parameters [64]:

- Maximum element size: limits the size of the finite elements.
- Minimum element size: specifies the minimum size of the finite elements.
- Maximum element growth rate: the maximum rate at which an element can grow in a region with small elements to a region with large elements. This value has to be greater than 1.
- Curvature factor: determines the size of the boundary elements in comparison to the curvature of the geometric boundary (it is the ratio of element size to radius of curvature).
- Resolution of narrow regions: used to control the number of layers of elements that are created in narrow regions. A higher value results in a finer mesh in narrow regions.

The parameters used for the mesh on the different simulations are represented on *Table 4.2*:

Table 4.2 – Mesh parameters on COMSOL Multiphysics® software

Parameter	**Value**
Maximum element size	1e-8 [m]
Minimum element size	5e-11 [m]
Maximum element growth rate	1.1
Curvature factor	0.2
Resolution of narrow regions	1

The mesh settings determine the resolution of the finite element mesh used to discretize the model. The FEM divides the model into small elements of geometrically simple shapes. In each shape, a set of polynomial functions is used to approximate the structural displacement field — how much the object deforms in each of the three coordinate directions [64].

In this example, because the geometry contains small edges and faces, an extremely finer mesh was designed. This will better resolve the variations of the stress field and give a more accurate result. Refining the mesh size to improve computational accuracy always involves some sacrifice in speed and typically requires increased memory usage [64].

4.3. Simulation results

4.3.1. Silicon PIN junction

In this study, we concentrate on the TE polarization. TE (Transverse Electric) polarized light is characterized by its electric field being perpendicular to the plane of incidence. For TE light, the magnetic field lies in the plane of incidence, thus its always perpendicular to the electric field in isotropic materials. On the other hand, TM (Transverse Magnetic) polarized light is characterized by its magnetic field being perpendicular to the plane of incidence [65].

In this case, the electric field has only one component along the z-direction.

The results presented in this chapter were obtained under similar conditions to those of the previous chapter, i.e., with an identical PIN structure.

The PIN junction was tested for different values of **λ** (light wavelength): 400 nm (blue), 530 nm (green) and 800 nm (IR).

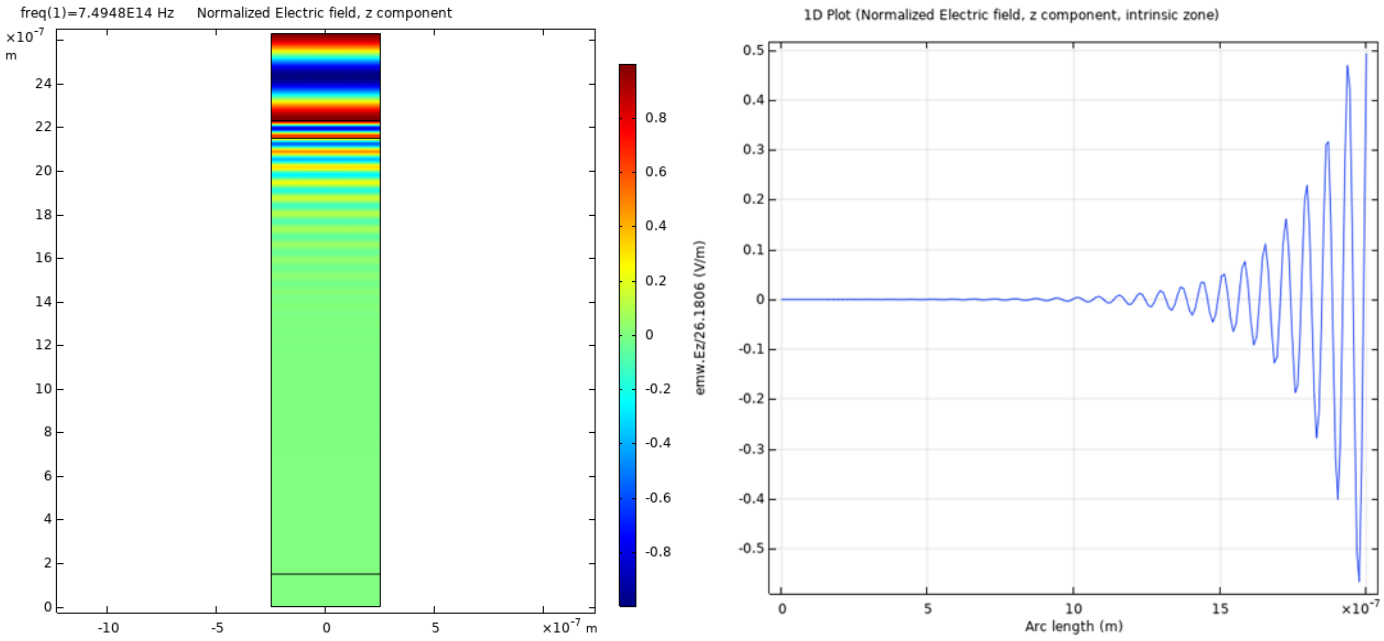

(a) **(b)**

Figure 4.4 – For a light wavelength of 400 nm
(a) Normalized Electric field, z-component of the cross section of a PIN junction
(b) 1D Plot of the Normalized Electric field, z component, intrinsic zone

For a light wavelength of 400 nm, in the blue region, the photons are absorbed mainly in the top of the intrinsic region. Electric field is zero in the bottom part of the intrinsic region.

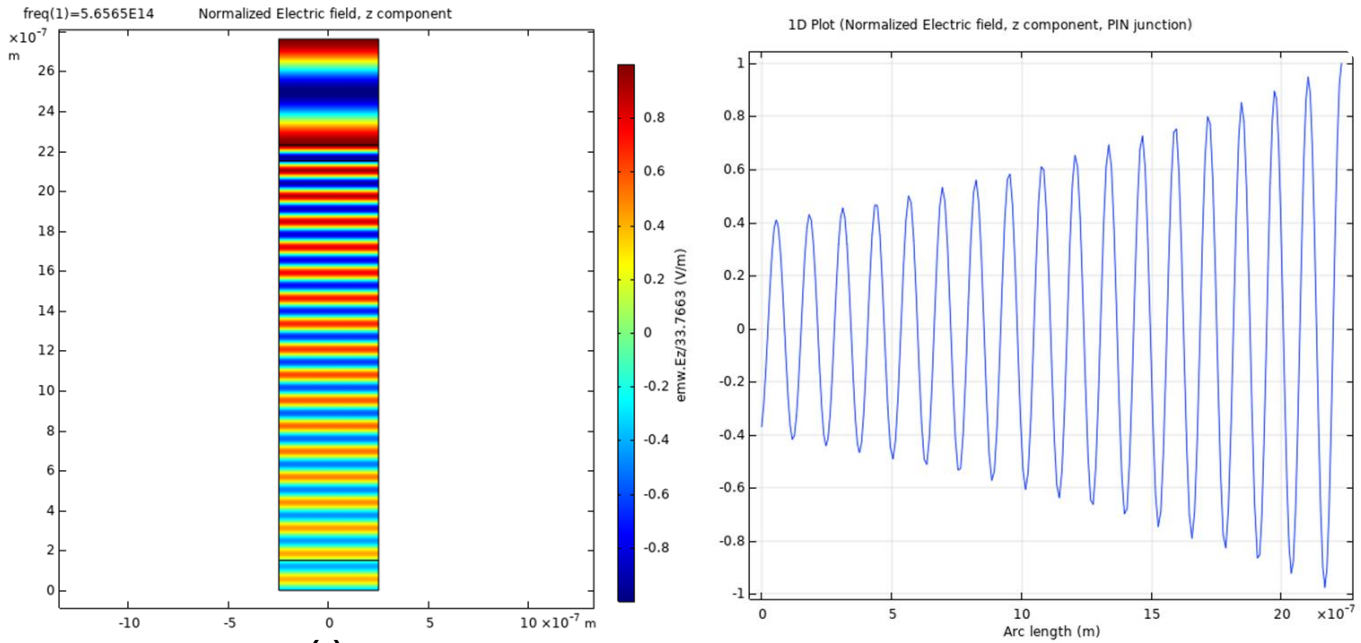

(a) **(b)**

Figure 4.5 – For a light wavelength of 530 nm
(a) Normalized Electric field, z-component of the cross section of a PIN junction
(b) 1D Plot of the Normalized Electric field, z component, intrinsic zone

It can be seen in Figure 4.5 that for a light wavelength of 530 nm, the electric field is stronger in the n-junction and decreases along the intrinsic zone, due to the fact that the photons are absorbed mainly in this area.

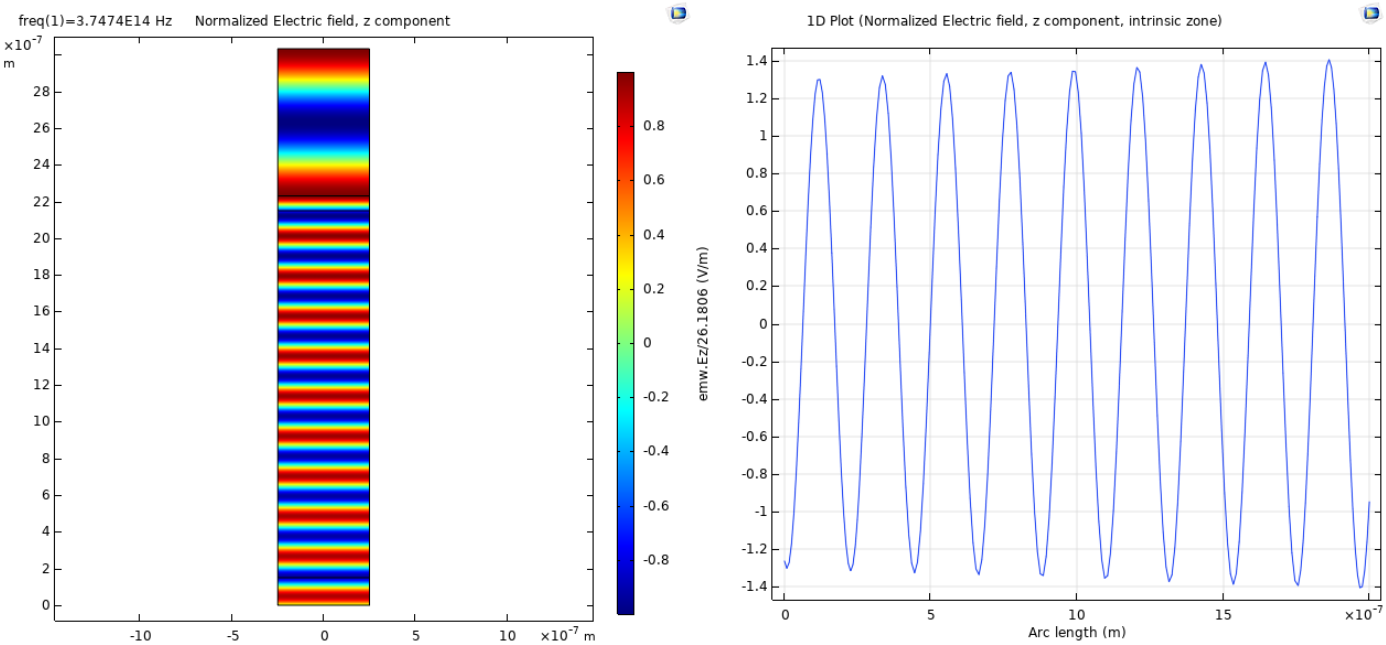

(a) **(b)**

Figure 4.6 – For a light wavelength of 800 nm
(a) Normalized Electric field, z-component of the cross section of a PIN junction
(b) 1D Plot of the Normalized Electric field, z component, intrinsic zone

For a light wavelength of 800 nm, we observe on Figure 4.6 (a) and (b) that the electric field practically does not decrease along the intrinsic zone. Thus, we could conclude that there is almost no absorption of photons for this wavelength.

With the aid of MATLAB, a 1D plot was made in order to compare the values of the normalized electric field along the intrinsic zone for the light wavelengths of 400, 530 and 800 nm:

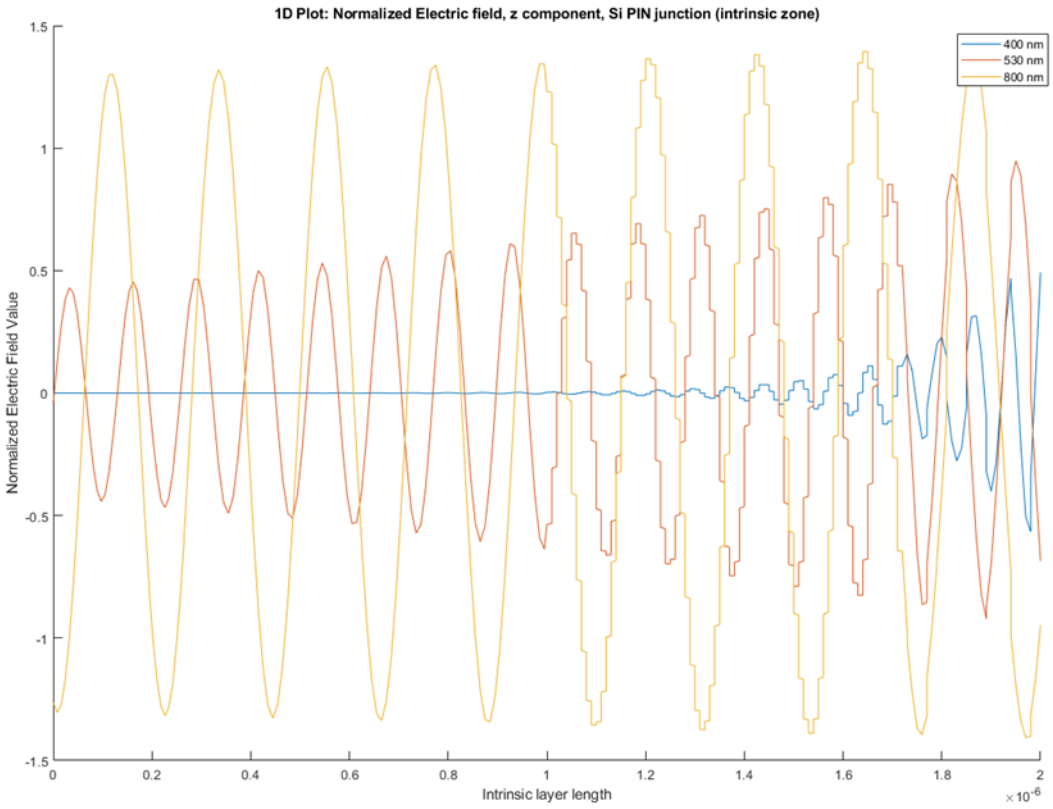

Figure 4.7 – 1D Plot of the normalized electric field, z-component, along the intrinsic zone

For 400 nm and 530 nm, the length of the intrinsic zone is appropriate for the absorption of photons. Meanwhile, for 800 nm, the length of the intrinsic zone should be bigger to better absorb the incoming light.

4.3.2. Introduction of nanoantennas

In this subchapter, we analyse the behaviour of the electric field when an aluminium nanoantenna with apertures (or air slits) is introduced on top of the silicon PIN junction. The operating principle of an optical antenna with apertures is identical to that of an array of nanoantennas.

The main purpose of these simulations is to observe the difference between a PIN junction without nanoantenna and with a nanoantenna. Furthermore, it is our interest to analyse the evolution of the diffraction pattern as the number of air slits increases, namely a three-slit, a seven-slit and a fifteen-slit array and to compare the simulation results with the results expected by the classical theory [71].

The simulation environment used is similar to that of Figure 4.2, where an incident light wave hits the PIN junction by propagating through the air slit arrays and absorbed along the intrinsic region.

Before introducing the various experiments that were done using the COMSOL Multiphysics® software, is important to recall an important material property, that is the index of refraction. The description of the complex index of refraction of all materials used in the simulations is in Appendix A.

Various experiments were performed, where the electric field was normalized to $E(0)$, that is the incident electric field.

The incident light wave has an electric field, whose amplitude is registered. This amplitude is constant for all cases that we are about to simulate and thus it will serve for normalization. It is necessary to have a normalization constant in order to better compare the electric field values for the cases when there is a nanoantenna on top of the PIN junction and when there is no nanoantenna (the structure will be different).

When light hits the surface, the electric field is no longer the incident field. It is the incident field plus the reflected field, and the reflected field varies whether or not there is a nanoantenna.

In these experiments, it was considered that the dimensions of the air slits and their spacing had subwavelength dimensions as well as the metal thickness. And so, for four different values of the light wavelength, four particular cases were considered:

- a nanoantenna metal thickness of λ/10 and an air slit width of λ/10;
- a nanoantenna metal thickness of λ/100 and an air slit width of λ/2;
- a nanoantenna metal thickness of λ/100 and an air slit width of λ/5;
- a nanoantenna metal thickness of λ/100 and an air slit width of λ/10.

For each case, on top of the PIN junction a three-slit, a seven-slit and a fifteen-slit array nanoantennas were tested. The procedures required to study and simulate a fifteen-slit array are identical to those used to simulate a three-slit or a seven-slit array, as the parameters are the same, differing only in the number of slits.

The maximum absolute values of the normalized electric field along the intrinsic region were registered on the Table 4.3:

Table 4.3 – Maximum absolute values of the normalized electric field along the intrinsic region

Light wavelength	Metal thickness	Air slit width	Array of 3 slits	Array of 7 slits	Array of 15 slits
400 nm	λ/10	λ/10	0.087	0.059	0.86
	λ/100	λ/5	0.536	0.369	0.577
		λ/10	0.335	0.356	0.517
530 nm	λ/10	λ/10	0.19	0.181	0.122
	λ/100	λ/5	**1.019**	**1.018**	**1.040**
		λ/10	0.956	0.893	0.908
800 nm	λ/10	λ/10	0.188	0.098	0.140
	λ/100	λ/2	**1.787**	**2.575**	**2.633**
		λ/5	**1.704**	**2.547**	**1.612**
		λ/10	**1.605**	**1.01**	**1.027**
1550 nm	λ/10	λ/10	0.177	0.063	0.272
	λ/100	λ/2	**10.053**	**8.071**	**5.806**
		λ/5	**11.467**	**4.508**	**4.724**
		λ/10	**2.3035**	**1.3689**	**1.0826**

When the total electric field is normalized by the incident field, it is possible to immediately check whether the radiation through the intrinsic region is higher or lower than the incident radiation. In other words, if any numerical value obtained by the different simulations is greater than 1, it means that the structure itself has the capacity to transmit more light than its incidence, which indicates the occurrence of the Extraordinary Optical Transmission phenomenon. The results highlighted in green indicate the occurrence of the EOT phenomenon.

The metal thickness λ/100 proved to be more efficient and thus more simulations were performed with this size. This metal thickness was the most efficient as it can be in part attributed to the fact that aluminum, for very small film thicknesses, has a very large transmission coefficient and a low reflection coefficient. Meanwhile, for a metal thickness of λ/10 there was no occurrence of the EOT phenomenon. Contrary to what happens in the previous case, in this case practically everything is reflected and little transmitted.

The results obtained from the simulations indicate that:

- if the nanoantenna metal thickness is much smaller in relation to the wavelength, the stronger will be the electric field intensity in the intrinsic region.
- the smaller the air slit size in relation to the wavelength, the smaller the intensity of the electric field in the intrinsic region, as expected given the classical theories of diffraction.

These results are confirmed by the classical theory as Extraordinary Optical Transmission is observed mainly due to the constructive interference of SPPs propagating between the slits of the nanoantenna, where they can be coupled from/into radiation.

The shape, dimensions and the spacing between apertures are fundamental parameters that must be carefully dimensioned to allow the propagation of SPP and the occurrence of the EOT phenomenon.

Below three cases are represented for a light wavelength of 400 nm: the metal thickness was set to λ/100 and each metal part width was set to λ/5 and they are separated by λ/5 as well.

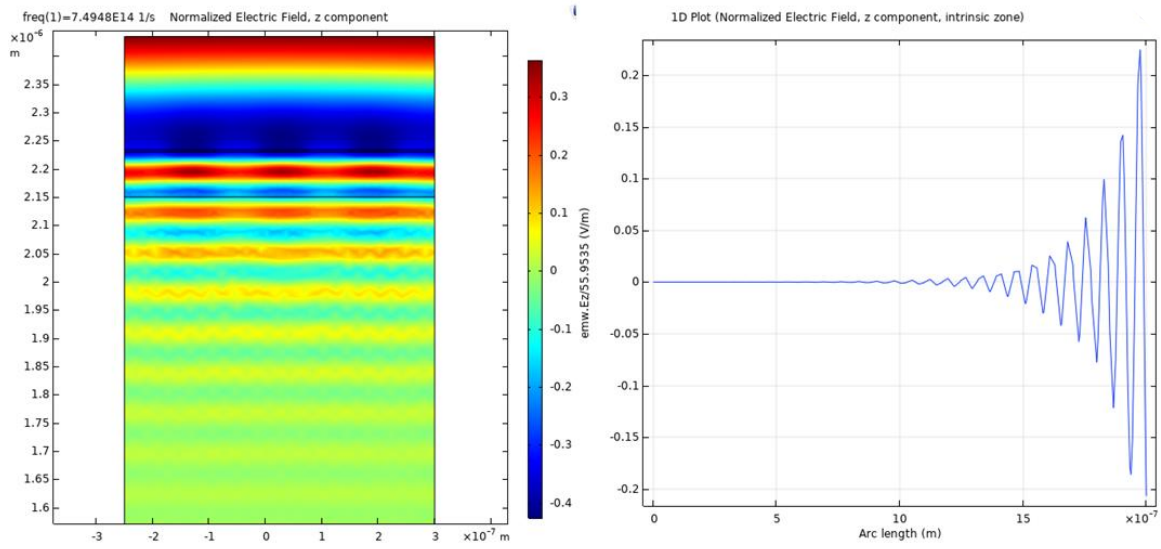

(a) **(b)**

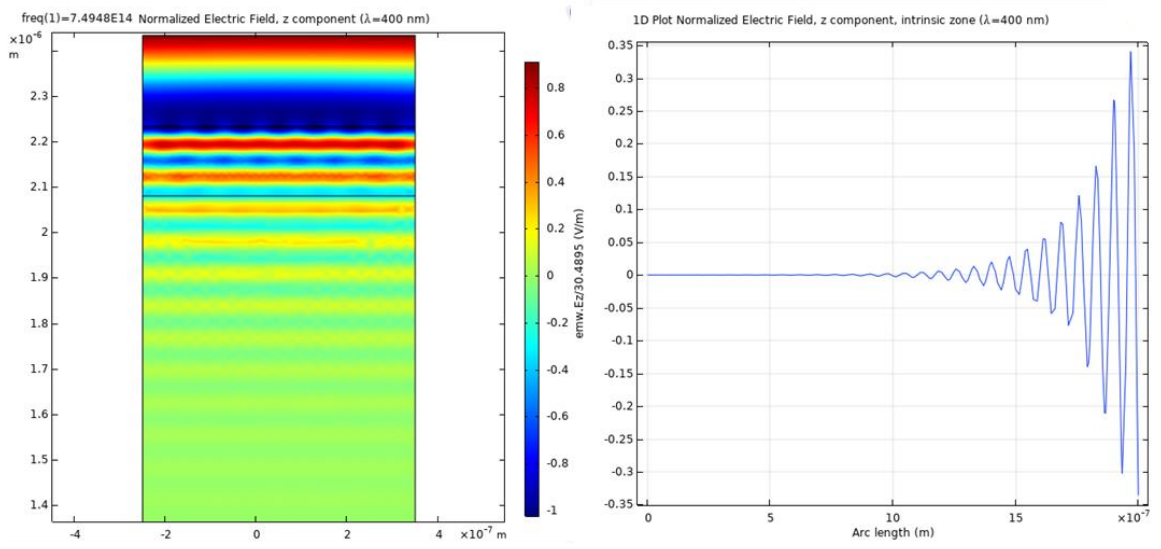

(c) **(d)**

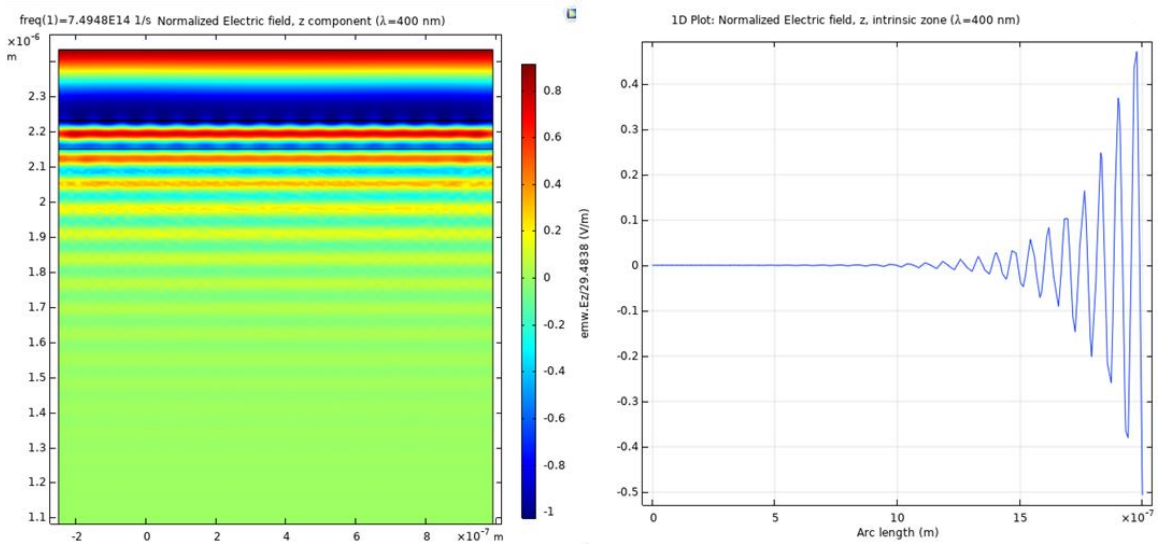

Figure 4.8 – For a light wavelength of 400 nm:
Normalized Electric field, z-component: **(a)** 3 slits; **(c)** 7 slits; **(e)** 15 slits
1D Plot of the Normalized Electric field z-component along the intrinsic zone:**(b)** 3 slits;**(d)** 7 slits;**(f)** 15 slits

With the aid of MATLAB, a 1D plot was made to compare the values of the normalized electric field along the intrinsic zone for the light wavelength of 400 nm with and without nanoantennas:

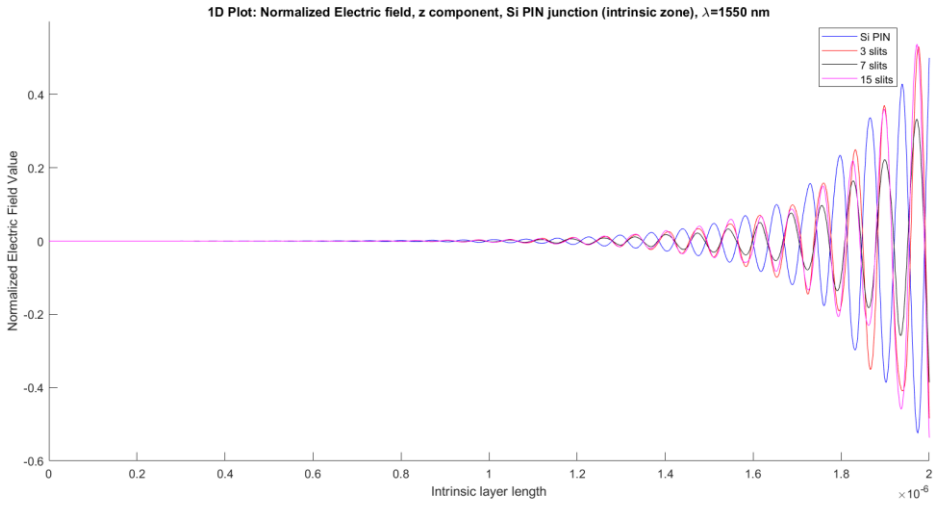

Figure 4.9 – 1D Plot of the normalized electric field, z-component, along the intrinsic zone (for a light wavelength of 400 nm)

We observe in all cases that the electric field is stronger in the n-junction and then rapidly reaches the zero value in the middle of the intrinsic zone.

By analysing *Figure 4.9*, we observe that the normalized electric field is stronger without nanoantennas. For this light wavelength, the results for other parameters of metal thickness and air slit width in *Table 4.3* are quite identical and thus, we conclude that for a light wavelength of 400 nm the introduction of nanoantennas for solar harvesting does not contribute for a bigger efficiency of the solar cell.

For a light wavelength of 530 nm, we have seen in *Table 4.3* that for a metal thickness of λ/100 and an air slit width of λ/5 barely occurs the EOT phenomenon.

In *Figure 4.10*, we compare the three cases where this phenomenon occurs:

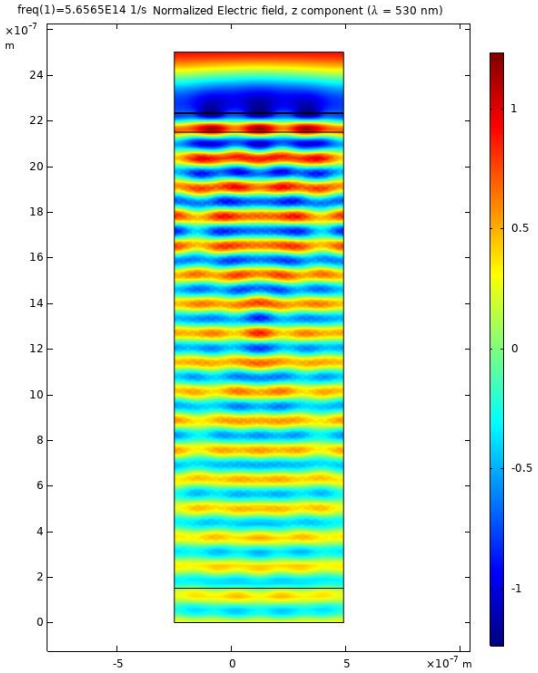

(a)

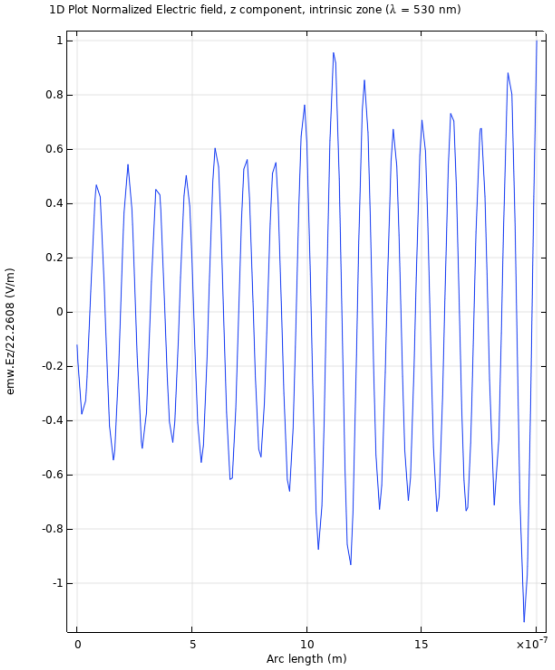

(b)

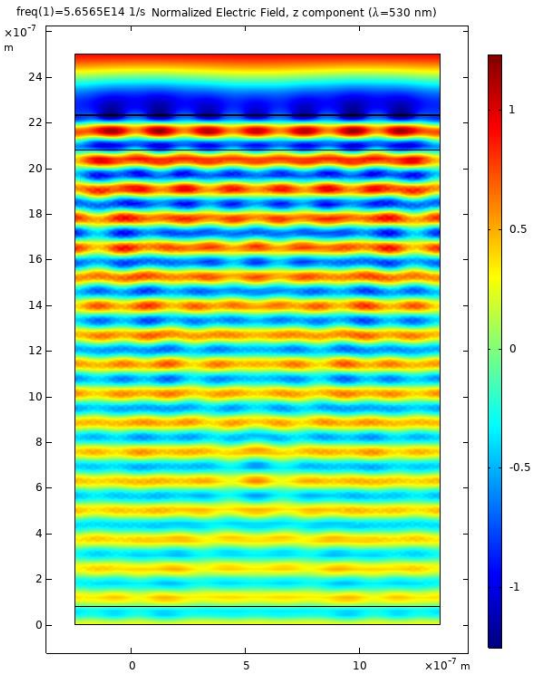

(c)

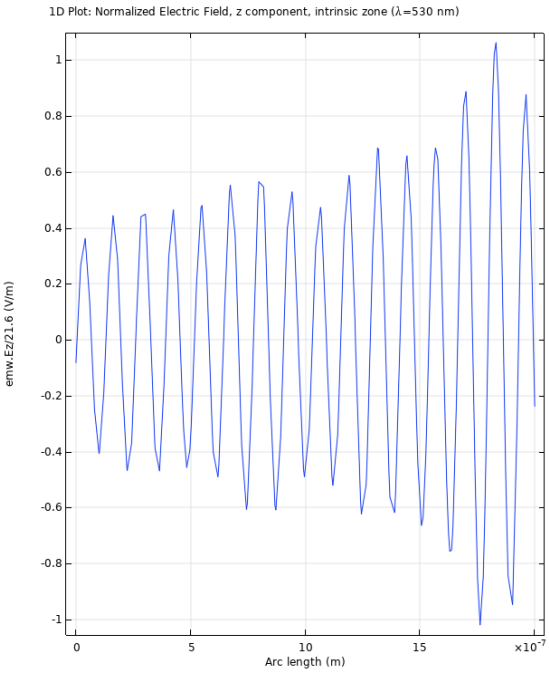

(d)

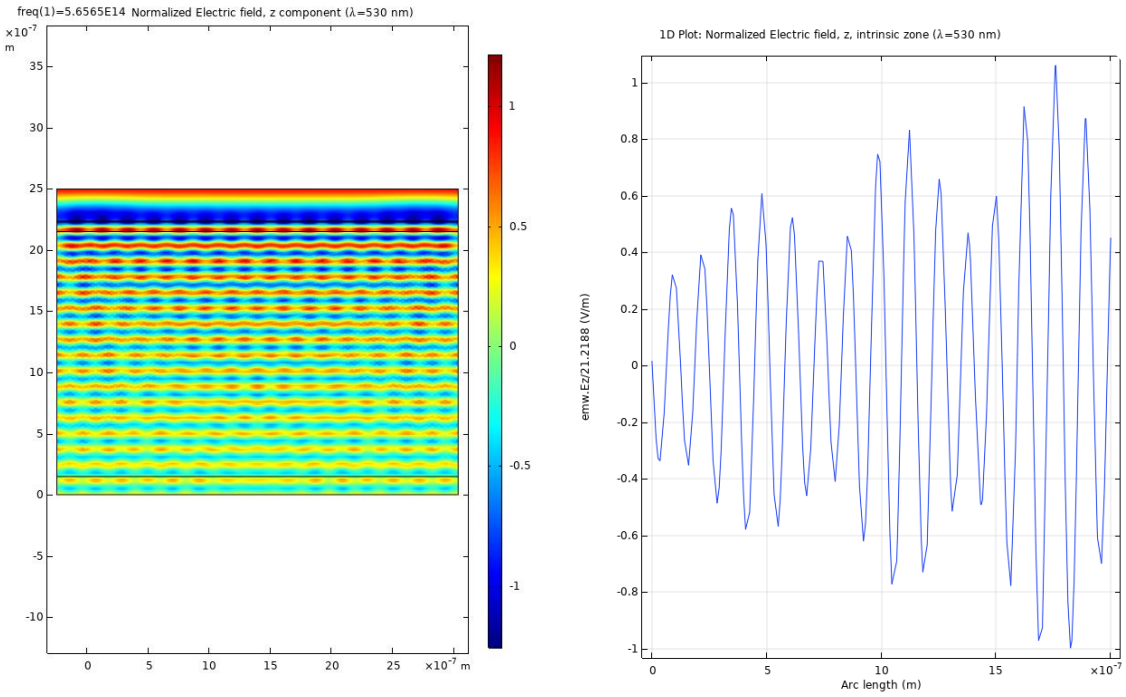

(e) **(f)**

Figure 4.10 – For a light wavelength of 530 nm:
Normalized Electric field, z-component (zoomed section of a PIN junction):
(a) 3 slits; **(c)** 7 slits; **(e)** 15 slits

1D Plot of the Normalized Electric field, z-component along the intrinsic zone
(b) 3 slits; **(d)** 7 slits; **(f)** 15 slits

With the aid of MATLAB, a 1D plot was made to compare the values of the normalized electric field along the intrinsic zone for the light wavelength of 530 nm with and without nanoantennas:

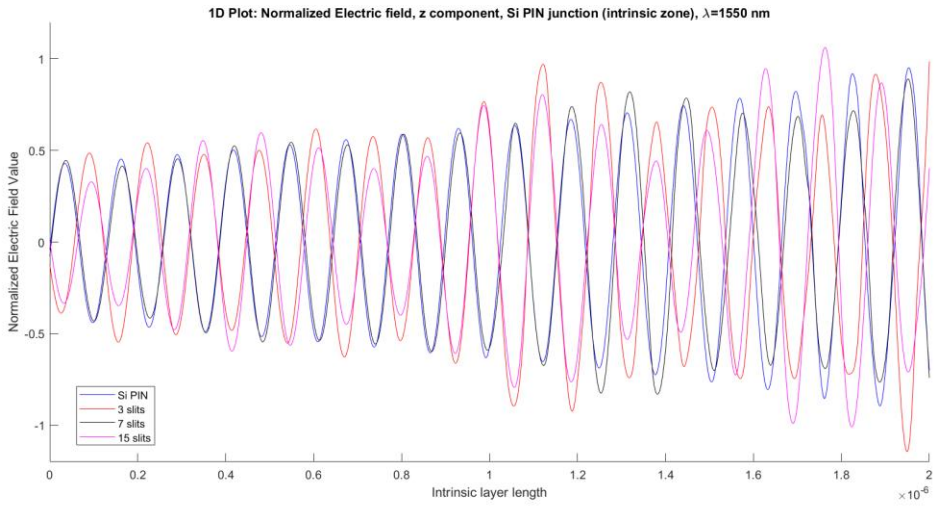

Figure 4.11 – 1D Plot of the normalized electric field, z-component, along the intrinsic zone (for a light wavelength of 530 nm)

For all cases, the electric field is stronger in the n-junction and then slowly decreases along the intrinsic zone.

By analysing *Figure 4.11*, we observe that the results obtained for a normalized electric field with and without nanoantennas are very similar. And so, the introduction of nanoantennas for solar harvesting barely contributes for a bigger efficiency of the solar cell.

For a light wavelength of 800 nm, the EOT phenomenon does not occur if the metal thickness is λ/10. For a metal thickness of λ/100, the EOT phenomenon occurs for every case and thus we can conclude that the nanoantennas are indeed efficient for this wavelength where λ/100 is the optimum thickness.

Below in *Figure 4.12*, there are represented the cases where the EOT phenomenon occurs.

a. For a metal thickness of λ/100 and air slit width λ/2:

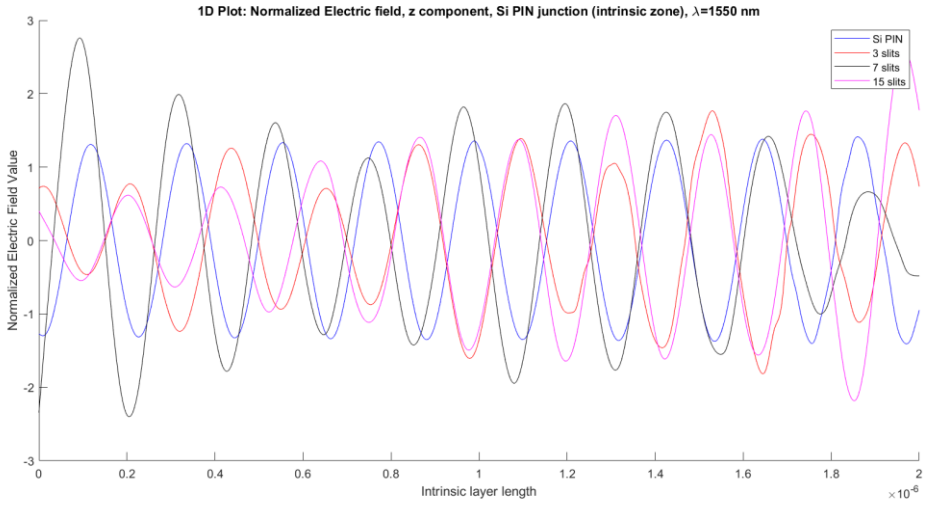

Figure 4.12 – 1D Plot of the normalized electric field, z-component, along the intrinsic zone (light wavelength: 800 nm; metal thickness: λ/100; air slit width: λ/2)

By analysing *Figure 4.12*, although the 15-slit array nanoantenna has recorded the maximum absolute value of the normalized electric field, the seven-slit array is the most efficient nanoantenna type, as the normalized electric field is higher along the entire intrinsic zone.

b. for a metal thickness of λ/100 and air slit width λ/5:

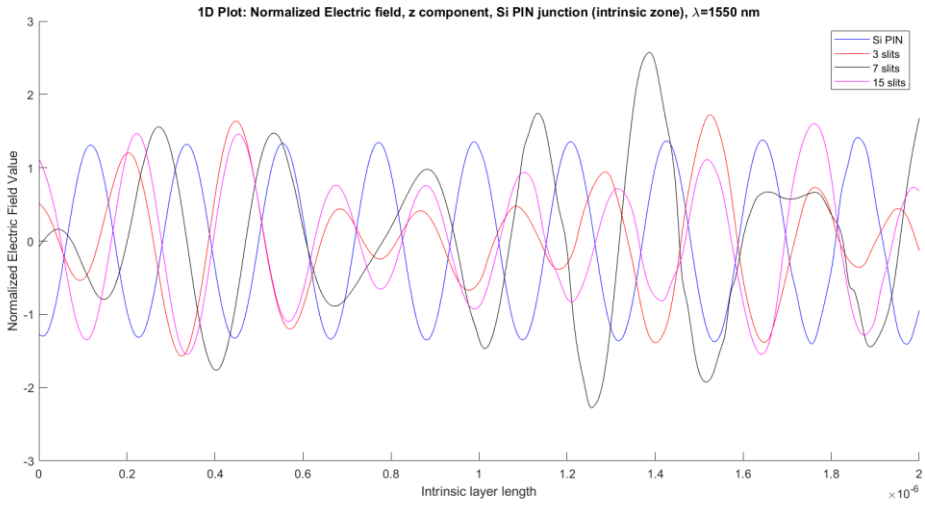

Figure 4.13 – 1D Plot of the normalized electric field, z-component, along the intrinsic zone (light wavelength: 800 nm; metal thickness: λ/100; air slit width: λ/5)

By analysing *Figure 4.13*, one can conclude that a seven-slit array nanoantenna is the most efficient along the intrinsic zone.

c. For a metal thickness of λ/100 and air slit width λ/10:

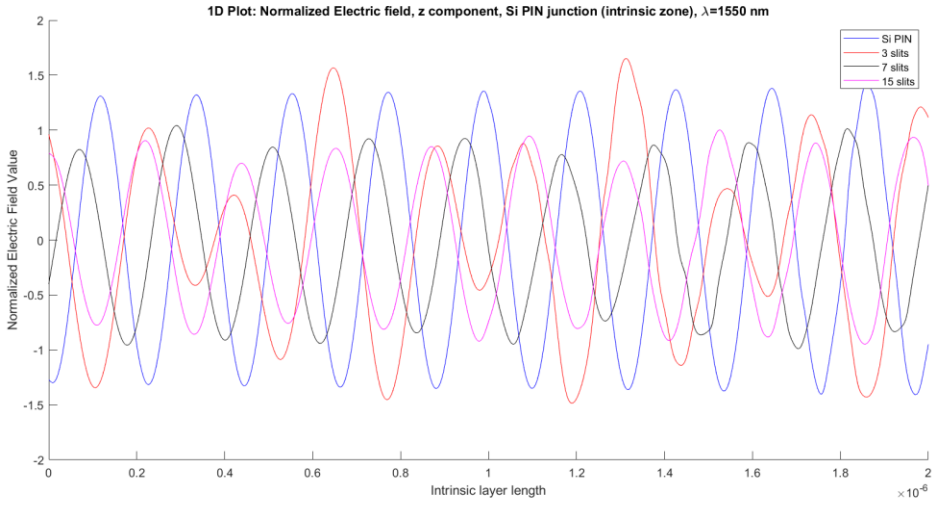

Figure 4.14 – 1D Plot of the normalized electric field, z-component, along the intrinsic zone (light wavelength: 800 nm; metal thickness: λ/100; air slit width: λ/10)

Even though there is the occurrence of EOT, the nanoantennas are less efficient for this air slit width and thus there is no visible advantage on their implementation.

For a light wavelength of 1550 nm, the EOT phenomenon occurred only for the metal thickness λ/100, where this phenomenon was stronger for the air slit width of λ/2 and λ/5.

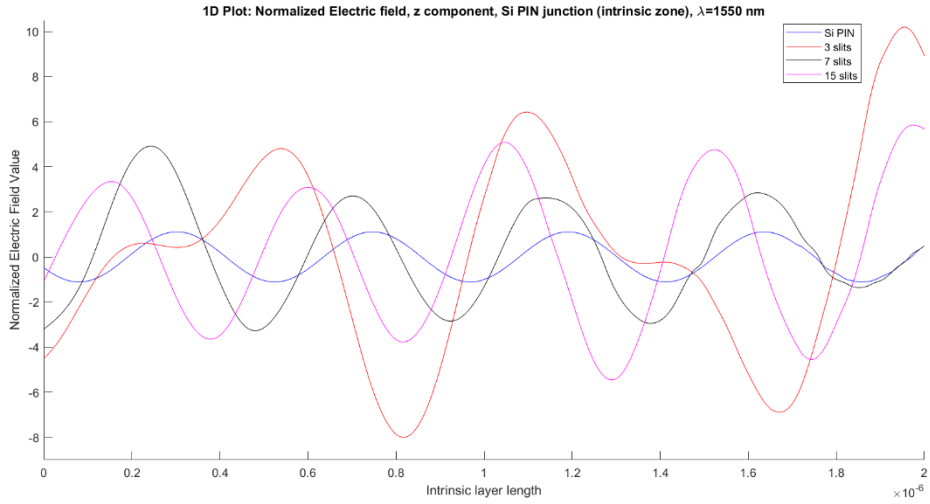

Figure 4.15 – 1D Plot of the normalized electric field, z-component, along the intrinsic zone (light wavelength: 1550 nm; metal thickness: λ/100; air slit width: λ/2)

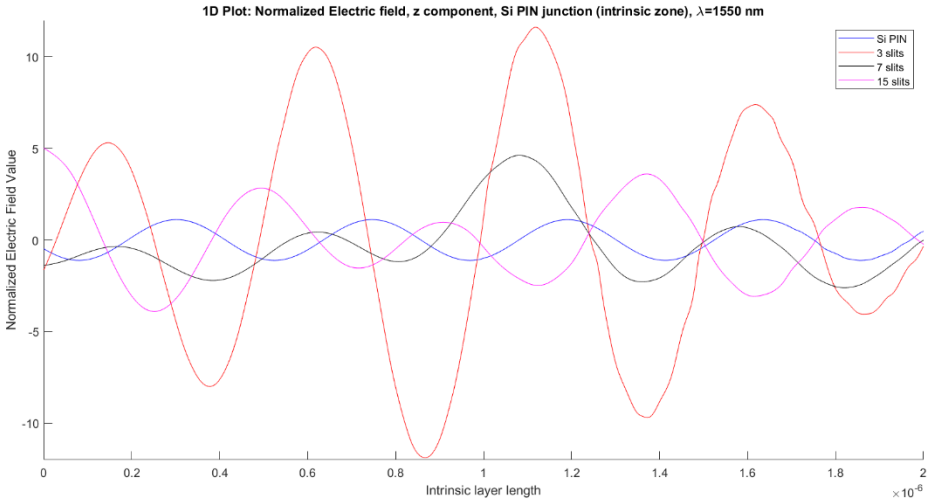

Figure 4.16 – 1D Plot of the normalized electric field, z-component, along the intrinsic zone (light wavelength: 1550 nm; metal thickness: λ/100; air slit width: λ/5)

The EOT phenomenon is mostly present for a three-slit and a fifteen-slit array nanoantenna. Furthermore, the 3-slit array nanoantenna has recorded on both cases a maximum absolute value of the normalized electric field above 10 times higher than the incident electric field.

On *Figure 4.17* it is represented the result of the simulation for a three-slit array, whose metal thickness is λ/100 and the air slit width is λ/5:

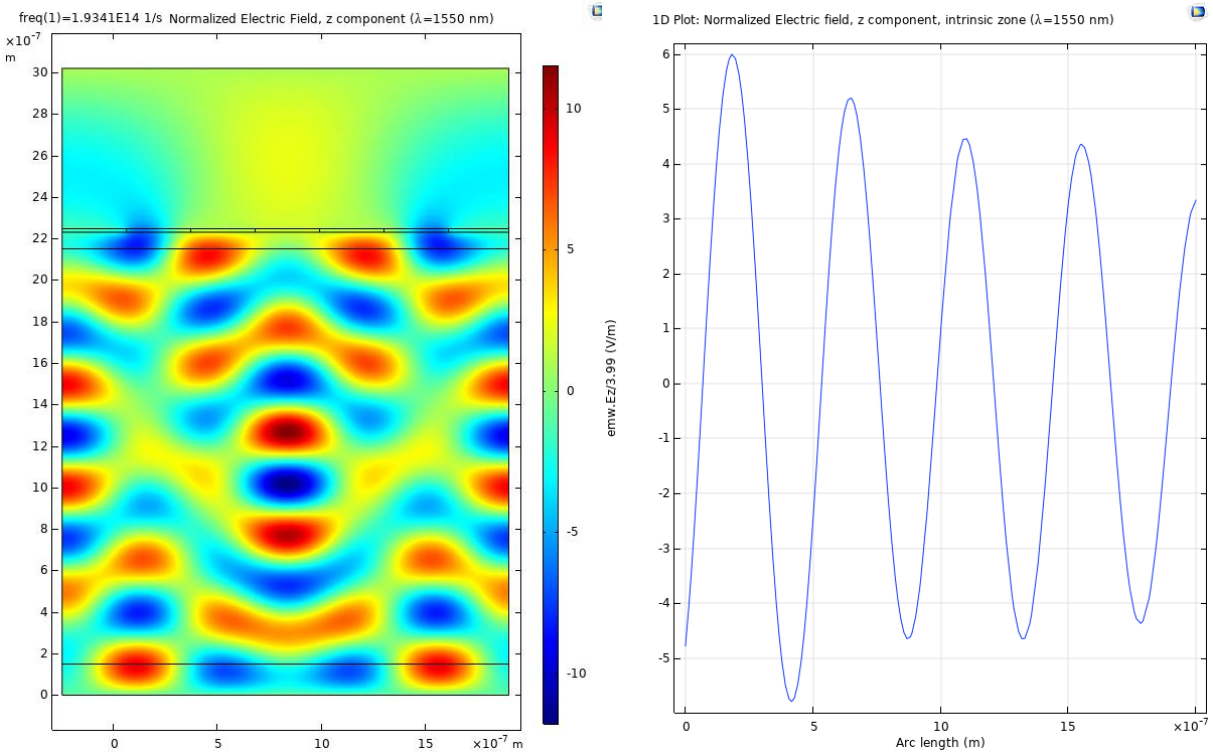

(a) **(b)**

Figure 4.17 – Simulation results for a three-slit array nanoantenna
(Light wavelength: 1550 nm; Metal thickness: λ/100; Air slit width: λ/5)

(a) Normalized Electric field, z-component (zoomed section of a PIN junction)
(b) 1D Plot of the Normalized Electric field, z-component along the intrinsic zone

On Figure 4.17 **(a)** we can observe a pattern of maximum and minimum points of the electric field, due to wave interference.

The result obtained is quite interesting, since the diffraction pattern resulting from a gap spacing of λ/5 and a metal thickness of λ/100 reaches values that are much higher compared to those obtained for other spacing.

The realization of these simulations allowed to better understand the concept of diffraction of light through air slits and the influence their size and their spacing imply on the intensity of the light wave that will be transmitted.

4.3.3. Study of other nanoantenna material types

The procedures that are necessary to carry out the study and simulation of an array of slits with different material types are identical to those used in the previous subchapter.

The metals that will be considered in the following simulations using the COMSOL Multiphysics® software, are gold and platinum.

In *Tables 4.4* and *4.5* are registered the maximum absolute values of the normalized electric field along the intrinsic region for a nanoantenna of gold and for another of platinum, respectively, on top of a silicon PIN junction.

Table 4.4 – Maximum absolute values of the normalized electric field along the intrinsic region (gold nanoantenna)

Light wavelength	Metal thickness	Air slit width	Array of 3 slits	Array of 7 slits	Array of 15 slits
400 nm	λ/10	λ/10	0.2284	0.3407	0.1711
	λ/100	λ/5	0.5390	0.5413	0.4829
		λ/10	0.5710	0.5701	0.5219
530 nm	λ/10	λ/10	0.6569	0.9128	0.3016
	λ/100	λ/5	**1.0770**	0.9547	0.9022
		λ/10	0.9317	0.9277	0.8997
800 nm	λ/10	λ/10	0.7553	0.2352	0.3181
	λ/100	λ/5	**1.3924**	**1.4130**	**1.2796**
		λ/10	**1.0834**	**1.0579**	**1.1441**
1550 nm	λ/10	λ/10	0.0447	0.076	0.2074
	λ/100	λ/5	**3.4412**	**4.4891**	**2.8097**
		λ/10	**1.5027**	**1.4073**	**2.5249**

Table 4.5 – Maximum absolute values of the normalized electric field along the intrinsic region (platinum nanoantenna)

Light wavelength	Metal thickness	Air slit width	Array of 3 slits	Array of 7 slits	Array of 15 slits
400 nm	λ/10	λ/10	0.1303	0.2228	0.1516
	λ/100	λ/5	0.5837	0.5775	0.5694
		λ/10	0.5721	0.5777	0.9688
530 nm	λ/10	λ/10	0.2101	0.4107	0.1970
	λ/100	λ/5	**1.0125**	**1.0016**	0.9937
		λ/10	**1.2147**	0.9568	0.9677
800 nm	λ/10	λ/10	0.1909	0.1386	0.1446
	λ/100	λ/5	**1.5880**	**1.5906**	**1.2431**
		λ/10	**1.2609**	**1.0482**	**1.1048**
1550 nm	λ/10	λ/10	0.0531	0.1105	0.0312
	λ/100	λ/5	**1.6631**	**1.7264**	**2.3329**
		λ/10	**1.3170**	**1.2530**	**1.2338**

From the observation of both tables above and comparing the results with an aluminum nanoantenna in *Table 4.3*, one can verify that the EOT phenomenon is present in all material types. In addition, it is possible to observe that the EOT phenomenon is stronger with an aluminum nanoantenna as maximum absolute values of the normalized electric field along the intrinsic region of 10 times the incident field were registered for a three-slit array nanoantenna.

For a gold or a platinum nanoantenna, the results obtained show that the EOT phenomenon is mostly present for the light wavelengths of 800 nm and 1550 nm.

These results show clear evidence of the EOT phenomenon and constitute an interesting result for the implementation of an aperture nanoantenna, since the electric field in the near field region is strongly enhanced.

In Figure 4.18, we compare the case where the maximum absolute value of the normalized electric field along the intrinsic region for an aluminum nanoantenna on top of a Si PIN junction had the highest value, with the other nanoantenna material types.

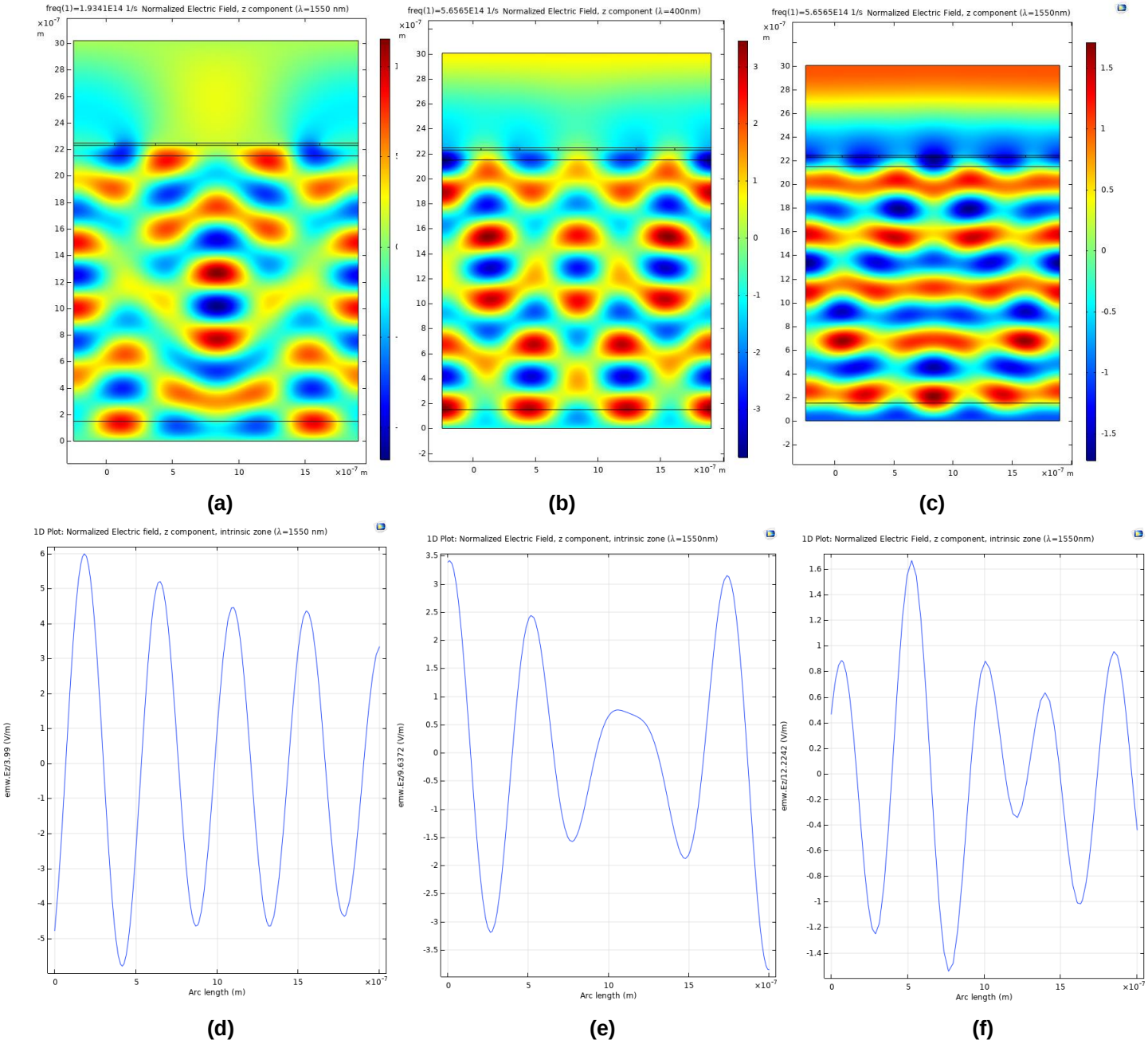

Figure 4.18 – Simulation results for a three-slit array nanoantenna
(Light wavelength: 1550 nm; Metal thickness: λ/100; Air slit width: λ/5)

(a) (b) (c) Normalized Electric field, z-component (zoomed section of a PIN junction)
(d) (e) (f) 1D Plot of the Normalized Electric field, z-component along the intrinsic zone

Figure 4.18 **(a)** and **(d)** have the results obtained for an aluminum nanoantenna, while **(b)** and **(e)** for a gold nanoantenna and **(c)** and **(f)** for a platinum nanoantenna.

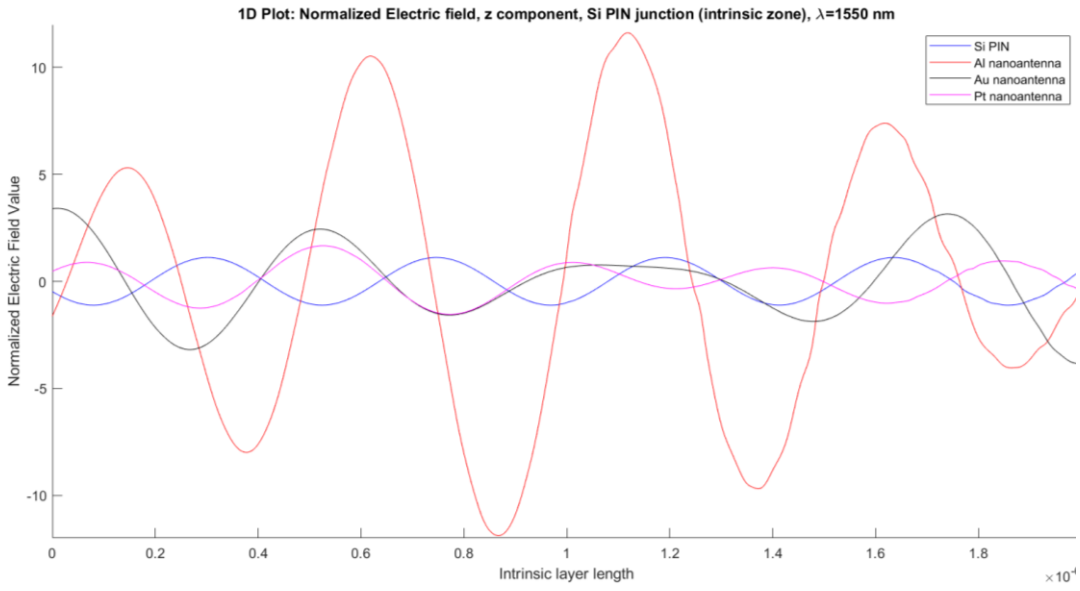

Figure 4.19 – 1D Plot of the normalized electric field, z-component, along the intrinsic zone for different nanoantenna material types
(three-slit array; light wavelength: 1550 nm; metal thickness: λ/100; air slit width: λ/5)

From *Figure 4.19* for this particular case, it is clearly visible the difference of the normalized electric field along the intrinsic zone for the aluminum nanoantenna and the other material types.

For the same metal thickness and air slit width, in *Figures 4.20* and *4.21* are represented the simulation results for a seven-slit array and a fifteen-slit array, respectively, for the three nanoantenna materials and the Si PIN junction.

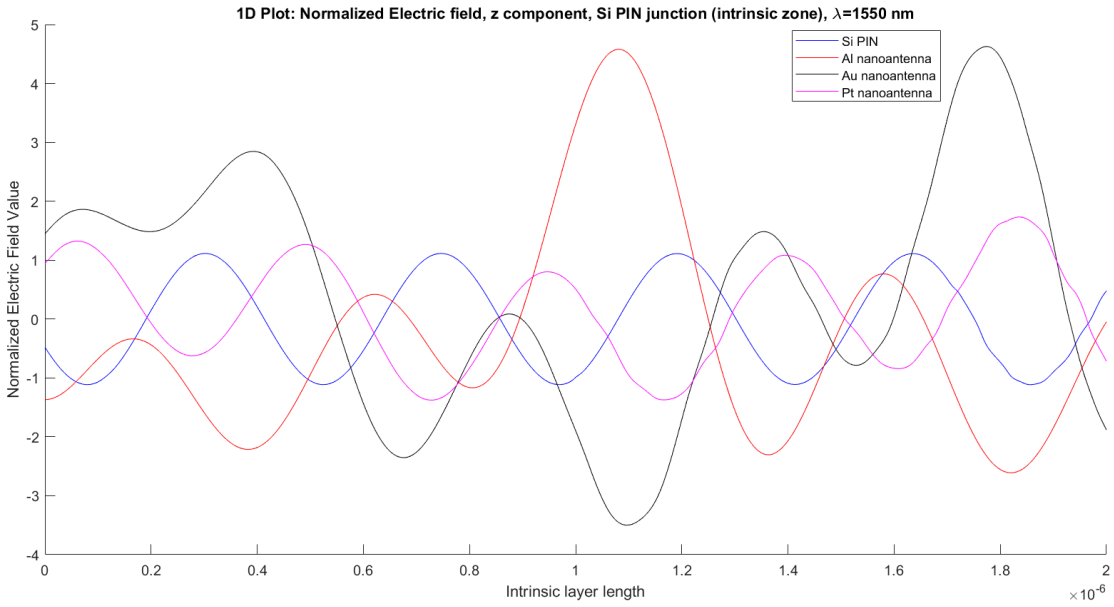

Figure 4.20 – 1D Plot of the normalized electric field, z-component, along the intrinsic zone for different nanoantenna material types
(seven-slit array; light wavelength: 1550 nm; metal thickness: λ/100; air slit width: λ/5)

From the observation of *Figure 4.20*, we verify that the aluminum and the gold nanoantenna have by far a stronger normalized electric field along the entire intrinsic region compared to the platinum nanoantenna and the case without any nanoantennas.

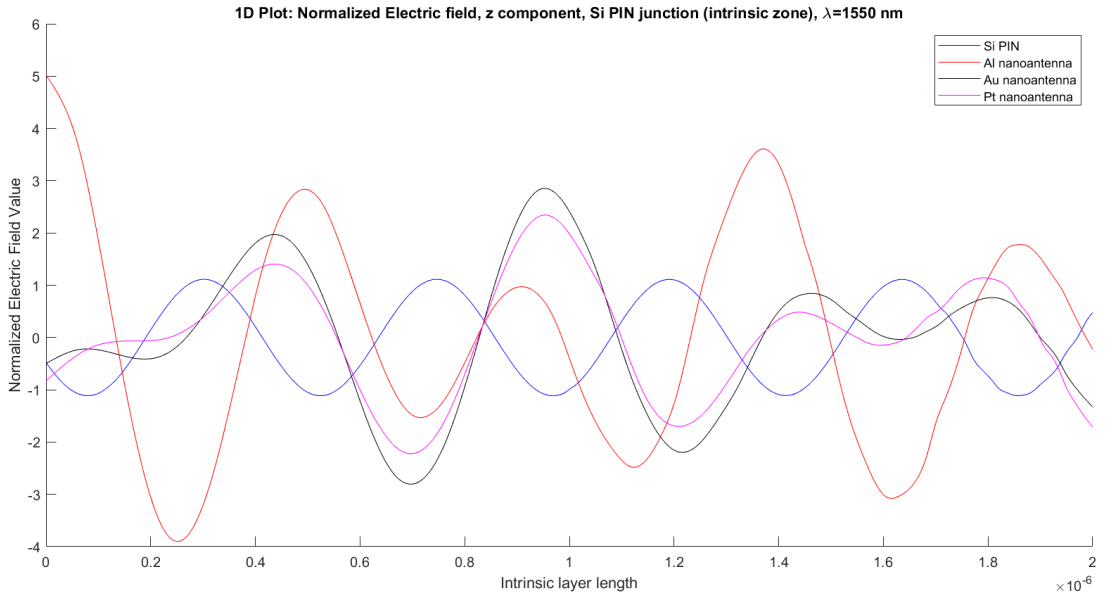

Figure 4.21 – 1D Plot of the normalized electric field, z-component, along the intrinsic zone for different nanoantenna material types
(fifteen-slit array; light wavelength: 1550 nm; metal thickness: λ/100; air slit width: λ/5)

By analyzing all the cases above, one can conclude that aluminum is the most appropriate material for the application of an optical antenna.

4.3.4. Study of the short-circuit current and the open-circuit voltage on the solar cell

We have seen in chapter 3 that a solar cell is commonly modelled using the single diode and 3 parameters model, that includes the I-V and the P-V characteristics of a typical module.

The problem of modelling a PV system is further compounded by the fact that the I-V curve of a PV module is dependent on the irradiance and temperature, which are continuously changing. Consequently, the parameters required to model a PV module must be adjusted according to the ambient temperature and irradiance [56]. Two main parameters that are used to characterize the performance of a solar cell are the short-circuit current, J_{SC}, and the open-circuit voltage, V_{OC}:

a) Short-circuit current, I_{SC}

The short-circuit current is a fundamental parameter of a PV cell. It is dependent upon irradiance and temperature.

To prove that the model used during the simulations on COMSOL Multiphysics® is indeed a solar cell, the short-circuit current was measured upon variation of the irradiance. As the software does not simulate directly the short-circuit current in the cell, a simulation of the current density norm, J_{SC}, was made. In this simulation, the solar cell was short-circuited as depicted in *Figure 4.22*:

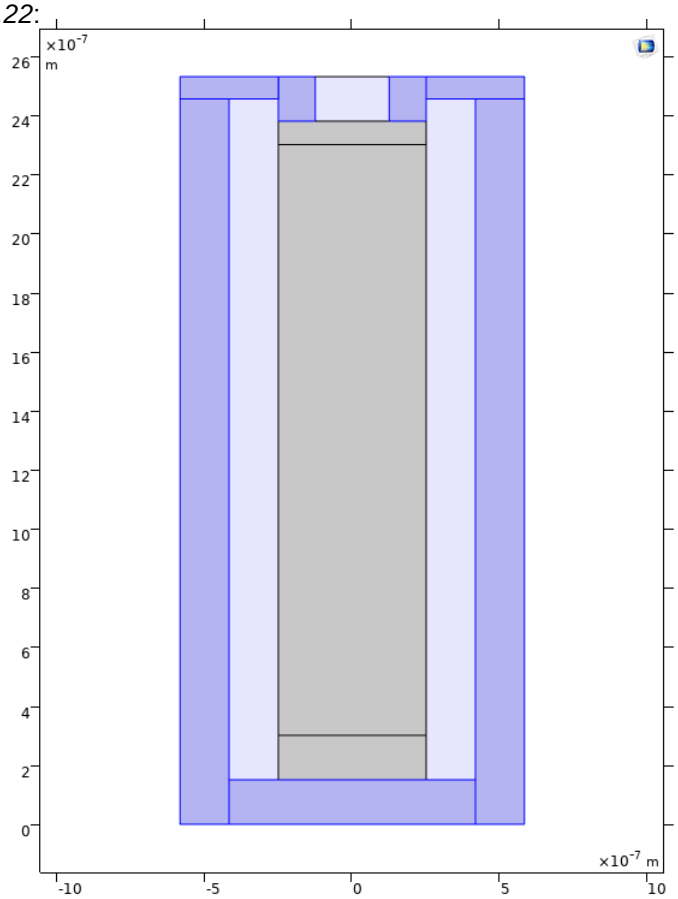

Figure 4.22 – Short-circuited solar cell model
(grey: Si PIN junction; dark blue: Aluminium; light blue: Air)

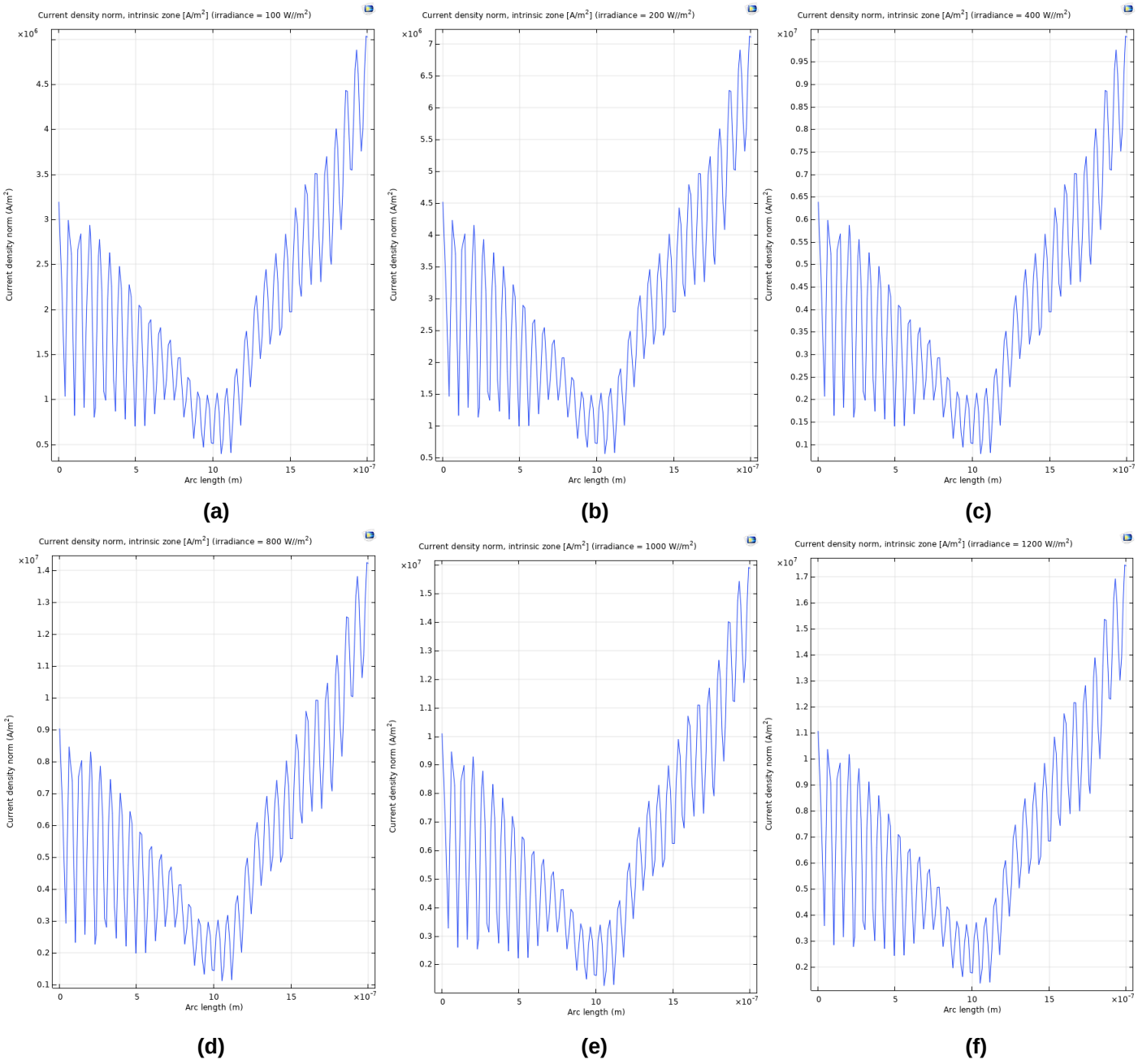

Figure 4.23 – Simulation results for the current density norm along the intrinsic zone
Irradiance:
(a) 100 W/m² **(b)** 200 W/m² **(c)** 400 W/m² **(d)** 800 W/m² **(e)** 1000 W/m² **(f)** 1200 W/m²

According to **[66]** Ibrahim *et al.*, the complete equation for the short-circuit current, considering that it varies with the irradiance and the temperature on the solar cell, is the following:

$$I_{SC}(G,T) = \frac{G}{G^r} \cdot [I_{SC}^r + \mu_{SC} \cdot (T - T^r)] \qquad (4.1)$$

where μ_{SC} is the thermal coefficient of the short-circuit current [A/ºC]: it measures the variation of I_{SC} with an increase of 1ºC of temperature T.

The influence of the temperature variation on the short-circuit current I_{SC} is almost negligible. Although COMSOL can simulate the variation of the temperature, during the simulations the temperature T on the PV cell is considered to be constant and equal to STC. Thus, for this simulation we will take into account the *Equation 3.9* and recalling that the software does not simulate directly the short-circuit current in the cell, but the current density norm:

$$I_{SC} = \frac{G}{G^r} \cdot I_{SC}^r \Leftrightarrow \frac{I_{SC}}{A} = \frac{G}{G^r} \cdot \frac{I_{SC}^r}{A} \Leftrightarrow J_{SC} = \frac{G}{G^r} \cdot J_{SC}^r \qquad (4.2)$$

where J_{SC} is the current density norm.

After observation of the *Figure 4.23*, we will take note of the average value of the current density norm for the cases presented below:

Table 4.6 – Average values of the current density norm

Irradiance [W/m²]	**Current Density Norm** [x 10⁶ A/m²]		
	Min.	Max.	**Average Value**
400	0.88	10.05	**5.47**
500	0.92	11.25	**6.09**
600	1.00	12.33	**6.67**
700	1.10	13.30	**7.20**
800	1.20	14.20	**7.70**
900	1.25	15.10	**8.18**
1000	1.28	15.97	**8.63**
1100	1.35	16.78	**9.07**
1200	1.40	17.60	**9.50**
1300	1.48	18.33	**9.91**
1400	1.60	18.96	**10.28**

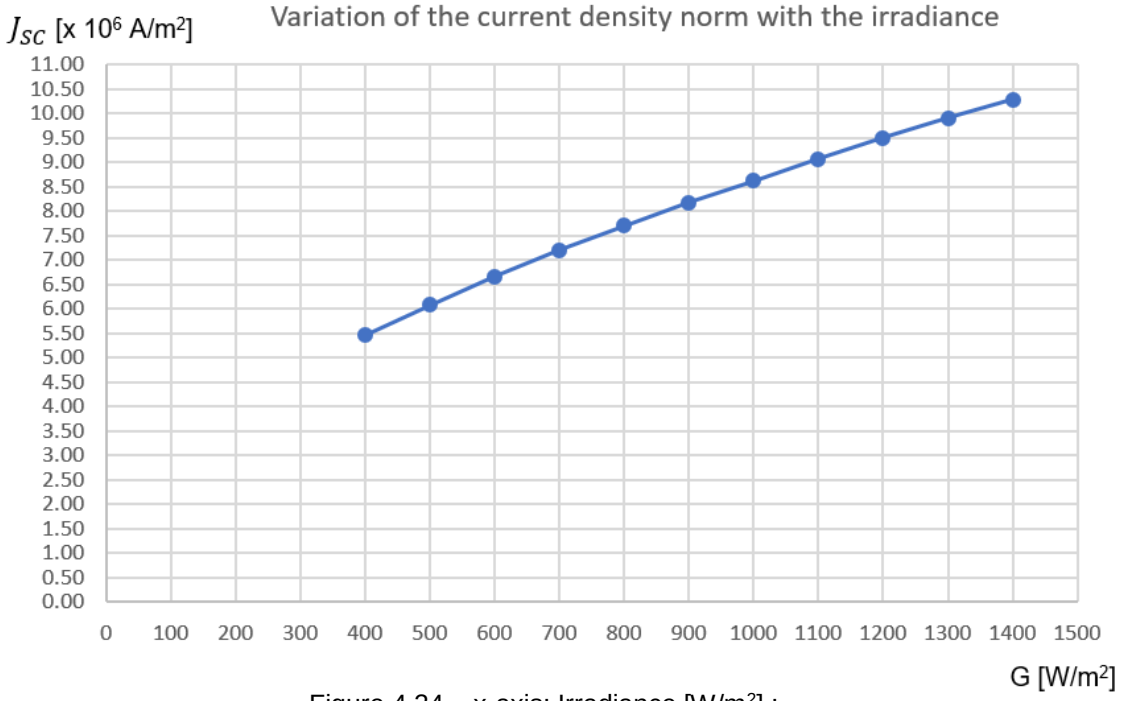

Figure 4.24 – x-axis: Irradiance [W/m²] ;
y-axis: Average value of the current density norm [x 10⁶ A/m²]

From *Figure 4.24*, we can see that the current density norm varies almost linearly with the input irradiance for this range of values on the PV cell. The slight non-linearity can be attributed to the resistance of the material (in this case, aluminum). The resistance of any material is a function of the material's resistivity, ρ, and the material's dimensions [68], and it is given by:

$$R = \frac{\rho \cdot L}{t \cdot W} \qquad (4.3)$$

where L, t and W are the length, the thickness and the width of the material, respectively.

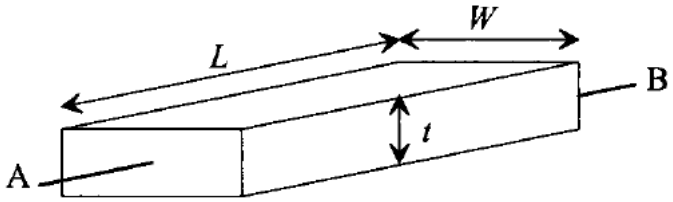

Figure 4.25 – Calculation of the resistance of a rectangular block of material [68]

Electrical resistivity is the ability of a material to resist an electric current. The SI unit of electrical resistivity is the ohm-meter (Ω·m). The resistivity of aluminum at 20ºC is known and equal to $2.65\text{x}10^{-8}\ \Omega \cdot \text{m}$ [69].

The electrical resistivity of most materials changes with temperature. If the temperature T on the PV cell does not vary too much, a linear approximation is typically used:

$$\rho\,(T) = \rho_0 \cdot [1 + \alpha \cdot (T - T_0)] \qquad (4.4)$$

where α is called the temperature coefficient of resistivity, T_0 is a fixed reference temperature, and ρ_0 is the resistivity at temperature T_0. The parameter α is an empirical parameter fitted from measurement data.

At STC the reference temperature of the PV cell is $T = 25ºC$. From **[69]**, we know that at $T_0 = 20ºC$ the resistivity of aluminum is $\rho_0 = 2.65\text{x}10^{-8}\Omega \cdot \text{m}$ and the temperature coefficient of resistivity is $\alpha = 0.00390$. Thus, it is possible to calculate the resistivity, ρ, using the linear approximation on *Equation 4.4*: $\rho\,(T = 25ºC) = 2.70\text{x}10^{-8}\Omega \cdot \text{m}$

And so, the resistance of the aluminium can be calculated. Knowing that we have different aluminium sections in the short-circuited PV cell model, we have to calculate the resistance for each section.

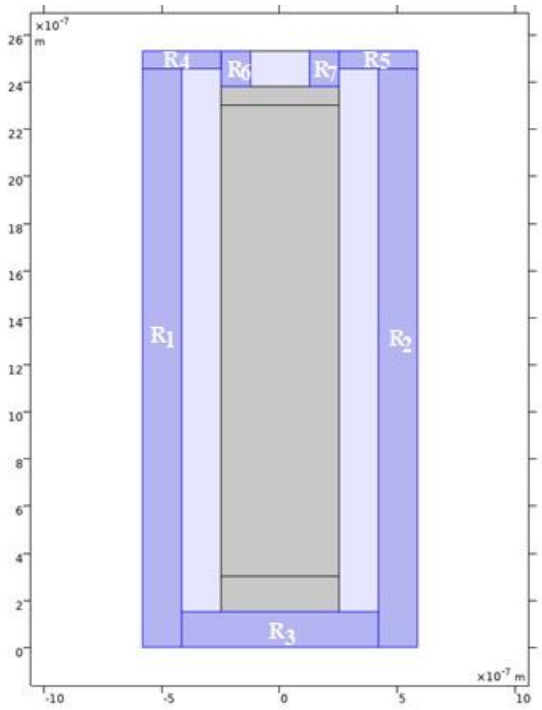

Figure 4.26 – Short-circuited solar cell with each block numerated
(grey: Si PIN junction; dark blue: Aluminum; light blue: Air)

On this model, the thickness t is equal to 640 nm and the length L and width W of each block is represented on *Table 4.7*.

Table 4.7 – Aluminum sections dimensions

Section	**Length, L** [m]	**Width, W** [m]
$\boldsymbol{R_1}$	$2.455\text{x}10^{-6}$	$1.666\text{x}10^{-7}$
$\boldsymbol{R_2}$	$2.455\text{x}10^{-6}$	$1.666\text{x}10^{-7}$
$\boldsymbol{R_3}$	$150\text{x}10^{-9}$	$8.335\text{x}10^{-7}$
$\boldsymbol{R_4}$	$0.075\text{x}10^{-6}$	$3.336\text{x}10^{-7}$
$\boldsymbol{R_5}$	$0.075\text{x}10^{-6}$	$3.336\text{x}10^{-7}$
$\boldsymbol{R_6}$	$150\text{x}10^{-9}$	$1.25\text{x}10^{-7}$
$\boldsymbol{R_7}$	$150\text{x}10^{-9}$	$1.25\text{x}10^{-7}$

The resistance for each section is given by:

$$R_1 = R_2 = \frac{2.70\text{x}10^{-8}\cdot 2.455\text{x}10^{-6}}{640\text{x}10^{-9}\cdot 1.666\text{x}10^{-7}} = 621.447\ m\Omega \qquad (4.5)$$

$$R_3 = \frac{2.70\text{x}10^{-8}\cdot 150\text{x}10^{-9}}{640\text{x}10^{-9}\cdot 8.335\text{x}10^{-7}} = 7.592\ m\Omega \qquad (4.6)$$

$$R_4 = R_5 = \frac{2.70\text{x}10^{-8}\cdot 0.075\text{x}10^{-6}}{640\text{x}10^{-9}\cdot 3.336\text{x}10^{-7}} = 9.485\ m\Omega \qquad (4.7)$$

$$R_6 = R_7 = \frac{2.70\text{x}10^{-8}\cdot 150\text{x}10^{-9}}{640\text{x}10^{-9}\cdot 1.25\text{x}10^{-7}} = 50.625\ m\Omega \qquad (4.8)$$

By analyzing the values of the resistance for each block of aluminum, one can conclude that the resistance is an important factor to consider. All the values obtained for the resistance of each block agree with the 0.35 µm CMOS process. Therefore, the non-linearity of the current density norm with the input irradiance is explained. It is feasible to conclude that the current density norm obeys the *Equation 4.2* and thus it is directly dependent on the input irradiance, and so does the short-circuit current, I_{SC}.

b) Open-circuit voltage, V_{OC}

The open-circuit voltage, V_{OC}, has a very small variation with the irradiance and temperature.

We have seen in Chapter 3 that the PV cell can be described through the equivalent electric circuit of a single diode. Its current–voltage characteristic (I-V curve) has an exponential growth, therefore the open-circuit voltage, V_{OC}, does not vary that much with a big increase of the short-circuit current, I_{SC}. A variation of the short-circuit current, I_{SC}, would represent a vertical movement of the red curve on *Figure 5.24.* Graphically, we are able to see that the open-circuit voltage would not vary too much with a vertical movement of the red curve.

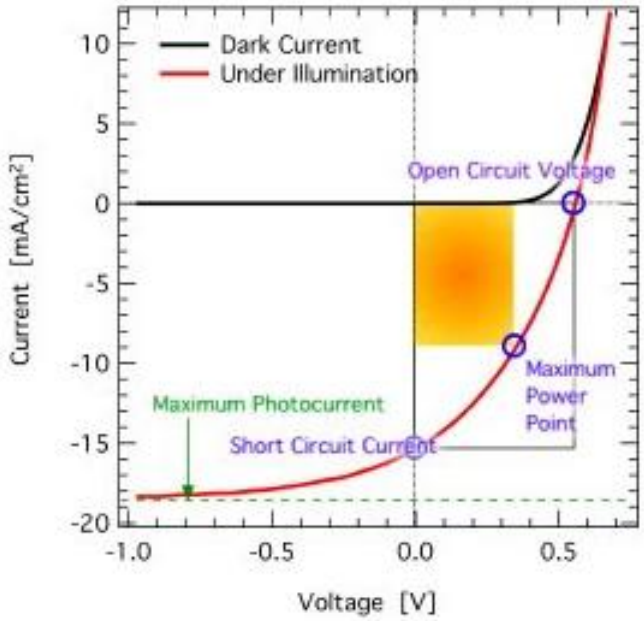

Figure 4.27 – I-V curve of a PV cell [70]
yellow rectangle: Fill factor

On COMSOL Multiphysics® software, the open-circuit voltage was measured for different values of the irradiance:

Table 4.8 – Values of the open-circuit voltage with the irradiance

Irradiance [W/m²]	Open-circuit voltage [V]		
	Point 1	Point 2	V_{OC}
100	-4.5189	-5.3311	0.8121
200	-4.5189	-5.3311	0.8121
400	-4.5189	-5.3311	0.8121
800	-4.5189	-5.3311	0.8121
1000	-4.5189	-5.3311	0.8121
1200	-4.5189	-5.3311	0.8121

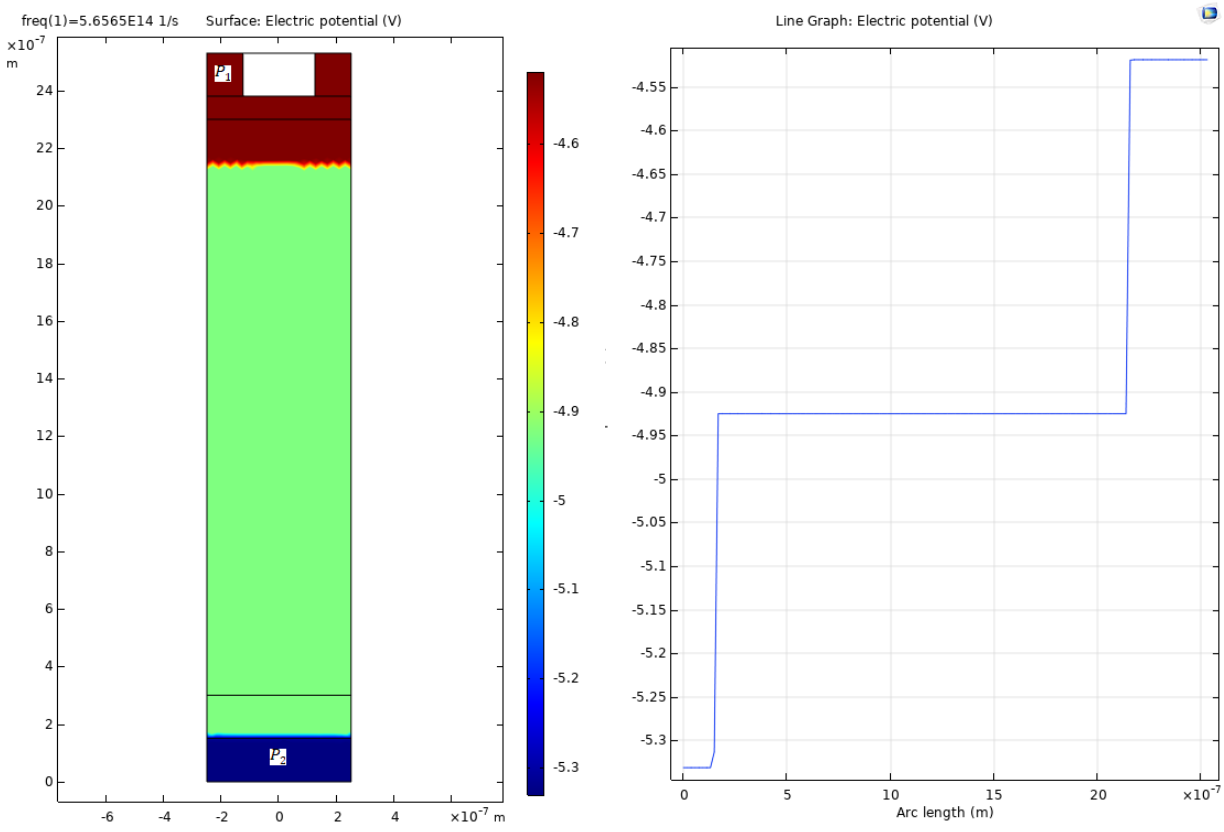

(a) **(b)**

Figure 4.28 – Measurement of the electric potential on open-circuited PV cell
(a) 2D model of the PV cell
(b) 1D Plot of the electric potential along the PV cell

P_1 and P_2, on *Figure 4.28* (a), are the two points represented on *Table 4.8*.

The open-circuit voltage has a steady value equal to 0.8121 V, for different values of the irradiance, G, and so we can conclude that it is not dependent on the irradiance. This value is the maximum voltage the solar cell on this model can deliver.

According to **[66]** *Ibrahim et al.*, the open–circuit voltage V_{OC} exhibits a strong dependence on temperature. Yet, its dependence on the irradiance, G, is not very significant and follows a logarithmic function, as seen in *Equation 4.9*:

$$V_{OC}(G,T) = V_{OC}^{r} + \frac{N_S \cdot k \cdot T}{q} \cdot \ln(G) + \mu_{OC} \cdot (T - T^{r}) \qquad (4.9)$$

where N_S is the number of series-connected cells in a PV module (in the case of a single PV cell, this value is equal to 1) and μ_{OC} is the thermal coefficient of the open-circuit voltage [V/ºC]: it measures the variation of V_{OC} with an increase of 1ºC of temperature T.

In addition, they state that there is a method of expressing V_{OC} as a function of T, which is as follows:

$$V_{OC}(T) = V_{OC}^{r} + \mu_{OC} \cdot (T - T^{r}) \qquad (4.10)$$

Therefore, we can conclude that the open–circuit voltage V_{OC} is not weakly dependent on the irradiance, G, which agrees with the results obtained in this study: the open–circuit voltage, V_{OC}, did not change with the input irradiance.

To conclude, we have seen that the short-circuit current, I_{SC}, varies nonlinearly with irradiance and its variation with temperature is fairly small depending on its temperature coefficient. When determining the dependence of the open-circuit voltage, V_{OC}, on temperature and irradiance, it is found that it is strongly dependent only on the temperature.

It has been observed that the results obtained in this dissertation are according to what is expected by the classical theory of a photovoltaic cell and so the model that was tested on COMSOL software is valid.

5. Conclusion

5.1. Introduction

The main objective of this dissertation is the study and simulation of the behavior of an optical antenna with subwavelength dimensions for solar harvesting on PV panels. To perform such study, the COMSOL Multiphysics® software was used, to obtain the simulation numerical results of the structures studied on Chapter 4.

This chapter presents a general summary of the conclusions that were made throughout the dissertation as well as some future work proposals.

5.2. Summary

This dissertation was carried out in several stages:

- from the research on the subject, through several scientific articles, papers, books, course lectures, thesis and the Internet, which is important for the realization of the state of the art (Chapter 2);
- the analytical model and the structure of a solar cell that is analysed during this work and its electrical parameters (Chapter 3);
- the introduction of the simulation software and the presentation of the several simulation results (Chapter 4).

With this study it has been verified that the classic diffraction theory by Bethe cannot answer and explain the phenomena that occur in the subwavelength and optical domain, like the Extraordinary Optical Transmission (EOT) and the surface plasmon polaritons (SPPs). The SPPs are crucial for Extraordinary Optical Transmission. This optical phenomenon is what is intended to be observed in the simulation results.

In Chapter 4, it has been demonstrated with several simulations in different conditions that the EOT phenomenon was always confirmed on nanoantennas with three material types: Aluminium (Al), Gold (Au) and Platinum (Pt). Thus, it means that these structures have the capacity to transmit more light than its incidence, in orders of magnitude greater than predicted by standard aperture theory. These experiments provide evidence that these unusual optical properties are due to the coupling of light with SPPs on the surface of the metallic nanoantennas.

In addition, the optical nanoantennas are devices that are capable to absorb various wavelengths of light. It has been verified with the simulation results that optimum results were obtained for light wavelengths of 800 nm and 1550 nm. These results constitute an interesting result for the implementation of an aperture nanoantenna, as they cover a wide range of the spectrum: the EOT phenomenon was verified on almost the entire visible region, as well as the IR region. Typical silicon solar cells have proven to be inefficient at these wavelengths [5].

Although most of the researchers use gold or silver to fabricate the optical antennas, the results obtained in this dissertation show that aluminium can have even better results than the other material types, mainly due to its transmission and reflection coefficients [67]. Additionally, among all metals analysed, aluminium has the smallest skin depth in the visible spectrum, as well as being cheaper than gold or platinum. However, aluminium is unstable. It oxidizes quickly and the optical properties are lost. Therefore, aluminium has to be coated with an anti-oxidant compound.

In addition, it has been demonstrated that both the short-circuit current and the open-circuit voltage both obey the equations of the solar cell model.

5.3. Future work

Since the subject of this dissertation is innovative, in an area that is still little explored, there is a wide range of future work that could be done, with application in several areas.

The first implementation that could be explored would be a performance analysis of a 3D model of a periodic array of slits smaller than the light wavelength using the COMSOL Multiphysics® program. With a 3D model, not only the electric field between slits would be studied into more detail, but also we could analyze the EOT phenomenon and the diffraction of light by slits smaller than its wavelength more effectively. This is a limitation of the 2D model that was used in this dissertation. However, a performance analysis with a 3D model requires a large computational effort and increased memory usage.

Secondly, during this study we have only analyzed the performance of metallic nanoantennas on a solar cell. New simulations could have been made of dielectric nanoantennas, that are optical antennas constructed with dielectric materials, such as silicon which is widely used in nanoelectronics to fabricate transistors and diodes. As seen in subchapter 2.5.1.2, they have several advantages over the metallic ones due to unique features not found in plasmonic nanoantennas, like much lower polarization losses. Due to their characteristics, it would be interesting to study this type of nanoantennas and compare its results with their metallic counterparts.

Also, a techno-economic analysis of the implementation of optical nanoantennas on solar photovoltaic panels into the market would be interesting, in order to better evaluate if this technique is indeed a potential new solution of increasing the conversion efficiency in the near future.

During this dissertation, we lacked to make an estimated evaluation of the conversion efficiency with the introduction of nanoantennas. This is the most common parameter to compare the performance of a solar cell. In order to obtain the conversion efficiency of a solar cell with nanoantennas, having the input power on the PV cell, P_{in}, we would then have to determine short-circuit current, I_{SC}, and the open-circuit voltage, V_{OC}, on the PV cell both with and without nanoantennas. However, the 2D model that was the base of this study had the limitation of guaranteeing that all metallic nanoantennas were touching with the same electric potential. With a 3D model we could make the necessary connections and illuminate the device.

To simplify the calculations, if we consider an ideal solar cell with $FF = 1$, the conversion efficiency would then be given by:

$$\eta = \frac{FF\, I_{SC}\, V_{OC}}{P_{in}} \qquad (5.1)$$

References

[1] "A year in global energy markets", https://www.bp.com/worldenergystatistics2017/, visited on 2nd November 2018

[2] "Renewables 2018", https://www.iea.org/renewables2018/, visited on 2nd November 2018

[3] Michele Gallo *et al.*, Design of optical antenna for solar energy collection; 2011 p.1

[4] Rui Castro, "Uma Introdução Às Energias Renováveis: Eólica, Fotovoltaica e Mini-hídrica"; 2nd ed.; 2012 p. 309

[5] D.K. Kotter *et al.*, Solar nanoantenna electromagnetic collectors, in: 2nd International Conference on Energy Sustainability, August 2008, Jacksonville, Florida, USA

[6] World Energy Council, 2013

[7] Photovoltaic Report, Fraunhofer Institute for Solar Energy Systems, Germany

[8] https://www.altadevices.com/use-gallium-arsenide-solar-cells/, visited on 25th November 2018

[9] http://vragenoverzonnepanelen.nl/zonnepanelen/welke-soorten-zonnepanelen-er/, visited on 25th November 2018

[10] F. Dimroth *et al.*, "Four-Junction Wafer-Bonded Concentrator Solar Cells", IEEE Journal of Photovoltaics, vol. 6, no. 1, pp. 343, 2016

[11] http://www.sunwindenergy.com/news/thin-film-photovoltaic-pv-cells-market-analysis-2020, visited on 2nd November 2018

[12] O' Regan B., Gratzel M., A low-cost, high-efficiency solar cell based on dye-sensitized colloidal TiO2 films. Nature 1991; 353:737–40.

[13] Rodriguez I. *et al.*, "Solar energy harvesting in photoelectrochemical solar cells", J Mater Chem 2007; 17:3205–9.

[14] Perovskite Solar, https://www.perovskite-info.com/perovskite-solar, retrieved on 11th January 2019

[15] "Best Research-Cell Efficiency Chart", https://www.nrel.gov/pv/cell-efficiency.html, visited on 11th January 2019

[16] R. Pernechelle, New Copper Redox Couples for Liquid Dye-Sensitized Solar Cells, KTH Royal Institute of Technology, 2017

[17] "New World Record For Solar Cell Efficiency At 46%", https://www.ise.fraunhofer.de/en/press-media/press-releases/2014/new-world-record-for-solar-cell-efficiency-at-46-percent.html, visited on 27th November 2018

[18] Kempa *et al.*, 2007; Gadalla et al, 2014

[19] Serrano E. *et al.*, Nanotechnology for sustainable energy; 2009 p.1

[20] Light - Britannica Online Encyclopedia, https://www.britannica.com/print/article/340440, visited on 28th October 2019

[21] Christiaan Huygens, https://en.wikipedia.org/wiki/Christiaan_Huygens, visited on 28th October 2019

[22] Lukas Novotny and Bert Hecht, “Principles of Nano-Optics”, Cambridge University Press, 2nd edition, p. 189, 2012

[23] Wave–Particle Duality: De Broglie, Einstein, and Schrödinger. In: Critical Appraisal of Physical Science as a Human Enterprise. Science & Technology Education Library, vol 36. Springer, Dordrecht, 2009

[24] “Light is It a Wave or a Particle?”, https://global.canon/en/technology/s_labo/light/001/11.html, visited on 28th October 2019

[25] A. Ahlbom *et al.*, “Light Sensitivity”, Scientific Committee on Emerging and Newly Identified Health Risks (SCENIHR), European Commission, 2008

[26] António Baptista, Optoelectronics, Solar Cell, slide 12, Instituto Superior Técnico, 2019

[27] D. Kotter *et al.*, “Theory and Manufacturing Processes of Solar Nanoantenna Electromagnetic Collectors”, Journal of Solar Energy Engineering, vol. 132, no. 1, 2010.

[28] I. Maksymov, “Magneto-plasmonic nanoantennas: Basics and applications”; 2016

[29] R. Gomes, “Estudo de uma antena ótica para comunicação intersatélites”, Instituto Superior Técnico, 2016

[30] Q-Han Park, “Optical antennas and plasmonics”, Department of Physics, Korea University, Seoul, 2009

[31] Lukas Novotny, “Antennas for light,” Nat. *Publ. Gr.,* vol. 5, pp. 83-90, 2011.

[32] M. Ameziane, “Solar Nanoantenna Electromagnetic Collectors for Energy Production”; Tampere University of Applied Sciences, 2015

[33] Sen Yan *et al.*, “Optimizing the bowtie nano-rectenna topology for solar energy harvesting applications”; 2017

[34] W.C. Brown, IEEE Transactions on Microwave Theory and Techniques; 1984

[35] A.M Marks, U.S. Patent No. 4445050 (1984), B.J. Zwan, U.S. Patent No. 4251679 (1981)

[36] R. L. Bailey, “A proposed new concept for a solar energy converter”; J. Eng. Gas Turbines Power 94, 73-77, 1972

[37] R. Corkish *et al.*, “Solar Energy Collection by Antennas”, pp. 1, 2013

[38] Nazarov *et al.*, Radiophys. Quantum Electron ; 2010

[39] Lin *et al.*, Investigation of resonance light absorption and rectification by subnanostructures; 1996

[40] Berland *et al.*, Optical rectenna for direct conversion of sunlight to electricity. In National Center for Photovoltaics Program Review Meeting, 2001 p. 323-324

[41] Sarehraz *et al.*, 2005

[42] Moddel & Grover, “Metal Single-Insulator and Multi-Insulator Diodes for Rectenna Solar Cells”, 2013.

[43] G. Vandenbosch and Zhongkun Ma, “Upper bounds for the solar energy harvesting efficiency of nano-antennas”, 2012.

[44] A.E. Krasnok *et al.*, “Optical nanoantennas”, Russian Academy of Sciences, 2013.

[45] F.B. Segerink *et al.*,"A Monopole Antenna at Optical Frequencies: Single-Molecule Near-Field Measurements", IEEE Transactions on Antennas and Propagation, Vol. 55, no. 11, 2007.

[46] T. Kalkbrenner *et al.*, "Optical microscopy via spectral modifications of a nanoantenna," Phys. Rev. Lett. 95, 2005.

[47] A.E. Krasnok *et al.*, "All-dielectric optical nanoantennas", Vol. 20, No. 18, Optics Express, 2012.

[48] J. Wenger, "Aperture optical antennas", École Centrale de Marseille, France

[49] F. Neubrech *et al.*, "Resonances of individual metal nanowires in the infrared", Applied Physics Letters 89, 253104, American Institut of Physics, 2006.

[50] "Opto-mechanical Devices for Measuring Nanoplasmonic Metamaterials", https://www.nist.gov/pml/microsystems-and-nanotechnology-division/photonics-and-plasmonics-group/opto-mechanical-devices, visited on 4th February 2019.

[51] Moddel & Grover, "Applicability of Metal/Insulator/Metal (MIM) Diodes to Solar Rectennas", IEEE Journal of Photovoltaics, Vol. 1, No. 1, 2011**.**

[52] A. Khan *et al.*, "Metal-insulator-metal diodes with sub-nanometre surface roughness for energy-harvesting applications", 2017.

[53] P. Biagioni, *et al.*, "Nanoantennas for visible and infrared radiation," *IOP Science,* vol. 75, 2012.

[54] "Solar Cell Structure",https://www.pveducation.org/pvcdrom/solar-cell-operation/solar-cell-structure, visited on 20th May 2019

[55] "The Working Principle of a Solar Cell", https://ocw.tudelft.nl/wp-content/uploads/solar_energy_section_3.pdf, TU Delft, visited on 20th May 2019

[56] Joseph S. Braley, "Photodetectors", University of Rhode Island, 2008

[57] Rui Castro, "AC Electrical Circuits for non-Electrical Engineers"; ed. 0; 2018 p. 19

[58] "Eis uma nova Amareleja... com um sétimo do custo e agora sem subsídios", https://expresso.pt/dossies/diario/2018-07-25-Eis-uma-nova-Amareleja.-com-um-setimo-do-custo-e-agora-sem-subsidios, visited on 21st May 2019

[59] S. Shakya *et al.*, "Training Manual for Engineers on Solar PV System", Research Gate, 2011

[60] "IV Curve", https://www.pveducation.org/pvcdrom/solar-cell-operation/iv-curve, visited on 22nd May 2019

[61] A. Luque, S. Hegedus, Handbook of Photovoltaic Science and Engineering

[62] Rui Castro, Renewable Sources and Distributed Power Generation, Photovoltaic Energy, slide 15, IST, 2017

[63] Dark IV Measurements,https://www.pveducation.org/pvcdrom/characterisation/dark-iv-measurements, visited on 18th September 2019

[64] COMSOL Multiphysics, *COMSOL Multiphysics® Reference Manual*, 2013

[65] "Polarization definitions", https://ibsen.com/technology-2/polarization-definitions/, visited on 17th June 2019

[66] H. Ibrahim *et al.*, “Variations of PV module parameters with irradiance and temperature”, Science Direct, 9th International Conference on Sustainability in Energy and Buildings, 2017

[67] Lukas Novotny and Bert Hecht, “Principles of Nano-Optics”, Cambridge University Press, 2nd edition, Figure 6.20, p. 198, 2012

[68] R. Jacob Baker, “CMOS Circuit Design Layout and Simulation”, 3rd Edition, 2010, p. 37, ISBN 978-0-470-88132-3, 2010

[69] Raymond A. Serway, “Principles of Physics”, 2nd ed., Fort Worth, Texas; London: Saunders College Pub. p. 602, ISBN 978-0-03-020457-9, 1998

[70] “Intermediate: Current-Voltage Characteristics of Organic Solar Cells”, https://blog.disorderedmatter.eu/2008/03/05/intermediate-current-voltage-characeristics-of-organic-solar-cells/, visited on 27th September 2019

[71] Rui Gomes, “Study of an Optical Antenna for Intersatellite Communications**”**, IST, 2016

[72] “Complex Index of Refraction”, https://www.physicsforums.com/threads/complex-index-of-refraction.103302/, visited on 24th October 2019

[73] “Refractive index database”, https://refractiveindex.info/, visited on 27th October 2019

Appendix A

Index of refraction

It is a dimensionless number that describes how fast light travels through the material. The refractive index of materials varies with the wavelength of light and so will the refraction angle as light goes from one material to another.

When light passes through a medium, some part of it will always be attenuated. This can be conveniently taken into account by defining a complex refractive index, $\underline{n}$. It is used to describe absorbing materials where the electric field is diminished in amplitude as it propagates, given by [72]:

$$\underline{n} = n + i \cdot \boldsymbol{k} \qquad (A.1)$$

The real part of the refractive index, n, is a function of the wavelength and it indicates the phase velocity, the rate at which the wave phase propagates in a medium.

The imaginary part of the complex index of refraction, $\boldsymbol{k}$, is called the extinction coefficient and is directly proportional to the absorption coefficient. It indicates the amount of attenuation when the EM wave propagates through the material. We can insert $\boldsymbol{k}$ into the expression for electric field of a plane EM wave traveling in the z-direction, by relating the complex wave number $\underline{k}$ to the complex refractive index $\underline{n}$, through:

$$\underline{k} = \frac{2\pi \cdot \underline{n}}{\lambda} \qquad (A.2)$$

This can be inserted into the plane wave expression as:

$$E(z,t) = Re\left[E_0 \cdot e^{i\cdot(\underline{k}z-\omega\cdot t)}\right] = Re\left[E_0 \cdot e^{i\cdot\left(\frac{2\pi\cdot(n+i\cdot\boldsymbol{k})\cdot z}{\lambda}-\omega\cdot t\right)}\right] = \\ = e^{-\frac{2\pi\cdot\boldsymbol{k}\cdot z}{\lambda}} \cdot Re\left[E_0 \cdot e^{i\cdot(\underline{k}z-\omega\cdot t)}\right] \qquad (A.3)$$

By observing *Equation (A.3)*, one can conclude that $\boldsymbol{k}$ gives an exponential decay. This has been observed in the Beer-Lambert law, where it relates the attenuation of light to the properties of the material through which the light is traveling.

In this dissertation, four different materials were studied: silicon, aluminum, gold and platinum. The respective indexes of refraction for all materials are shown in *Figures A.1* to *A.4*.

The index of refraction of each material was obtained from a database [73]. For each material, COMSOL software reads two files: one for the index n and the other for the index k. Each file has a list of values that are experimental data from several sources to Drude-Lorentz model. An interpolation function plot is generated by the software from this data.

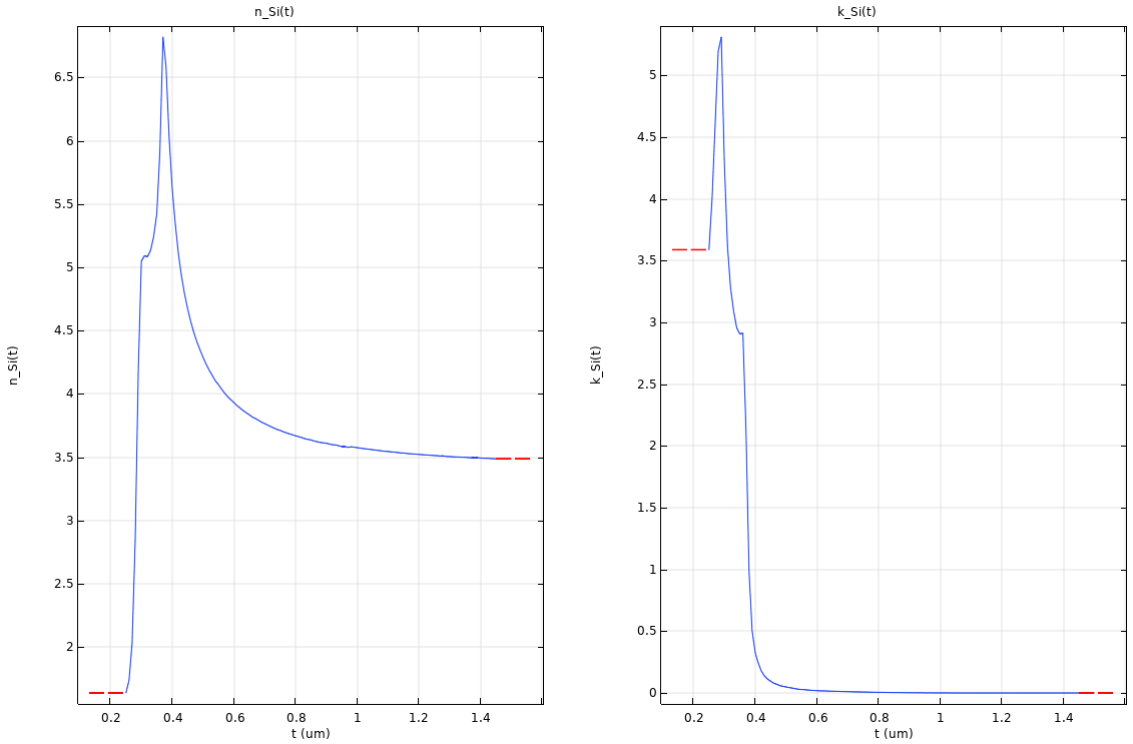

(a) **(b)**

Figure A.1 – Refractive index of Silicon (Si)
(a) n , real part of complex index of refraction
(b) $\boldsymbol{k}$, imaginary part of complex index of refraction

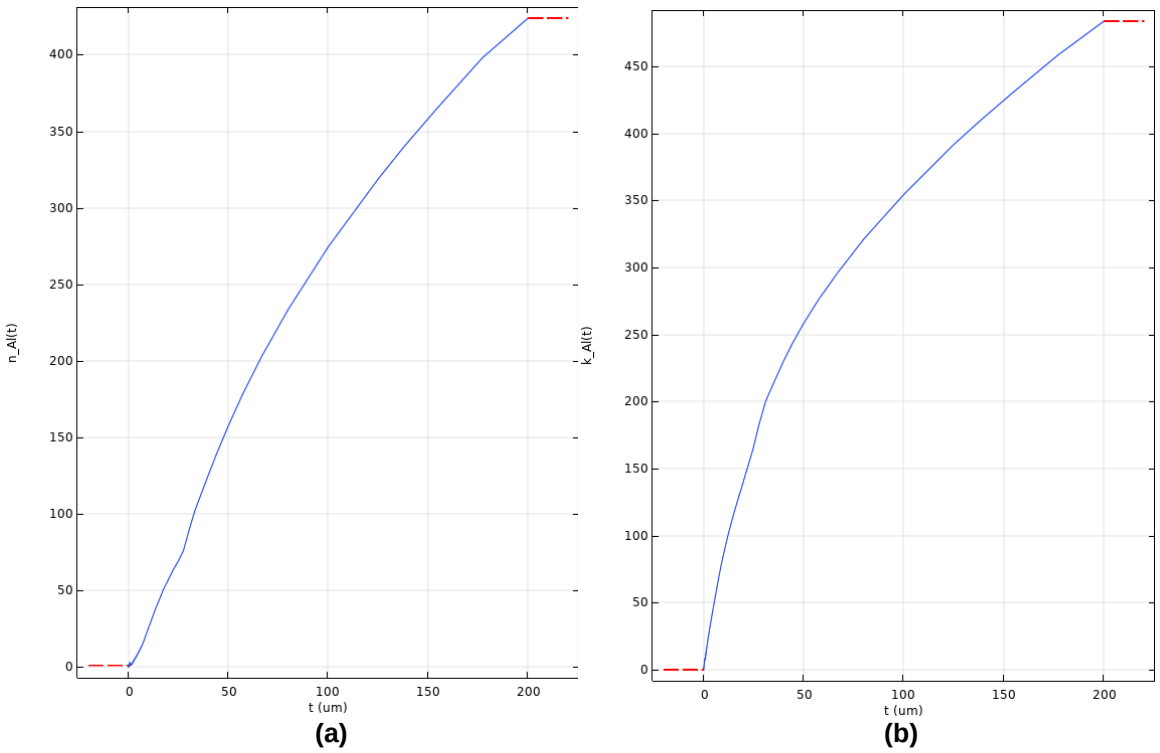

(a) **(b)**

Figure A.2 – Refractive index of Aluminum (Al)
(a) n , real part of complex index of refraction
(b) $\boldsymbol{k}$, imaginary part of complex index of refraction

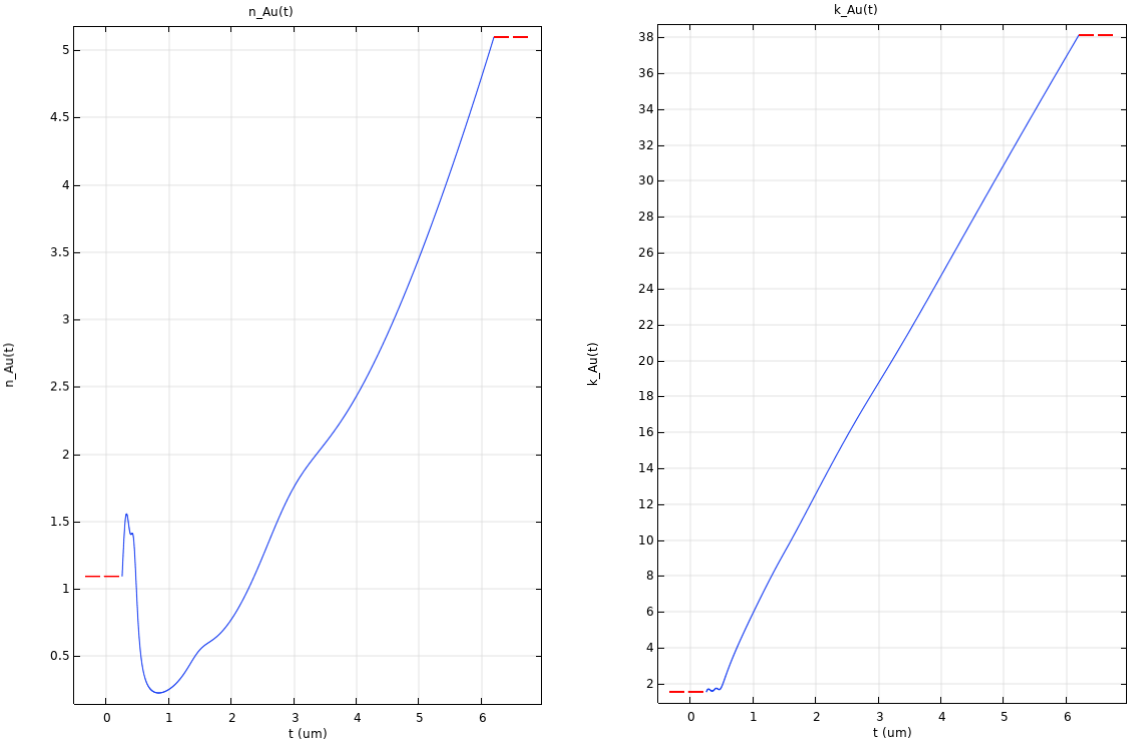

(a) **(b)**

Figure A.3 – Refractive index of Gold (Au)
(a) n , real part of complex index of refraction
(b) $\boldsymbol{k}$, imaginary part of complex index of refraction

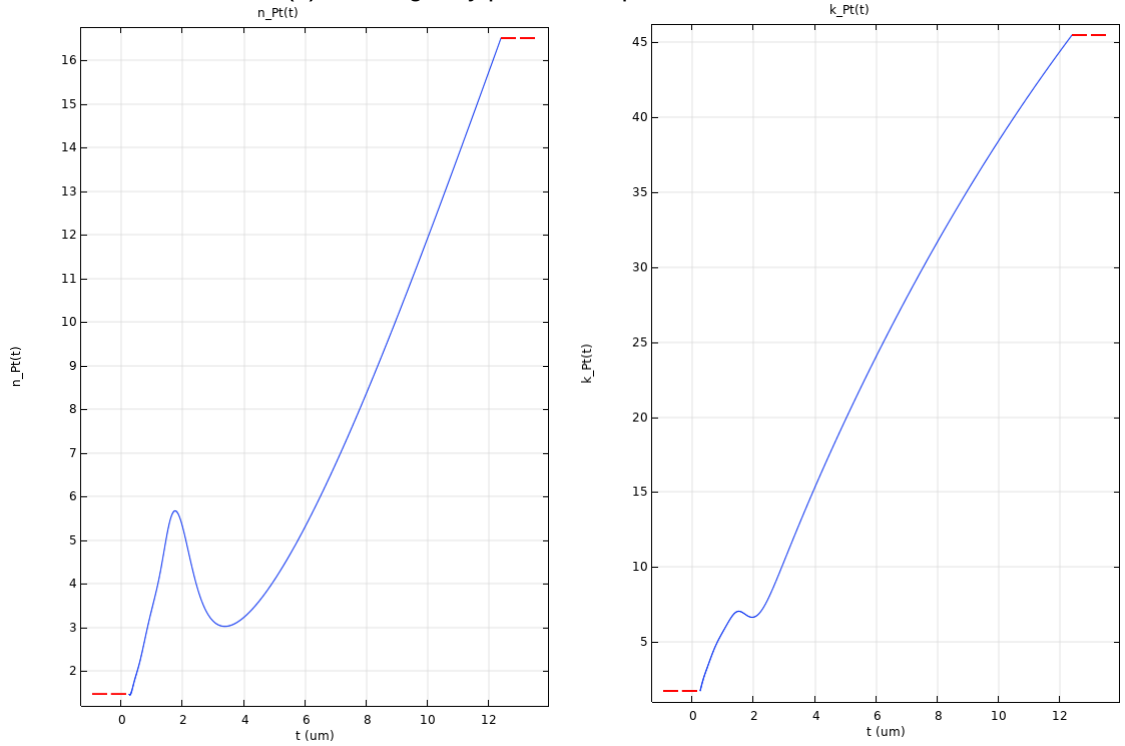

(a) **(b)**

Figure A.4 – Refractive index of Platinum (Pt)
(a) n , real part of complex index of refraction
(b) $\boldsymbol{k}$, imaginary part of complex index of refraction